2018-03-29

Activatable Fluorophores Combined with Amphiphilic Polymer Carriers for Bioimaging

Sicheng Tang
University of Miami, tabristang@gmail.com

Follow this and additional works at: https://scholarlyrepository.miami.edu/oa_dissertations

UNIVERSITY OF MIAMI

ACTIVATABLE FLUOROPHORES COMBINED WITH AMPHIPHILIC POLYMER
CARRIERS FOR BIOIMAGING

By

Sicheng Tang

A DISSERTATION

Submitted to the Faculty
of the University of Miami
in partial fulfillment of the requirements for
the degree of Doctor of Philosophy

Coral Gables, Florida

May 2018

UNIVERSITY OF MIAMI

A dissertation submitted in partial fulfillment of
the requirements for the degree of
Doctor of Philosophy

ACTIVATABLE FLUOROPHORES COMBINED WITH AMPHIPHILIC POLYMER
CARRIERS FOR BIOIMAGING

Sicheng Tang

Approved:

_____
Françisco M. Raymo, Ph.D.
Professor of Chemistry

_____
Roger M. Leblanc, Ph.D.
Professor of Chemistry

_____
James N. Wilson, Ph.D.
Associate Professor of Chemistry

_____
Guillermo Prado, Ph.D.
Dean of the Graduate School

_____
James D. Baker, Ph.D.
Professor of Biology

TANG, SICHENG   (Ph.D., Chemistry)

<u>Activatable Fluorophores Combined with;</u>   (May 2018)
<u>Amphiphilic Polymer Carriers for Bioimaging.</u>

Abstract of a dissertation at the University of Miami.

Dissertation supervised by Professor Françisco M. Raymo.
No. of pages in text. (141)

Self-assembling amphiphilic macromolecular nanoparticle, with a hydrophobic inner core and hydrophilic shell, can capsulate organic dyes inside. Thus, as a result, could be a valuable delivery vehicle for biology applications. We have developed a family of polymers, as supramolecular hosts, with decyl and polyethylene glycol side chains, exhibiting different hydrophobic/hydrophilic ratio, polyethylene glycol length or molecular weight. The polymers assemble into particles in neutral buffer and capture hydrophobic BODIPY in their interior. The relationship between critical concentration, dye loading property, hydrodynamic diameter and polymer structures were investigated. These provided a guideline to design self-assembling supramolecular hosts for the encapsulation of fluorescent guests and can lead to ideal delivery vehicles for the imaging probes to target locations in biosystems. In additional, a halochromic coumarin-oxazine fluorophore was connected to the side chains of an amphiphilic polymer covalently, with folate ligands as targeting agents to MCF-7 cancer cells. The pre-fluorophores did not produce any detectable fluorescence at neutral pH, but are converted into fluorophores with red emission in acidic environment. Thus, this design offers the opportunity to highlight cancer cells selectively with high brightness and optimal contrast.

We also designed a photoactivatable BODIPY with two oxazines attached. As a result, the oxazine heterocycles can be disconnected stepwise upon UV irradiation and each product exhibit different emission bands. When relative amounts of chromophores are placed in a polystyrene bead matrix, the ratio of three component can be modulated by dose of activating photons. This ratiometric strategy can be applied to write barcode inside biosystems: different regions of a same animal can be labeled with different barcodes to allow the monitoring of the spatiotemporal tracking.

To my family and friends

TABLE OF CONTENTS

Page

LIST OF FIGURES

viii

xiv

LIST OF TABLES

xv

CHAPTER 1 FLUOROPHORES AND CARRIERS FOR BIOIMAGING

1.1. Introduction

Fluorophores are a group of unique chemical compounds that can absorb a certain electromagnetic irradiation and re-emit light. The electronic states involved in this process can be illustrated by Jablonski Diagram (**a** in Figure 1.1): molecules absorb electromagnetic radiation and thus, undergo electronic excitation from their ground state to their excited state, which can then release energy radiatively. If the emission of light occurs from a singlet excited state, in which the excited electrons retains its original spin, the phenomenon is termed fluorescence. While in phosphorescence, the light is emitted from a triplet excited state, in which the excited electron inverts its spin. Generally, fluorescence occurs in the nanosecond timescale and is much faster than phosphorescence, which occurs in the range of microseconds to seconds[1]. The re-emitted photons can be captured by fluorescence microscope (**b** in Figure 1.1). The basic operating principles of a fluorescence microscope involve the illumination of the labeled specimen with an excitation source through an objective lens. The radiations focused on the sample excite the many fluorescent labels from their ground state to one of their excited singlet states. The excited species relax thermally to the first singlet excited state and then radiatively to S_0. The emitted light is collected on the detector, through the very same objective lens, to reconstruct an image of the labeled sample with micrometer resolution on a millisecond timescale. In fact, the fluorescence microscope has become an indispensable analytical tool in the biomedical laboratory for the investigation of cells and tissues.
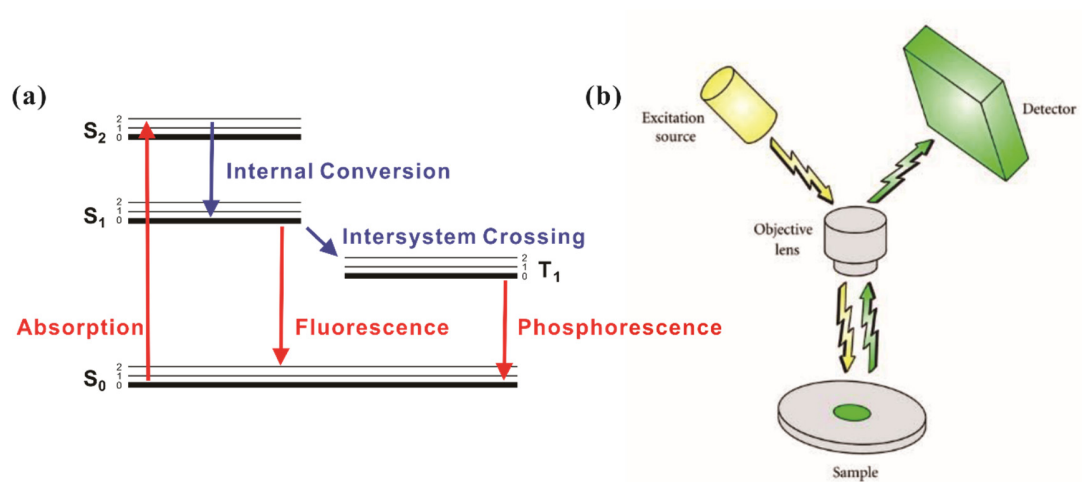
Figure 1.1 (a) Jablonski diagram illustrating excitation of a fluorescent molecule from the ground state (S_0) to the second singlet excited state (S_2) is followed by internal conversion to the first singlet excited state (S_1). The molecule in S_1 can either decay nonradiatively or emit light in the form of fluorescence to regenerate S_0. Alternatively, it can undergo intersystem crossing to populate the first triplet excited state (T_1) and then either decay nonradiatively or emit light in the form of phosphorescence to regenerate S_0. (b) The fluorescence microscope records images of samples labelled with fluorescent molecules by exciting the labels and collecting their emissions.

Traditional imaging techniques, such as ultrasound, X-ray radiography, computed tomography, magnetic resonance imaging and positron-emission tomography scanning, has been widely used to study biology systems. However, the strategies stated above sometimes fail to achieve a high contrast between targets of interests and background[2]. Fluorescent based bioimaging assays, who aim to visualize, characterize, and measure biological processes at the molecular and cellular levels in living systems, have found particular interest because they hold certain advantages (sensitive, selective, rich in contrast and versatile) and could be an ideal modality for biosystem studies, such as cellular organ labels, chemical indicators, and enzyme substrates[3].

Though bioimaging is largely driven by the photophysical properties of synthesized fluorophores, the development of nanotechnology significantly facilitates the imaging

research.　Incorporating with nano-sized carriers whose surface has been properly functionalized, for example with receptors, ligands or antibodies, so as to recognize the specific counterpart, the designed fluorophores have several advantages compared to traditional ones.　Firstly, loading the fluorophores in nanocarriers can increase their bioavailability, which otherwise will be most likely eliminated by liver and kidneys rapidly[4].　Secondly, hydrophobic drugs can only be administered intravenously after addition of solubilizing adjuvants like ethanol or Cremophor EL, which is often accompanied with toxic side effects[5-6].　Incorporation of these drugs in nanocarriers avoids the use of adjuvants[7].
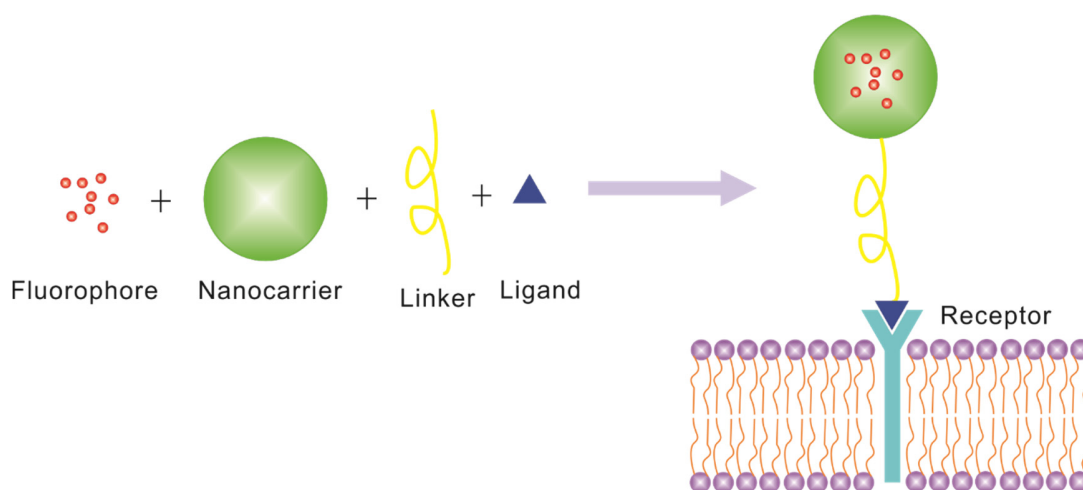
Figure 1.2 Molecular Imaging Probe

Based on these factors mentioned above, when designing a receptor targeted fluorescent probe, several concerns usually arise, such as (1) what fluorescent moiety should be used? (2) What types of carrier should be used to transport the dye?　(3) What kind of strategy should be applied to achieve a high signal-to-noise ratio (SNR)?　The introduction written below will have a general view of these question.

1.2. NIR Fluorophores

The major disadvantage of optical imaging technique is the tissue penetration caused by tissue absorption and scattering. Near infrared (NIR) fluorophores can give out fluorescent signals between 650 – 900 nm, where the absorption and scattering of tissue are minimized[8]. Thus, the problem can be partially solved by modulating the optical signals to near infrared (NIR) region, under which the interference of tissue absorption and scattering is minimized. Moreover, tissue autofluorescence is negligible in the NIR region, and less fluorescence extinction enhance deep tissue penetration with minimal background interference[9].
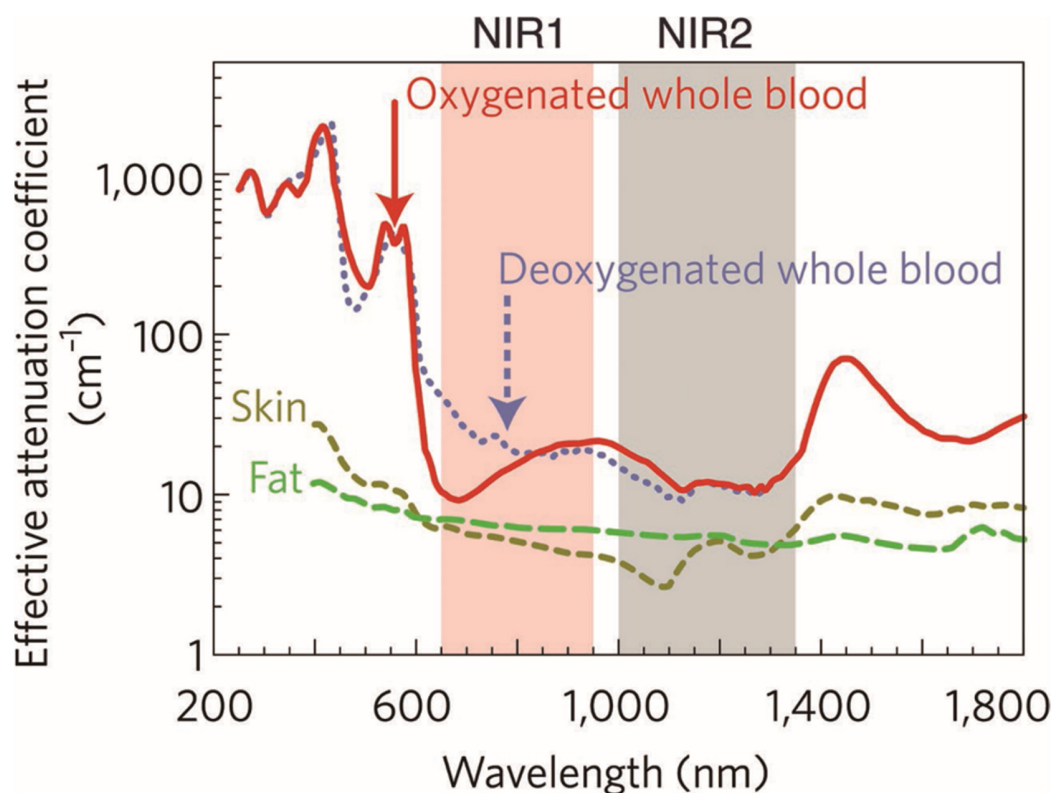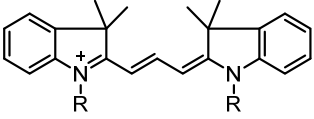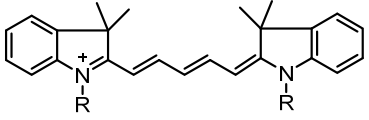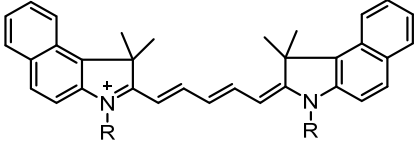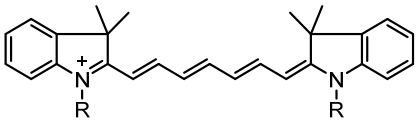
Figure 1.3 Near-infrared optical windows in biological tissues. The effective attenuation coefficient graphed as a function of wavelength shows that absorption and scattering from oxygenated blood, deoxygenated blood, skin and fatty tissue is lowest in the NIR1 and NIR2 spectral regions[10-11].

1.2.1. Small Molecule Fluorophores

Cyanine Dyes.

Cyanine dyes were firstly developed in 1856, by Williams. Typical cyanine dye contains two aromatic nitrogen-containing heterocycles, as charged fluorophores, linked by an odd-number polymethine bridge[12]. The model compound of cyanine, monomethine cyanine, generally show an absorption in the visible region, with a narrow absorption band, high extinction coefficient (in most cases reaching 200,000 mol^{-1} cm^{-1} L) and high quantum yield[13]. With the elongation of the vinylene moiety between the two heterocycles, the molecules show a bathochromic shift by approximately 100 nm. For example, pentamethine (Cy5 in Table 1.1) derivatives can reach a near-infrared region (> 700 nm), and heptamethine cyanines (Cy7 in Table 1.1) show absorption beyond 1000 nm[13]. On the other side, the extension of the nitrogen-containing heterocycles leads to a bathochromic shift by about 20 nm (Cy 5.5 in Table 1.1)[14]. Based on the unique fluorescent properties of cyanine dyes, they are widely used in semiconducting materials, laser materials, optical recording media, paints, and bioprobes for nucleic acids and proteins[15-17]. However, traditional cyanine dyes suffer from poor photostability, self-aggregation and low quantum yield in aqueous solution, the major environment in biosystems. With the continuous development of cyanine dyes, significant progress has been made to overcome these limitations. Ongoing efforts in the research of cyanine dyes are focused on exploiting their value in biomedical applications.

Table 1.1 Optical properties of typical cyanine dye in aqueous buffer[18].

Fluorophore	Structure	Abs/nm	Em/nm	φ
Cy 3		558	572	0.67
Cy 5		649	670	0.28
Cy 5.5		675	694	0.28
Cy 7		743	767	0.28

By replacing the central link of polymethine with a rigid cyclohexenyl group, the photostability and fluorescent quantum yield are significantly increased[19-20]. James *el al.* constructed a series of symmetrical polymethine dyes containing different bis-N-substituted indoles, linkers and benzindole moieties and found out that the structure with a cyclic chloro-cyclohexene moiety showed better fluorescent imaging ability[21]. Other Studies also show that the fluorescence efficiency is greatly increased upon binding of cyanine dyes with nucleic acids or proteins as a result of the rigidization of the fluorophores[22-23]. Based on the rigidity study, Peng *et al.* synthesized a series of 3H-indocyanine dyes with different N-substituents[24]. The results showed that the electron withdrawing ability on N-position can tremendously improve the photostability. They also tried to replace the chlorine located on the central cyclohexene ring with other electron

withdrawing/donating groups to investigate its effects[25]. Those who were replaced by electron donating groups showed a better photostability in aqueous solutions. As the major media in biosystems is water, the hydrophilic property is a must for these probes. So, NIR cyanine dyes with the introduction of carboxylic or sulfonic acid groups have been synthesized[26-27]. These newly synthesized cyanine dyes were found to have a large stock shift, strong fluorescence and a great improvement of water solubility. A "turn on" system involving a bis(heptamethine cyanine) dye moisty, which contains two cyanine subunits, was synthesized by Strekowski et al.[28]. This designed system exhibited negligible fluorescence in aqueous solution. However, once bound to with protein, a strong increase in fluorescence (~ 1000 folds) was observed, leading to a high SNR.

Rhodamine Dyes.

Rhodamine dyes are one group of xanthene dyes. Owing to their photophysical properties, such as high molar extinction coefficients and good photostability, this type of dyes have been widely used as probes for fluorescent imaging. However, most rhodamine-based fluorophores only emit in visible region (500 - 600 nm), and thus do not meet the requirements for bioimaging mentioned above. So, efforts have been paid to modify its xanthene core, in order to tune the emission wavelength. Wang et al. synthesized a NIR rhodamine dye by replacing the center oxygen atom by silicon[29]. This system was again a "turn on" one, whose fluorescence can be controlled by a ring-opening process. Kiode et al. further developed four rhodamine derivatives based on the Si substituted rhodamine[30]. The four designed fluorophores can emit strong NIR in aqueous media, with their emission peaks ranging from 660 nm to 740 nm. The same research group also developed a Te substituted rhodamine, which showed neglectable fluorescence in PBS[31]. However, once

contacted with reactive oxygen species (ROS), the oxidation of the Te lead to a ~ 200-fold increase in its fluorescence. This "turn on" property made it a suitable probe for detecting ROS in biosystems.
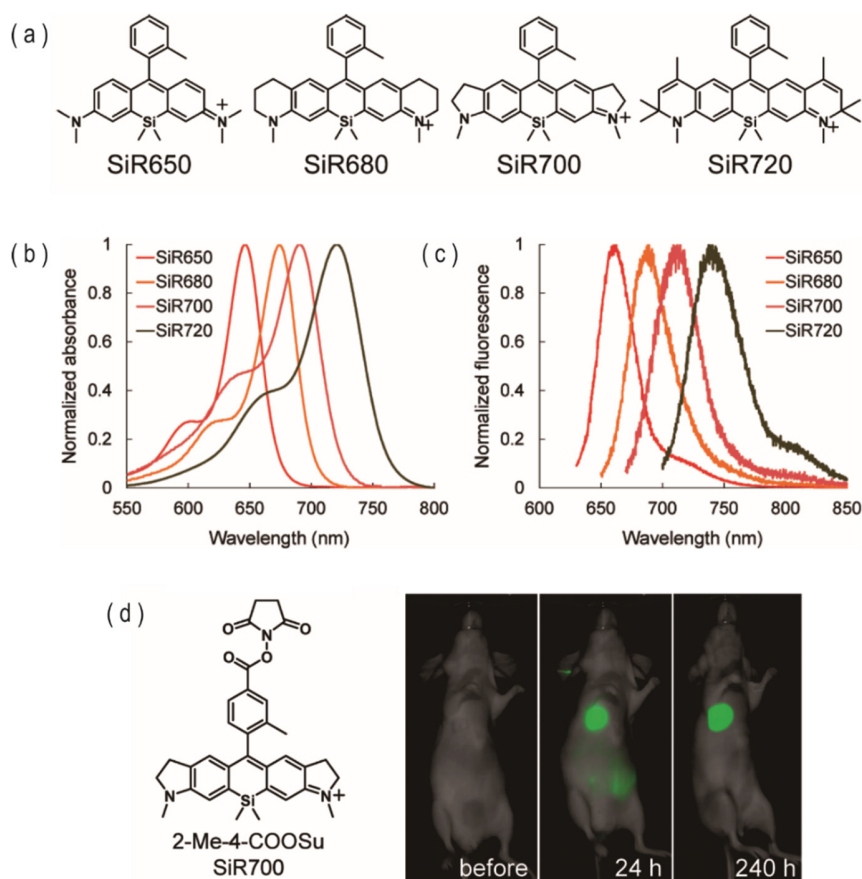
Figure 1.4 (a) Chemical structures of SiR650 and newly synthesized NIR wavelength-excitable fluorescence dyes, SiR-NIRs. Normalized absorption (b) and emission (c) spectra of 1 μM SiR-NIRs, measured in PBS at pH 7.4.   (d) In vivo tumor imaging with SiR700-labeled anti-tenascin-C antibody (SiR700-RCB1). Xenograft tumor model mice prepared with human malignant meningioma HKBMM cells were intravenously injected with 300 μL of 130 μg/mL SiR700-RCB1 (D/A = 1.6). The tumor fluorescence images were obtained before and at 24 h after the injection.

BODIPY Dyes.

BODIPY stands for a group of dyes that have a skeleton of boron-dipyrromethene, which was firstly depicted in 1968[32]. They generally have a narrow fluorescence band high quantum yield, and also exhibits excellent thermal and photochemical stability, as long as

low toxicity. These characteristics make them a desirable tool for laser dyes, molecular photonic wires, chemosensors, electron transfer reagents and bioprobes[33-39]. But traditional BODIPY dyes share the same problem with rhodamine: their absorption and emission wavelengths are both located in visible region, instead of NIR one. Therefore, great efforts have been made to shift the absorption and emission spectrum to NIR region by research groups worldwide.   Currently, the two main strategies used to shift BODIPY into NIR dyes are (1) functionalization at α-, β- sites of the BODIPY core to extend π-conjugation[40-42], (2) replacing the *meso*-carbon by an imine type nitrogen atom[40, 43] (Figure 1.5). The most straightforward way to extend the conjugation would be introduce aromatic units at 3- or 5- positions, as illustrated by Burghart *et al.*[44]. The extension leaded to a bathochromic shift of ~ 50 nm in both absorption and emission compared to regular BODIPY, but this also caused a decrease in fluorescence quantum yield. The possible energy loss from the excited state via thermal rotation of the aromatic substituents could be the reason. Thus, Chen *et al.* synthesized three series of BODIPY dyes by merging the 3- and 5-phenyl rings with the fluorescent core, which forms six-membered rings and reduced the rotation, as well as the torsion angles between the phenyl groups and the central core[45].
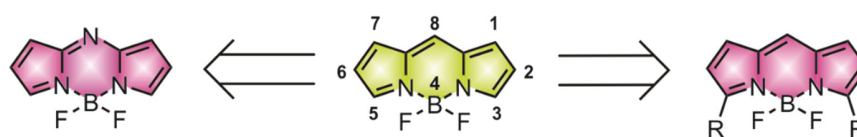
Figure 1.5 BODIPY skeleton and methods to tune its absorption and emission.

Not only limited to bioimaging applications, BODIPY dyes are also utilized in photodynamic therapy. By modifying the NIR BODIPY skeleton, Shen's group developed a bromo substituted derivative, which can generate singlet oxygen when exposed to a

irradiation at 635 nm[46] (Figure 1.6). Nevertheless, Wang et al. synthesized and characterized two novel BODIPY dyes, each containing two pyridinium groups and exhibiting DNA photocleavage ability through the production of free radicals[47].
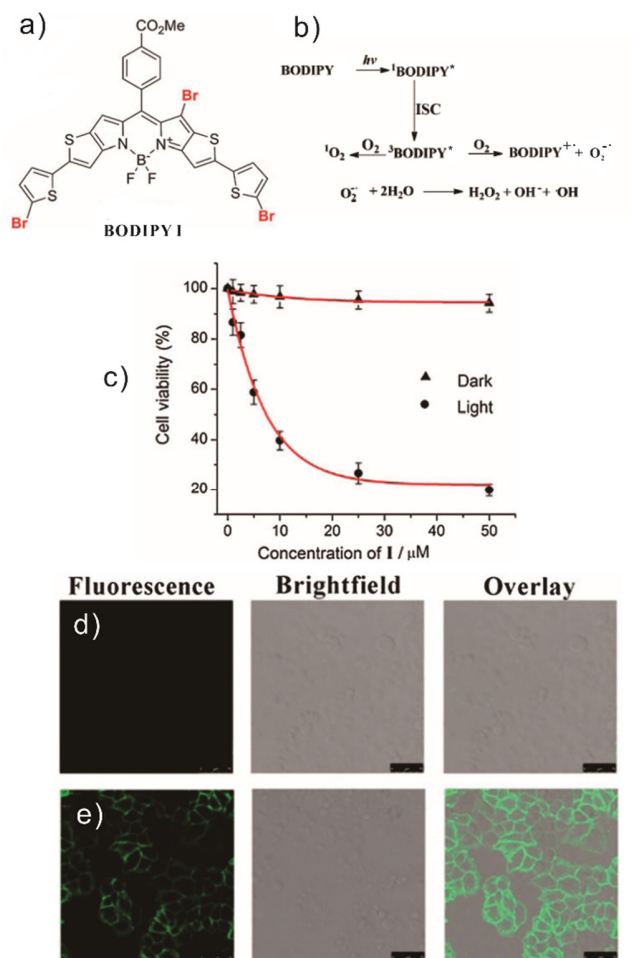
Figure 1.6 (a) Structure of NIR BODIPY I. (b) Proposed photodamage mechanism for BODIPY I. (c) the photocytotoxicity of sensitizer I as demonstrated by an MTT assay based on HeLa cells in the absence and presence of light (λ_{irr} = 635 nm). Confocal fluorescence images in HeLa cells (λ_{ex} = 488 nm, λ_{em} = 510 – 530 nm). (a) I (10 mM) treated cells in the dark; (b) I (10 mM) treated cells irradiated for 100 s by a 635 nm laser beam with a power density of 400 mW cm^{-2}. The fluorescence signal is due to the presence of Annexin V-FITC which acts as a probe for apoptotic cells[46].

Squaraine Dyes.

Squaraines were firstly developed in 1965, by Treibs and Jacob[48]. They are a group of molecules that process an electron deficient four-membered ring, oxocyclobutenolate, as a center core, cooperating with two donor moieties, such as aromatic or heterocyclic components, at the two sides of the core to afford a donor-acceptor-donor motif[49]. These dyes typically emit in the red/NIR region, exhibiting excellent photophysical properties, including high molar extinction coefficient[50-51]. However, like the most organic dyes, squaraine dyes have an issue on solubilizing in water, due to their large and planar hydrophobic π-conjugated structures. What's more, the squaraine dyes tend to aggregate in aqueous solution, because of its insolubility, and the aggregates show minimum fluorescence, as well as a broadened absorption band. So currently, a lot of efforts have been paid to the design of NIR squaraine dyes, in order to regulating its aggregation or disaggregation behavior. To improve the solubility in aqueous solution, Suzuki and coworkers made a step to synthesize a water soluble squaraine[52]. They made a squaraine derivative with four sulfonate moieties on the side chain, which showed a tremendous solubility in PBS buffer along with an absorption peak at 787 nm (1 in Figure 1.7). Later on, Smith's research group reported squaraines surrounded by different types of rotaxane rings[53](2 in Figure 1.7). The rotaxane ring not only increased the solubility of squaraine in water, but also prevent it from aggregation, as the surrounded space were taken up by rotaxanes. The whole unit showed a better photostability and stability in various solvent systems. As this strategy did not involve the covalent attachment between the host and guest, it suggest a potential versatile method to construct various types of highly stable, water-soluble NIR probes for bioimaging.
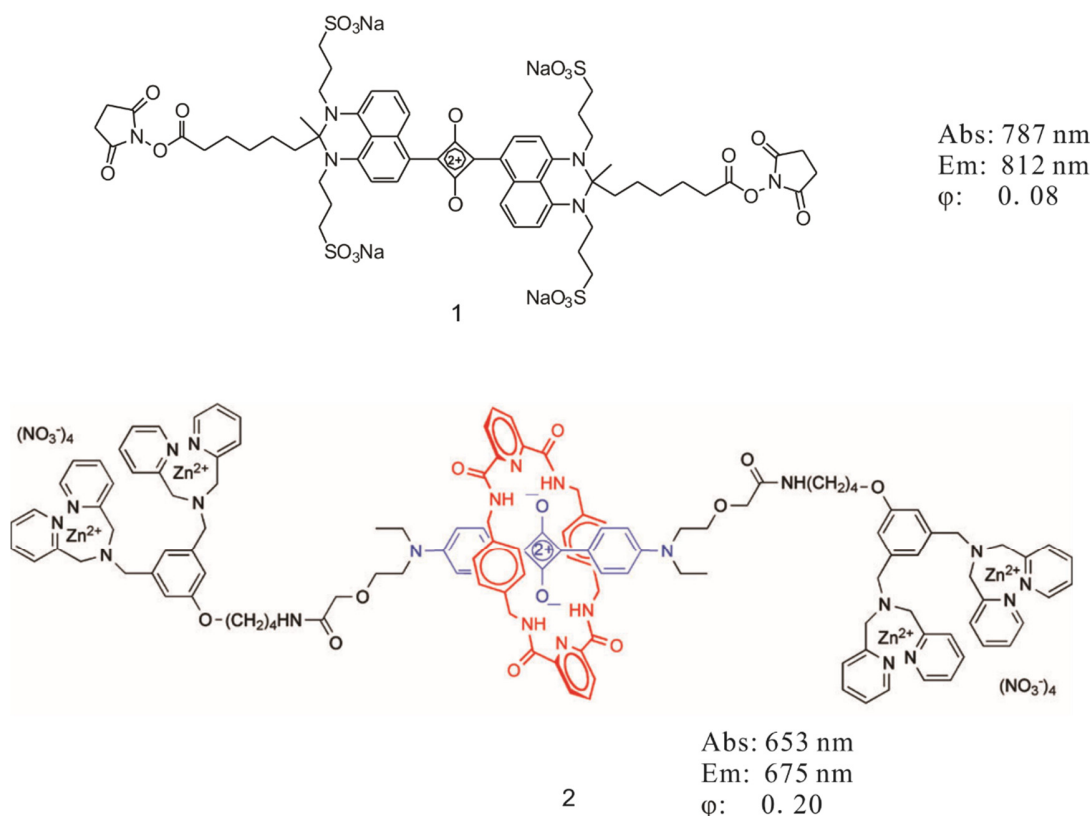
Figure 1.7 Example of water-soluble NIR squaraine dyes achieve by (1) substitution with sodium sulfonate; (2) surrounded by rotaxane.

Phthalocyanines Porphyrin Derivatives.

Phthalocyanines and porphyrin derivatives are versatile functional pigments consisting of four pyrroles or isoindoles, bridged through four nitrogen atoms[54]. There are $4n + 2$ π electrons located in the center 16-member ring, and they are strongly delocalized around the chromophore. As a result, this group of molecules have a relatively high thermal and chemical stability, which could survive intense electromagnetic irradiation. The two hydrogen atoms located at the center of the cavity can be modified by metal ions and various substituents, which, as a result, leads to various physical/chemical properties[55]. In the last two decades, numerous works have been done to investigate the applications of phthalocyanines and porphyrin derivatives, not only limited as fluorescent dyes, but also

electronics, optoelectronics and biomedicines. Though this type of molecule showed a good thermal and chemical stability, they cannot serve as a good probe for bioimaging as the light emitted located below 700 nm[56]. Thus, strategies such as applying benzene groups or electron-donating groups onto the skeleton to move the absorption and emission bands towards NIR region have been developed. Expanded pentafluophenyl porphyrins were synthesized by Osuka's research group[57]. They managed to tune the absorption wavelength to as long as 950 nm. Xie *et al.* synthesized a new class of N-confused expanded porphyrins, with triangular shapes and emitted from 800 – 1000 nm[58]. Conjugated porphyrin dimers were also found to be utilized in imaging studies[59]. These dimers exhibited far-red spectral region fluorescence (700 – 800 nm), where the tissue showed neglectable absorption and scattering.

Besides the application in bioimaging as fluorescent probes, phthalocyanines and porphyrin derivatives also can also generate singlet oxygen upon irradiation, showing a potential to be photosensitizers for photodynamic therapy[60]. Hu *et al.* synthesized several benzyl-substituted phthalonitriles with the cavities occupied by Zn[61]. These type of phthalonitriles showed the property of generating singlet oxygen under irradiation, and further research developed its function for photodynamic therapy. In another similar study, Karunakaran and coworkers developed a novel porphyrin derivative, with its cavity occupied by Zn, which showed favorable photophysical properties, negligible dark toxicity, along with high *in vitro* photodynamic therapy[62].

Therefore, with excellent stability and suitable photophysical properties, versatility of newly developed phthalocyanines and porphyrin derivatives make them greatly potential to be extensively applied in clinic for both biological imaging and cancer therapy.

1.2.2. Macromolecule Fluorophores

Quantum Dots.

Quantum Dots (QDs) are fluorescent inorganic nanocrystals, with a core-shell structure. QDs showed high extinction coefficients, high fluorescent quantum yields, sharp emission bands, and its emission wavelengths can be modified by changing size of the nanocrystal[63]. Generally, the emission band will shift towards the longer wavelength when the diameter of QDs increases (Figure 1.8). Thus, QDs with suitable size, along with NIR emission, could be a fluorescent probe for bioimaging[64].
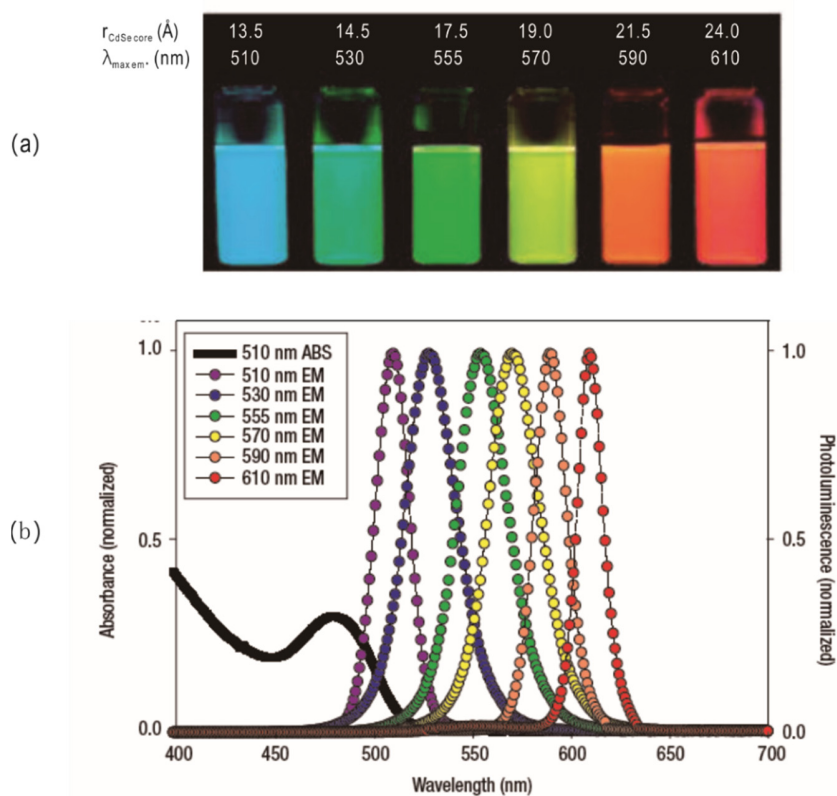
Figure 1.8 (a) Photo demonstrating the size-tunable fluorescence properties and spectral range of the six QD dispersions versus CdSe core size. All samples were excited at 365 nm with a UV source. (b) Absorption and emission of six different QD dispersions. The black line shows the absorption of the 510-nm emitting QDs[65].

However, the main challenge remains in their toxicity. The strategies commonly used to reduce their toxicity is to coat the surface with a less toxic layer[66-67]. Another problem researchers are facing is the water solubility issue. Xue *et al.* used four different agents to help NIR-emitting QDS solubilize in water[68]. Though all the four agents did their functionality, they have different effects on the photophysical properties of QDs. QDs with Nanohydrogels and amphiphilic polymers showed a dramatic decrease in quantum yield, while the ones coated with N-succinyl-N'-ocytl chitosan (SOC) micelles or Glutathione (GSH) as phase transfer agents showed relatively strong fluorescence. Based on these strategies, Cao *et al.* developed a SOC micelles coated QDs for bioimaging[69]. This type of QDs exhibited low cytotoxicity and were selectively accumulated in tumor through enhanced permeability and retention (EPR) effect (Figure 1.9).
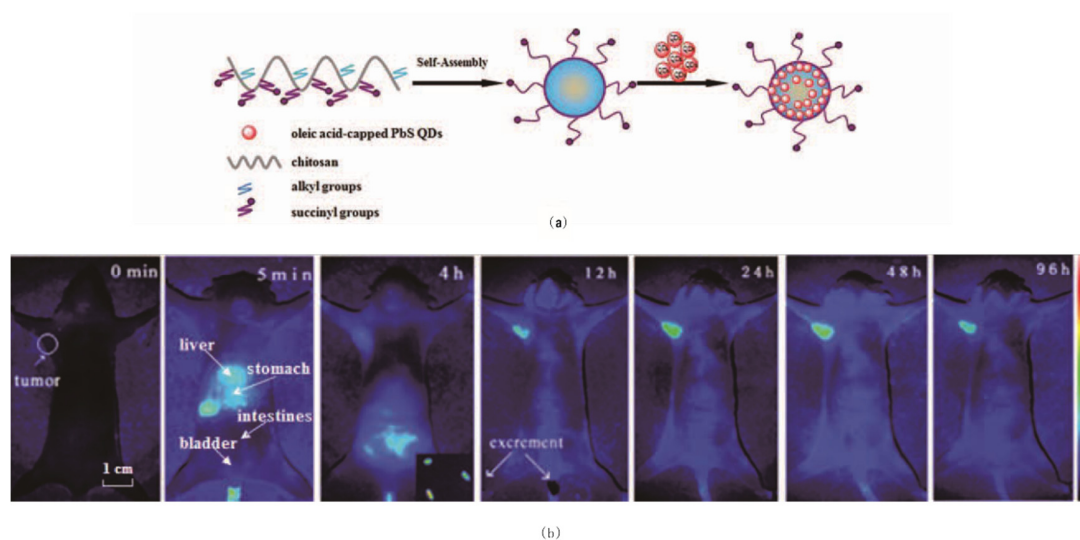
Figure 1.9 (a) Schematic diagram of the synthesis procedure for PbS QDs-loaded SOC micelles. (b) *In vivo* imaging of PbS QDs-loaded SOC micelles by NIR imaging system. The Bel-7402 hepatoma cells were injected in the left armpit of each nude mouse. After the diameter of the tumor reached about 0.4 cm, the mice were fasted to avoid the background signal and ready for use. PbS QDs loaded SOC micelles were intravenously injected via the tail vein into tumor-bearing mice and monitored for 96 h. Fluorescence imaging of the preinjection mouse was acquired and set as background imaging[69].

Conjugated Polymers.

As fluorescent probes for bioimaging, conjugated polymers (CPs) have attracted more and more attention, because they showed good stability, non-cytotoxicity and tunable emission[70-71]. CPs have a backbone of alternating σ- and π-bonds, with their absorption and emission strongly depends on the composition. The introduction of alternating push-pull motif has been used frequently to lower the bandgap, which further leads to a bathochromic shift in absorption and emission[72]. The most popular CPs are polyacetylene, polyaniline, polycarbazole and so on[73] (Figure 1.10).
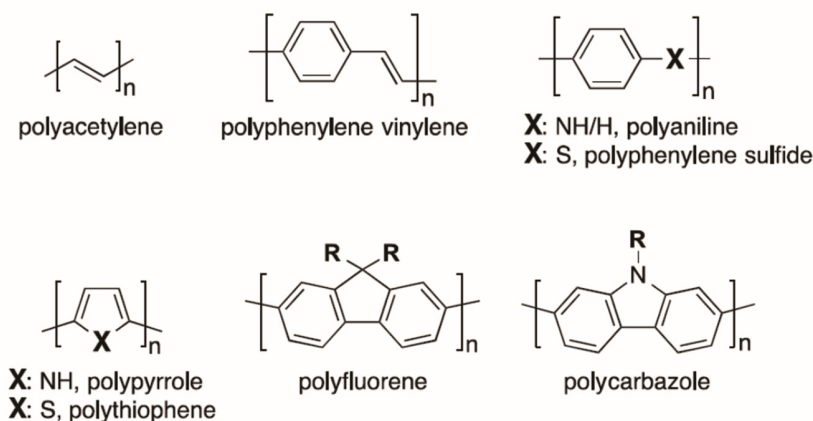
Figure 1.10 Structures of conventional conjugated polymers.

However, as the major part of CPs is highly hydrophobic, strategies have to be implemented to make them operable in aqueous solution. Three methods were commonly used to increase the solubility. The first approach tried to introduce charged moieties on the polymer side chains[74]. Another method linked CPs to biological structures or liposomes[75-76]. The most common technique was to prepare the CPs into polymer dispersion in aqueous solutions, which was also known as polymer dots (Pdots)[77]. Liu *et al.* developed CPs who have selectivity for folate receptor by conjugate folic acid onto the

surface of CPs[78]. These synthesized CPs showed a selectivity for HeLa cells and MFC-7 cells. In addition, they utilized receptor mediated endocytosis to label ovarian cancer cells with overexpressed folate receptors (SKOV-3 cells) (Figure 1.11).
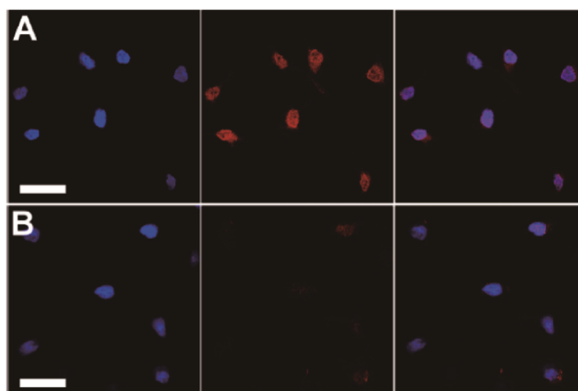
Figure 1.11 Confocal fluorescence images of SKOV-3 cells labeled by Pdot-folate conjugates. (A) The blue fluorescence results from the nuclear counterstain Hoechst 34580, and the red fluorescence is due to the Pdot–folate conjugates. The right panel shows the overlay of the blue and red fluorescence; (B) images of negative control samples in which cells were incubated with bare Pdots without folate functionalization.

1.3. Supramolecular Amphiphilic Nanocarriers

As most NIR fluorophores mentioned above show a hydrophobic property, a common method, who should be easy in practice and does not affect the photophysical properties of dyes, should be developed. Amphiphilic polymers are valuable macromolecular synthons for the construction of supramolecular hosts capable of capturing a diversity of molecular guests in their interior[79-94]. Their covalent skeleton incorporates hydrophilic and hydrophobic segments that guide the assembly of multiple polymer chains into single particles of nanoscaled dimensions in aqueous environments. Solvophobic interactions bring the hydrophobic fragments of distinct polymer components in contact to minimize their direct exposure to water. Concomitant solvation of the hydrophilic fragments ensures optimal aqueous solubility and prevents further association of the nanoparticles into micro- and macroscaled aggregates. The overall result is the spontaneous assembly of

nanostructured constructs with hydrophilic surface and hydrophobic interior, where multiple hydrophobic guests can be encapsulated. In fact, such supramolecular hosts can transfer, otherwise insoluble, molecules into aqueous phases and carry them across hydrophilic media. Indeed, self-assembling nanoparticles of amphiphilic polymers are promising supramolecular vehicles for the transport of drugs, photoactivatable fluorophore, fluorescent dyes into specific intracellular targets[95-112]. Some of the fundamental aspects of these amphiphilic nanocarrier will be discussed briefly in the following sections.

1.3.1. Critical Concentration.

When mixed with water at relatively low concentrations, most amphiphiles migrate to the air/water interface (*a* in Figure 1.12) to avoid direct exposure of their hydrophobic components to the aqueous environment[113-115]. In the resulting arrangement, the hydrophilic segment of the molecule remains within the aqueous phase, while the hydrophobic counterpart protrudes above the aqueous surface. If the amphiphile concentration is gradually increased, then the air/water interface becomes increasingly crowded until additional molecules are forced to reside within the aqueous phase (*b* in Figure 1.12). Above a certain concentration threshold, denoted critical concentration (CC), the amphiphiles in the aqueous phase self-assemble into micellar aggregates (*c* in Figure 1.12) to prevent the direct exposure of their hydrophobic parts to water. In fact, the hydrophobic portions of the many molecules in each supramolecular assembly point toward the interior of the construct, while the hydrophilic parts are on the surface to be directly exposed to the aqueous solvent. Such an arrangement ensures the most appropriate environment around the hydrophobic and hydrophilic fragments of each molecular component of the self-assembling supramolecular constructs. Any further addition of

amphiphiles slightly beyond the CC then translates into an increase of the number of micelles dissolved in the aqueous phase. Under these conditions, the many supramolecular assemblies remain isolated from each other with no spatial correlation. At concentrations significantly greater than the CC, however, liquid-crystalline phases with long-range orientational and positional order may appear[116-117].
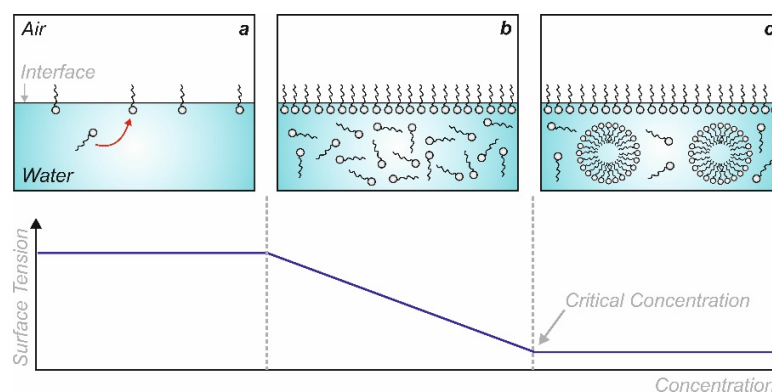
Figure 1.12 The addition of increasing amounts of amphiphilic compounds to water encourages the formation of a layer of molecules at the air/water interface (*a* and *b*) and, eventually, results in the self-assembly of micellar aggregates above a critical concentration (*c*).

The morphology of micellar aggregates of amphiphilic components is related to the structural composition and concentration of the individual building blocks and it can vary with the ionic strength and temperature of the solution[113-114]. Generally, these supramolecular assemblies are spherical (Figure 1.13) and, only occasionally, adopt globular or rod-like shapes. In all three instances, the interior of the aggregate is hydrophobic and the surface hydrophilic. However, certain amphiphiles tend to form bilayer assemblies capable of curling into spherical vesicles and encircling solvent molecules within their inner hydrophilic face.
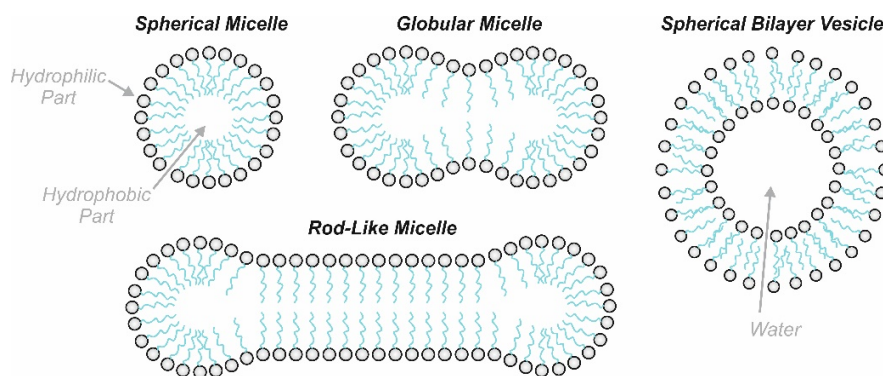
Figure 1.13 Common morphologies of supramolecular assemblies of multiple amphiphilic components.

The value of CC varies with the structural composition of the self-assembling building blocks and its determination for any amphiphile is essential to identify a range of optimal concentrations to induce the spontaneous formation of micellar aggregates. This crucial parameter can be measured with diversity experimental procedures based on its influence on certain physical variables, including chemical shift, absorbance, fluorescence intensity, ionic conductivity, osmotic pressure and surface tension[116-119]. Out of these many methods, those relying on fluorescence and surface tension measurements are relatively simple and, as a result, appear to be the most common protocols for CC determination in literature reports.

Fluorescence methods for CC determination rely on the ability of the micellar aggregates to encapsulate emissive and hydrophobic probes in their nonpolar interior[120-123]. These molecular guests must be selected to lack any significant solubility in aqueous environments on their own, but readily transfer into an aqueous phase after entrapment within their supramolecular hosts. Under these conditions, their fluorescence can be detected in water only if a given amphiphile is present at a concentration greater than the corresponding CC. For example, 9,10-bis(diphenylethynyl)anthracene (20 in Figure 1.14) is essentially insoluble in phosphate buffer saline (PBS), but readily dissolves in the

presence of significant amounts of an amphiphilic polymer (3)[124]. As a result, the treatment

of a fixed amount of 20 with identical volumes of PBS solutions containing increasing

concentrations of 3 can be exploited to identify the CC value of the polymer. Indeed, no

emission can be detected at low polymer concentrations (Figure 1.14). Once CC is reached,

however, the amphiphiles assemble into micellar aggregates. The resulting supramolecular

constructs capture the fluorescent species, transfer them into the aqueous phase and allow

the detection of their fluorescence. Consistently, a sudden increase in emission intensity

is observed above this particular concentration threshold (Figure 1.14).
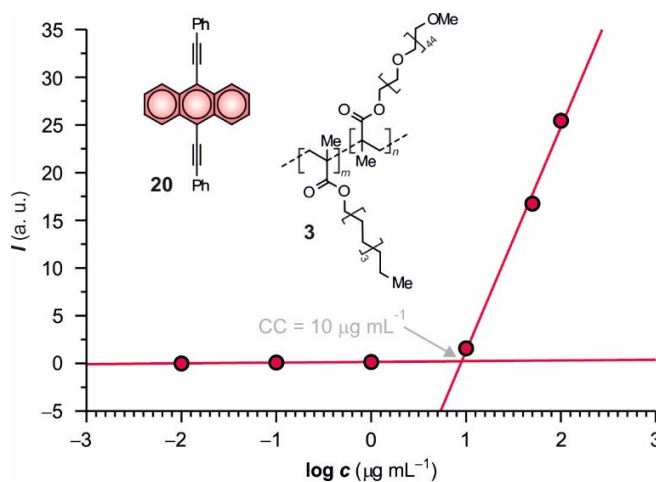
Figure 1.14 Plot of the emission intensity of 20 (1 μg mL^{-1}, λ_{Ex} = 440 nm, λ_{Em} = 476 nm) against the concentration of 3 in PBS at 25 °C.

In principle, the encapsulation of fluorescent probes in the interior of the micellar

aggregates might have an influence on the ability of the amphiphilic components to

assemble and, therefore, affect the actual CC value. This potential limitation can be

overcome with protocols based on measurements of surface tension, which do not require

the addition of any molecular guest125. Indeed, this parameter can be determined

experimentally with a variety of instrumental setups, including Traube's stalagmometer,

modified manometers or computer-controlled tensiometers calibrated with liquids of known surface tension.

Molecules in a liquid attract each other. These interactions are balanced in all directions for a given molecule within the bulk of the liquid. However, they are unbalanced for an equivalent molecule on the surface of the very same liquid, resulting in forces that tend to hold the liquid together. The surface tension (γ) is a measurement of such a cohesive energy that exists at the air/liquid interface. The presence of amphiphilic molecules at the interface disrupts these cohesive interactions with a concomitant decrease in surface tension. In fact, amphiphiles are often called "surface active" compounds or "surfactants", because of this effect. Specifically, the surface tension depends on the concentration of a given amphiphile, as shown schematically in Figure 1.12. It remains approximately constant at low concentrations, but drops rapidly with the crowding of the air/water interface and then shows a negligible change, once the micellar aggregates start assembling. As a result, CC can be estimated from the intersection of the linear correlations associated with the last two segments of the plot (Figure 1.12). For example, the dependence of the surface tension on the concentration of sodium dodecyl sulfate in water and the corresponding CC are illustrated in Figure 11[126].
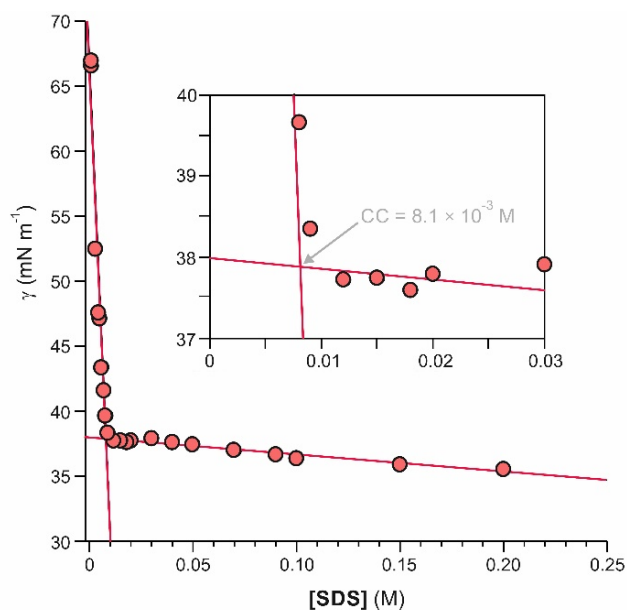
Figure 1.15 Plot of the surface tension of a solution of sodium dodecyl sulfate (SDS) in water against the amphiphile concentration at 25 °C

1.3.2. Hydrodynamic Diameter.

Dynamic light scattering measurements can provide a quantitative assessment of the size distribution of spherical nanoparticles dispersed in a solvent from the analysis of their random thermal motion (Brownian motion). Indeed, the translational diffusion coefficient (D_t) of the moving nanoparticles is inversely related to their hydrodynamic diameter (D_h) according to equation (1), where k_B, T and η are Boltzmann's constant, temperature and viscosity respectively. As a result of this correlation, the displacement of small diffusing nanoparticles over time (*a* in Figure 1.16) is more pronounced than that of large counterparts (*b* in Figure 1.16). In fact, the sequential tracking of the nanoparticle positions with very short probing intervals (< 100 μs) permits the determination of their physical dimensions, even when the moving objects are micellar aggregates of amphiphilic building blocks.

$$D_{\mathrm{h}} = \frac{k_{\mathrm{B}}T}{3\pi\eta D_{\mathrm{t}}} \tag{1}$$
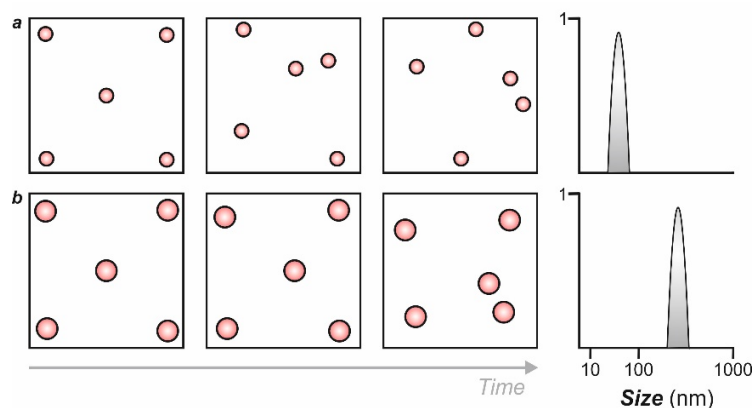
Figure 1.16 Illustration of the relationship between the speed of particle movement and the size.

Experimentally, this particular technique determines the aggregate size by measuring the random changes in the intensity of light scattered from the corresponding solution. Generally, a laser source illuminates the sample maintained in a transparent cell and the scattered light (Figure 1.17) is collected on a photomultiplier tube. As the diffusing aggregates are constantly in motion, the obtained optical signal shows random changes because of the constructive and destructive phase addition of the scattered light with time. Their size can then be extracted from this signal after an appropriate mathematical treatment. Specifically, the detected signal can be interpreted in terms of an autocorrelation function $[G(\tau)]$ of the delay time (τ), *i.e.* the time that elapses between two consecutive data collections. If all the particles are identical in size, $[G(\tau)]$ decays monoexponentially with τ, according to equation (2), and fitting of the experimental data provides an estimate of the decay constant (Γ). In turn, this parameter is directly related to D_{t}, according to equation (3), where the scattering vector (q) is a function of the refractive index (n) of the liquid, the wavelength (λ) of the laser and the scattering angle (θ), according to equation

(4). Thus, a measurement of $[G(\tau)]$ against τ ultimately provides a value of D_t and, in combination with equation (1), also of D_h.

$$G(\tau) = \exp\left(-2\Gamma\tau\right) \tag{2}$$

$$\Gamma = D_t\, q^2 \tag{3}$$

$$q = (4\pi n/\lambda)\, \sin(\theta/2) \tag{4}$$
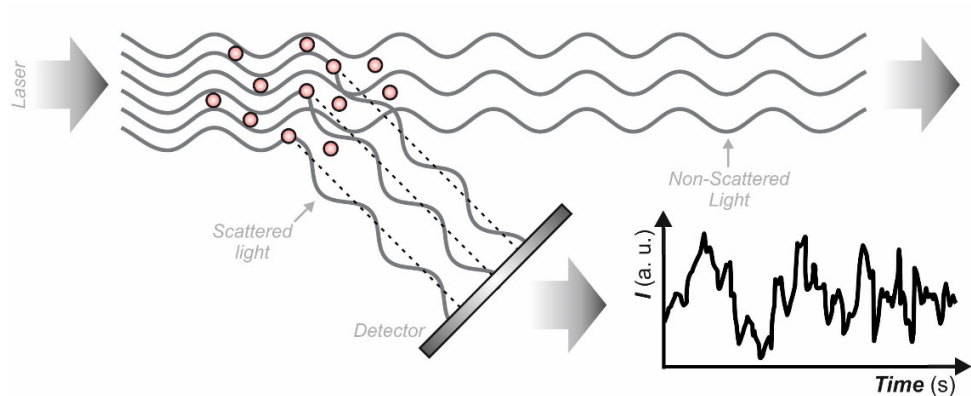
Figure 1.17 Schematic representation of the optical setup used for dynamic light scattering measurements of nanoparticle sizing35.

Nonetheless, most samples have a distribution of nanoparticle sizes and, therefore, the correlation of $[G(\tau)]$ and τ becomes a power series, according to equation (5). Once again, a decay constant ($\overline{\Gamma}$), which is the sum of all the individual exponential decays contained in the correlation function and is proportional to D_t, is extracted to obtain a weighted average of D_h, termed z-average size.

$$G(\tau) = \exp\left(-2\overline{\Gamma}\tau + \mu_2\,\tau^2 - \cdots\right) \tag{5}$$

Besides fitting a single exponential decay to the correlation function (eq. 5) to obtain the z-average size, a multiexponential function can be used instead to obtain the distribution of particle sizes. After applying such a mathematical algorithm, one gets the size distribution as a plot of the relative intensity of light scattered by the particles in various size classes.

As an example (Figure 1.18), shows the intensity distributions for amphiphilic polymers 3 and 21. Specifically, hydrodynamic diameters of *ca.* 10 and 130 nm are registered for these two particular amphiphilic macromolecules respectively.
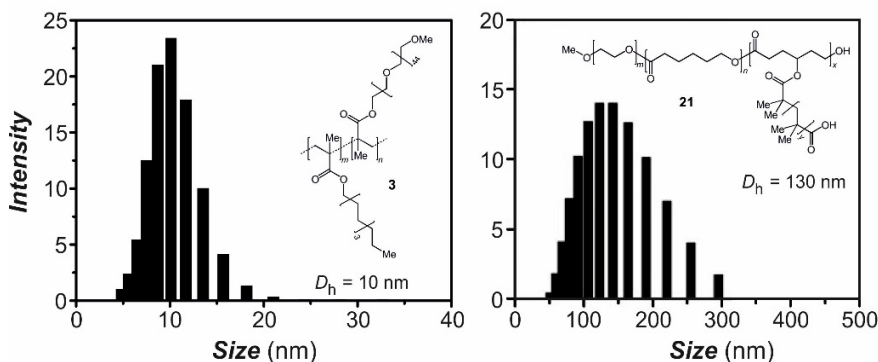
Figure 1.18 Chemical structure and hydrodynamic diameters, Dh, for amphiphilic polymers 3 and 21

1.4. Probing Strategies

The SNR in probing molecular processes and cellular functions in biosystems is depending on the efficiency of the delivery of fluorophores to target tissues. This delivery process is currently mediated by nonspecific mechanism followed by an activation mechanism and specific mechanism[127].

1.4.1. Specific Delivery

As more and more researches have been done to reveal novel specific factors that can only be recognized by a type of cells or tissues, newly designed fluorescent probes who are incorporated with these characteristic factors can giving out signals specifically from those cells or tissues. The factors that can be targeted for specific delivery by this approach include overexpressed receptors on membranes, adhesion factors, RNAs and so on.

Antibody or proteins bioconjugates are popular targeting agent which can bind to the surface receptors are widely used according to published papers[128]. The main challenge that researchers are facing is that before the probes diffusing into targets, they are uptake

by the liver[129]. Though some studies somewhat overcome this problem, it is more common to use nuclear methods because they are not antigenic and are small enough for a faster diffusion compared to biomacromolecules. Additionally, small molecules are easier to prepare and are amenable to combinatorial synthesis. This approach can also be applied to functionalize the cairriers.
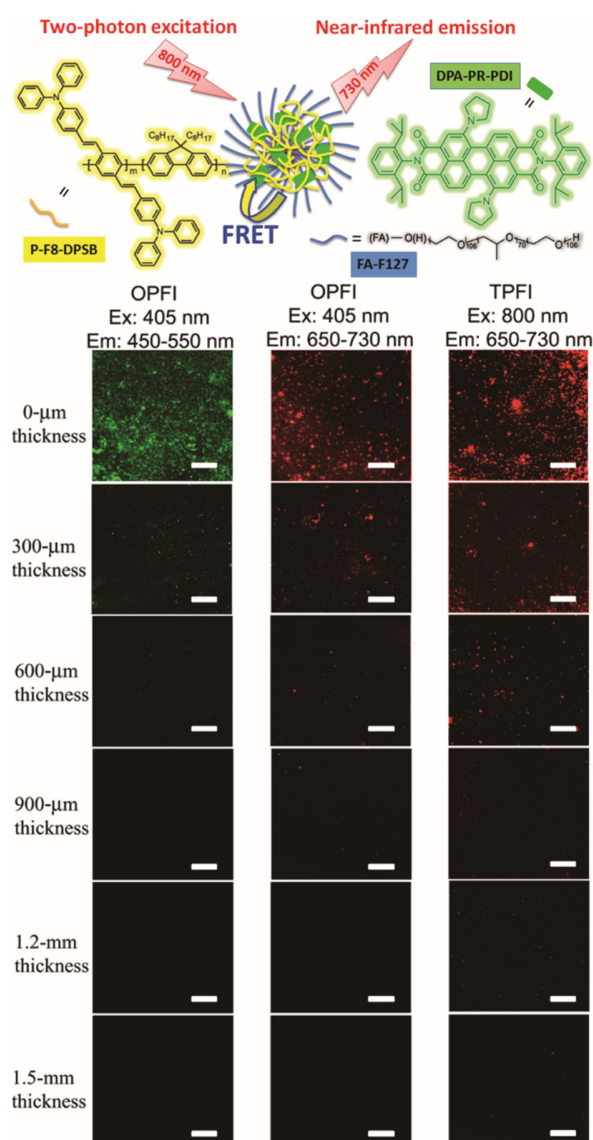
Figure 1.19 Chemical structures of the conjugated polymer with NIR fluorescent dye (DPA-PR-PDI), the amphiphilic polymer with folate moiety (FA-F127) used for the construction of the hybrid NPs, and illustration showing the NIR fluorescence emission of the NPs upon excitation using 800 nm pulse laser.

Evaluation of the penetration ability of hybrid fluorescent NPs for fluorescence imaging under different imaging modes. The scale bar refers to 100 μm.

Tian's research group synthesized a type of hybrid fluorescent nanoparticles with a Bis(diphenylaminostyryl)benzene (DPSB)-based conjugated polymer as energy donor and a peryleneimide derivative (DPA-PR-PDI) as energy acceptor[130]. The conjugated polymer showed a decent molar extension coefficient at 400 nm, as well as a two-photon absorption. The absorption of DPA-PR-PDI exhibited an overlap with the emission of the conjugated polymer, leading to FRET possible. An amphiphile, pluronic F127, was conjugated with folate ligand, a type of target agent which can specifically bind to folate receptors overexpressed on the surface of some cancer cells[131]. These three components were self-assembly into nanoparticles in PBS buffer with a nanoscaled dimension. These hybrid nanoparticles had a good stability and low cytotoxicity. Because of its NIR two-photon absorption and NIR emission, the signals could be detected through tissue with a thickness of 1.5 mm (Figure 1.19).

1.4.2. Activation in Target

Activatable fluorophores are a group of chemical compounds that can switch from a nonemissive to an emissive state, or from one emission wavelength to another one upon certain external stimuli. This unique property makes activatable fluorophores fit well with the goal of high contrast, compared to the "always-on" systems, as signals could be tuned to be respond to a specific target and avoid the washing process. Incorporate with the NIR dyes mentioned above, activatable NIR dyes have attracted intensive attention in bioimaging, but only a few are readily available owing to poor photostability and hydrophilicity, and difficulties of signal capture in heterogeneous tissues *in vivo*[132-137]. Extensive researches have been devoted to the redesign and modification of the existing

fluorescent skeletons to overcome these limitations. Great efforts have been made to develop new activatable NIR dyes with better photostability, high quantum yield and sensitivity.
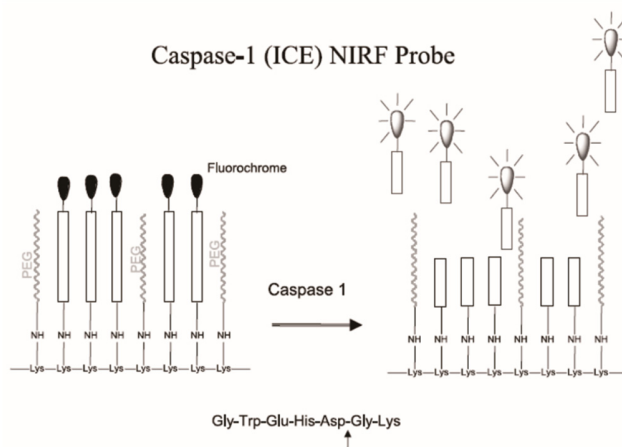
Figure 1.20 Schematic diagram of the ICE-NIRF probe. In its intact state (left), the high local density of fluorochromes causes substantial fluorescence quenching. The enzymatic activation by caspase-1, involving cleavage of the peptide substrate, results in release of the near-infrared fluorochrome, Cy5.5 (right).

There are some enzymes, which can catalyze one specific type of reactions, overexpressed in certain cells and can be used as a guidance for designing activatable NIR fluorophores. The transformation of a normal cell to an apoptotic ell is typically characterized by loss of cell volume, plasma membrane blebbing, nuclear chromatin condensation and aggregation, and endonucleocytic degradation of DNA into nucleosomal fragments[138]. Consequently, caspases are considered both initiators and executioners of apoptosis[139]. So, by detecting the existence of caspases, the process of cell apoptosis can be monitored. Messerli *et al.* synthesized a NIR probe based on the function of caspase-1[138]. They conjugated a NIR fluorophore, Cy 5.5, to a caspase-1-cleavalbe peptide through its C-terminal cysteine residue to generate the probe. The probe showed neglectable fluorescence, because of high

local fluorophores (Figure 1.20), when it was linked to the peptide. Upon activation, the

peptide was cleaved and a "turn-on" fluorescent signal was detectable (Figure 1.21).
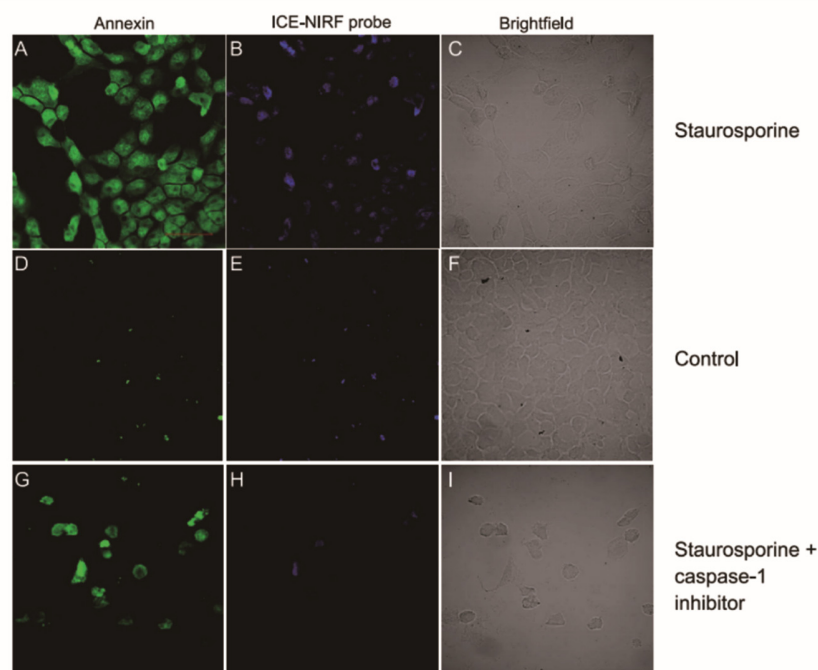
Figure 1.21 Induction of apoptosis with staurosporine resulting in activation of the ICE-NIRF probe. Gli36 cells were treated with 50 M staurosporine for 24 hours (A–C) or with the same percentage of DMSO (0.01%) to which experimental wells were exposed (D-488nm laser, E-633nm laser and F-bright field). To examine the role of caspase-1 in staurosporine-induced apoptosis and probe activation, cells were coincubated in caspase-1 inhibitor (10 M) and staurosporine (G–I). Staurosporine induces apoptosis, indicated by the positive annexin staining viewed with the 488-nm laser (A), which colocalized with activated probe viewed with the 633-nm laser (B). Coincubation of the caspase-1 inhibitor with staurosporine did not completely block apoptosis, indicated by the relatively higher number of apoptotic cells stained with annexin (G), as those that activated the probe (H).

1.4.3. Photoactivation for Cell Tracking

In previous sections, the general mechanisms require external factors or stimuli. But it can

cause unwanted complexities. Light, on the other hand, can provide potentially more facile

spatiotemporal control. To date, most light-triggered photoactivation processes have been

based upon the concept of photocaging.

Patterson et al. reported a photoactivatable Aequorea victoria green fluorescent protein (GFP)[140]. Before activation, the GFP showed neglectable fluorescent signal. After irradiation with 413 nm light, the neutral probe was transformed into an anionic state, enabled a 100-fold increasing of the GFP fluorescence at 520 nm. The fluorescent signal was stable for days under aerobic conditions and thus, making it a suitable tool for cell track *in vivo*. Sequentially, they used the photoactivatable GFP both as a free protein to measure protein diffusion across the nuclear envelope and as a chimera with a lysosomal membrane protein to demonstrate rapid interlysosomal membrane exchange. To be more specific, a small area of cells was irradiated with 413 nm laser and the fluorescent signal was tracked over time. Based on such a strategy, monitoring the development of small amount or even single cell temporally and spatially is possible.
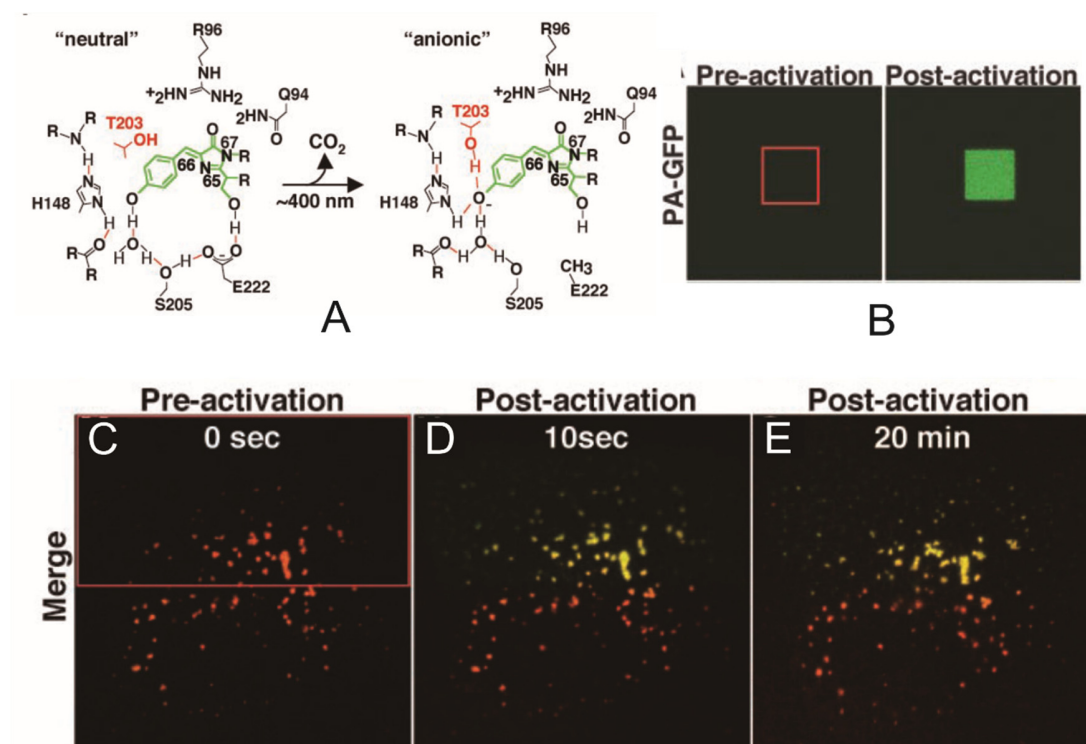
Figure 1.22 (A) Mechanism of photoactivation of GFP. (B) Purified PA-GFP was embedded in 15% polyacrylamide beneath a coverslip and imaged by using low levels of 488-nm excitation before (pre-

activation) and after 413-nm irradiation (post-activation) within the regions indicated by the red squares. (C to E) Cells expressing PA-GFP– lgp120 and loaded with rhodamine-labeled albumin were incubated on ice for 15 min in the presence of 5 μg/ml nocodazole. Merged images shown before, 10 s, and 20 min after photoactivation of the region indicated in red.

1.5. Scope of This Thesis

Extensive researches have been devoted to develop a suitable fluorophore, as well as a strategy with high SNR, for bioimaging applications. However, because of the hydrophobic nature of most fluorescent dyes, a guideline for developing the amphiphilic carrier should be investigated. Additionally, there's still room to improve fluorophores with better quantum yields, higher photostability and better water-solubility.

In the course of study, I have developed a family of polymers incorporating fluorescent chromophores based on an indole skeleton and their applications in bioimaging. In **chapter 2**, nine amphiphilic macromolecules with decyl and polyethylene glycol side chains, exhibiting different hydrophobic/hydrophilic ratio, polyethylene glycol length or molecular weight, were synthesized from radical polymerization. The polymers assemble into particles in neutral buffer and capture hydrophobic BODIPY in their interior. The relationship between critical concentration, dye loading property, hydrodynamic diameter and polymer structures were investigated. These provided a guideline to design self-assembling supramolecular hosts with for the encapsulation of fluorescent guests and can lead to ideal delivery vehicles for the imaging probes to target locations in biosystems[141].

In **chapter 3**, a halochromic coumarin-oxazine fluorophore was connected to the side chains of an amphiphilic polymer covalently, with folate ligands as targeting agents to MCF-7 cancer cells. The pre-fluorophores did not produce any detectable fluorescence at neutral pH, but are converted into fluorophores with red emission in acidic environment.

Control experiments showed the function of folic acid as no fluorescent signals are detected from folate-negative cells. Instead of covalently linking the pre-fluorophores, capsulation of probes inside micelles cannot distinguish folate-positive from -negative cells, because of leakage. Thus, this design offers the opportunity to highlight cancer cells selectively with high brightness and optimal contrast[142-143]. In **chapter 4**, we designed a photoactivatable BODIPY with two oxazines attached. As a result, the oxazine heterocycles can be disconnected stepwise upon UV irradiation and each product exhibit different emission bands. When relative amounts of chromophores are placed in a polystyrene bead matrix, the ratio of three component can be modulated by dose of activating photons. This ratiometric strategy can be applied to write barcode inside biosystems: different regions of a same animal can be labeled with different barcodes to allow the monitoring of the spatiotemporal tracking.

CHAPTER 2 Structural Implications on the Properties of Self-Assembling Supramolecular Hosts for Fluorescent Guests

2.1. Background

The covalent incorporation of hydrophobic and hydrophilic components within the same macromolecular skeleton results in the formation of amphiphilic polymers[83-85, 144]. In aqueous solutions at appropriate concentrations, these macromolecules can assemble into particles with nanoscaled dimensions. Noncovalent contacts between the hydrophobic domains of independent polymer chains bring multiple macromolecular components together in the form of discrete nanoparticles to avoid their direct exposure to water. Concomitant solvation of the hydrophilic counterparts ensures the dispersion of the resulting supramolecular assemblies in the aqueous medium and prevents their further association into large aggregates. In the process of assembling, the amphiphilic components can capture hydrophobic molecules and position them in the interior of the nanostructured assemblies. Once encapsulated, the molecular guests can be transported by their supramolecular host across hydrophilic environments. In fact, the unique properties of self-assembling nanoparticles of amphiphilic polymers can be exploited to transfer, otherwise insoluble, molecules into aqueous phases and carry them across physiological media to target locations in biological specimens. Indeed, these supramolecular constructs are becoming invaluable vehicles for the delivery of contrast agents and/or drugs in a diversity of diagnostic and/or therapeutic applications[101, 103, 106, 145].

Self-assembling nanoparticles of amphiphilic polymers can capture hydrophobic chromophores in their interior and transfer them into water[146]. The supramolecular host around the encapsulated molecular guests protects them from the aqueous environment

and, generally, preserves their photochemical and photophysical properties. In fact, this strategy permits the modular assembly of supramolecular constructs with multiple chromophoric subunits in close proximity and the engineering of photoresponsive systems with properties that would not be possible to replicate with the individual chromophoric components on their own[147-167]. In our laboratories, we followed similar experimental protocols to encapsulate fluorescent, photochromic and/or photocleavable guests inside such supramolecular hosts[90, 94, 124, 168-175]. We demonstrated that the photochemical and photophysical properties of the entrapped species can be exploited to (1) modulate fluorescence inside living cells with optical control[175], (2) image the resulting nanostructured constructs with subdiffraction resolution[170, 172-173], (3) monitor their ability to exchange their constituent components in the intracellular space[94, 124, 168, 174] and (4) probe their dynamics within hydrogels or developing embryos in real time[171]. In all these experiments, however, we relied exclusively on one structural design for the self-assembling amphiphilic building blocks. Specifically, we synthesized a poly(methacrylate) backbone with a random distribution of decyl and oligo(ethylene glycol) side chains. This particular polymer forms supramolecular hosts with fast kinetics in neutral buffer that are capable of entrapping a diversity of hydrophobic guests and transport them from the extracellular into the intracellular space. Such behavior is a consequence of the amphiphilic character engineered into the macromolecular construct, which, in turn, is related to the relative amount of hydrophobic and hydrophilic chains as well as to their lengths. In principle, the modification of these parameters should (1) have an influence on the ability of the amphiphilic components to associate, (2) control the physical dimensions and stability of the resulting supramolecular hosts, (3) dictate the

nature of the environment surrounding the entrapped guests and their exposure to the aqueous phase as well as (4) affect the cellular uptake and intracellular localization of the nanocarriers and their cargo. Thus, a systematic investigation of the influence that the structural design of the individual amphiphilic building blocks can have on the properties of the corresponding nanoparticles can provide fundamental insights on these fascinating supramolecular systems and, possibly, guide the optimization of these promising delivery vehicles. On the basis of these considerations, we envisaged the possibility of synthesizing homologous series of macromolecules, differing in their amphiphilic character, and investigating their ability to form supramolecular hosts for fluorescent guests in aqueous solutions. In this article, we report the preparation and structural characterization of these polymers together with spectroscopic investigations of their assembly into nanostructured hosts for borondipyrromethene (BODIPY) guests.

2.2. Results and Discussion

2.2.1. Design, Synthesis and Structural Characterization

Macromolecules **1** and **2** (Figure 2.1) incorporate a random distribution of hydrophobic and hydrophilic components along a common poly(methacrylate) backbone. They differ in the number of repeating units integrated within their oligo(ethylene glycol) chains (l in Figure 2.1). They were prepared by the radical co-polymerization of **3** and either **4** or **5**, under the influence of azobis(*i*-butyronitrile) (AIBN), in tetrahydrofuran (THF). In both instances, various amounts of **3** (0.05–3 mmol) were reacted with fixed aliquots of either **4** or **5** (0.5 mmol) and AIBN (0.03 mmol) at 75 °C for 3 days to produce polymers (**1a**, **1b**, **1d–f** or **2a–c** in Table 1) with a ratio between hydrophobic and hydrophilic components (*m*:*n* in Table 2.1 Structural parameters associated with **1a–f** and **2a–c**.) ranging from 8:1

to 1:3. For each macromolecule, *m:n* was estimated from the integrals of the resonances associated with the terminal methyl protons of the side chains in the corresponding ^{1}H nuclear magnetic resonance (NMR) spectrum. As an example, the ^{1}H NMR spectrum (Figure 2.1) of **1b**, recorded in deuterated chloroform, shows peaks at 0.88 and 3.39 ppm for the protons of the methyl groups at the termini of the hydrophobic and hydrophilic chains respectively with relative intensities corresponding to a *m:n* ratio of 4:1. Furthermore, the spectrum does not reveal any signals at chemical shifts greater than 5.0 ppm, where olefinic protons are expected to resonate, indicating that any unreacted methacrylate monomers are effectively separated from the corresponding polymer in the purification steps.
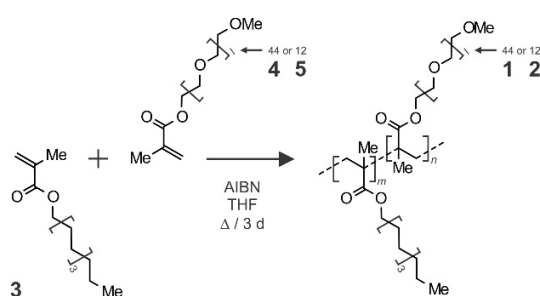
Figure 2.1 Synthesis of 1 or 2 from 3 and 4 or 5 respectively.

Table 2.1 Structural parameters associated with 1a–f and 2a–c.

	m:n [a]	M_n [b] (kDa)	PDI [b]	D_H [c] (nm)	W_S [d] (kDa)	I_S [c]	N_M [e]	C_c [f] (µg mL^{-1})
1a	6:1	19	1.28	36	1130	0.24	59	7.5
1b	4:1	21	1.32	26	580	0.25	26	16.7
1c	4:1	81	1.11	20	716	0.27	8.8	7.1
1d	1:1	21	1.16	10	53	0.51	2.5	19.3
1e	1:2	17	1.16	7	23	0.88	1.3	76.8
1f [g]	1:3	22	1.23	6	16	0.55	0.7	—
2a [h]	8:1	23	1.14	—	—	—	—	—
2b	3:1	19	1.26	14	109	0.24	5.7	12.9

| **2c** | 1:1 | 19 | 1.16 | 11 | 88 | 0.32 | 4.6 | 9.5 |

[a] The ratio ($m:n$) between the hydrophobic and hydrophilic components of each macromolecule was determined by ^{1}H NMR spectroscopy in CDCl$_3$. [b] The average number molecular weight (M_n) and polydispersity index (PDI) of the macromolecules were determined by GPC in THF against monodisperse polystyrene standards (2,700–200,000). [c] The hydrodynamic diameter (D_H) and "supramolecular" polydispersity index (I_S) of the nanoparticles were determined by DLS in PBS. [d] The average "supramolecular" weight (W_S) of the nanoparticles was determined by SLS in PBS. [e] The number (N_M) of macromolecules per nanoparticles is the ratio between W_S and M_n. [f] The critical concentration (C_c) was determined by emission spectroscopy in PBS and the presence of **6**. [g] **1f** is not able to solubilize **6** in PBS and the corresponding C_c could not be determined. [h] **2a** is not soluble in PBS and the corresponding D_H, W_s, I_S, N_M and C_c could not be determined. PDI and I_S quantify the widths of the distributions of the molecular weight of the individual macromolecules and the hydrodynamic diameter of the corresponding nanoparticles respectively. The former parameter is the ratio between the weight-average molecular weight and M_n determined by GPC (ref. 176). The latter parameter is the square root of the ratio between the standard deviation and DH (ref. 177).
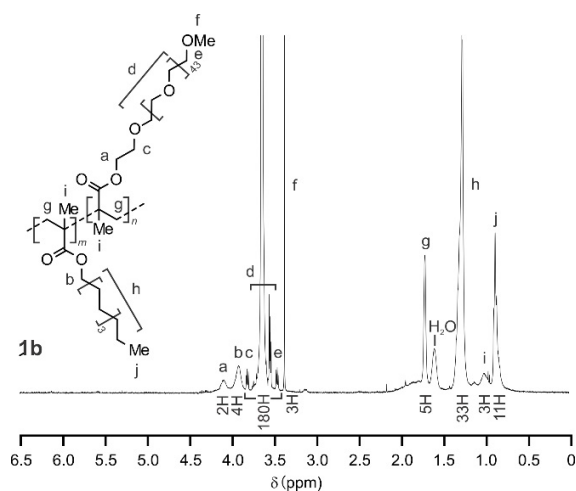
Figure 2.2 ^{1}H NMR spectrum (400 MHz, CDCl$_3$, 25 °C) of 1b.

Gel permeation chromatography (GPC) of THF solutions of **1a**, **1b**, **1d–f** and **2a–c** indicates their number-average molecular weight (M_n in Table 2.1) to range from 17 to 23 kDa with a polydispersity index (PDI in Table 2.1) varying from 1.14 to 1.32[176-177]. In order to assess the influence of M_n on the ability of the amphiphilic macromolecules to form nanoparticles, **3** and **4** were reacted in the presence of a tenth of the original amount

of AIBN, under conditions otherwise identical to those employed for the preparation of **1b**, to generate **1c**. The *m:n* of both polymers is 4:1, but the M_n of **1b** is only 22 kDa while that of **1c** is 81 kDa.

All macromolecules readily dissolve in aqueous solution with the exception of **2a**. This particular polymer has a *m:n* of 8:1 in conjunction with a *l* of 12. Therefore, it is the amphiphilic construct with the most pronounced hydrophobic character out of the nine macromolecules investigated. Dynamic light scattering (DLS) measurements (Figure 2.9) on phosphate buffer saline (PBS) solutions of the other eight polymers, at a concentration of 0.5 mg mL^{-1}, indicate the hydrodynamic diameter (D_H in Table 2.1) to range from 6 to 36 nm with a polydispersity index (I_S) varying from 0.24 to 0.88[176-177]. Interestingly, D_H increases linearly with *m:n* for **1** (Figure 2.3) and remains approximately constant for each polymer solution, maintained in the dark at ambient temperature, over the course of up to 4 days (Figure 2.10). A similar trend is observed also for the D_H of **2**, which drops from 14 to 11 nm with a decrease in *m:n* from 3:1 to 1:1. These results demonstrate that the hydrophobic character of these amphiphilic constructs controls their ability to aggregate into nanostructured particles in aqueous solution and that the physical dimensions of the resulting supramolecular assemblies increase with the relative content of hydrophobic components. Consistently, static light scattering (SLS) measurements reveal that the "supramolecular" weight (W_S in Table 2.1) of the resulting assemblies also increases monotonically with *m:n* (Figure 2.3) to range from 16 to 1130 kDa for **1**. The ratio between W_S and M_n for each polymer suggests that the average number (N_M) of amphiphilic components in each nanostructured assembly varies from 2.5 to 59 and, yet again, increases monotonically with *m:n*. For **1e** and **1f**, however, W_S and M_n are almost identical,

indicating that these particular polymers remain isolated in aqueous solution instead of assembling into supramolecular aggregates. In fact, they are significantly more hydrophilic than any of the other macromolecules with *m*:*n* of 1:2 and 1:3 respectively.
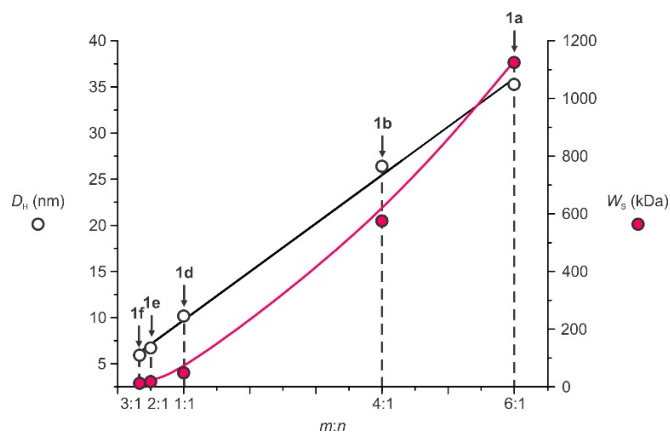
Figure 2.3 Dependence of D_H and W_S on m:n for **1a**, **1b** and **1d**–**f** (0.5 mg mL^{-1}) in PBS at 22 °C.

Comparison of **1b** and **1c**, which have the same *m*:*n* but different M_n, shows minor differences in D_H and W_S but a significant change in N_M. Up to 26 independent macromolecules are required on average to form a single nanoparticle of **1b**, while only 8.8 are sufficient for **1c**. Thus, the elongation of the macromolecular backbone of the individual amphiphilic building blocks reduces the number of separate components needed for the noncovalent assembly of one nanoparticle.

2.2.2. Noncovalent Encapsulation of Fluorescent Chromophores

The absorption and emission spectra of **6** in THF (Figure 2.4) show maxima at 524 and 536 nm respectively. Essentially the same bands are observed also if **6** is combined with appropriate amounts of **1a**–**e**, **2b** or **2c** in PBS (Figure 2.4). In fact, the wavelengths (λ_{Ab} and λ_{Em} in Table 2.2 Photophysical parameters for **6** encapsulated within nanoparticles of **1a**–**e**, **2b** and **2c**[a].) of the absorption and emission maxima detected in aqueous media, with the amphiphilic macromolecules, remain close to those measured in organic solution,

without the polymers. However, the amount of polymer required to enable the spectroscopic detection of the, otherwise insoluble, chromophore in PBS changes with the amphiphilic character of the macromolecular construct. For example, the emission intensity (Figure 2.4), detected after treating a fixed aliquot of **6** with PBS solutions containing increasing amounts of either **1a** or **1d**, raises abruptly above a critical concentration (C_c in Table 2.1) of either 7.5 or 19.3 µg mL^{-1} respectively. These observations suggest that the amphiphilic macromolecules form supramolecular hosts, capable of capturing the fluorescent guests and allowing their detection in the aqueous phase, only at concentrations greater than the corresponding C_c. In agreement with this interpretation, DLS measurements (Figure 2.5) show that D_H increases by one order of magnitude as the concentration of either **1a** or **1d** raises above the corresponding C_c. Interestingly, comparison of the C_c values determined with this protocol for **1a**, **1b**, **1d** and **1e** clearly indicates that this parameter increases with a decrease in *m:n*. Specifically, C_c varies from 7.5 to 76.8 µg mL^{-1} with a change in *m:n* from 6:1 to 1:2 (Table 2.1 Structural parameters associated with **1a**–**f** and **2a**–**c**.), suggesting that the hydrophobic content of the macromolecular constructs controls their ability to aggregate into supramolecular hosts for **6**. In fact, even relatively large concentrations of **1f**, which is the polymer with the most pronounced hydrophilic character, cannot solubilize the fluorescent chromophore in aqueous environments to allow its detection. In agreement with this interpretation, the stability of the nanocarriers and their ability to retain their fluorescent cargo also appear to vary with *m:n*. At concentrations greater than the corresponding C_c in PBS, the emission intensity detected for **6** in the presence of **1a** remains constant for hundreds of minutes (Figure 2.11), while it gradually decreases over time in the presence of **1e**. Thus,

nanocarriers of the polymer with a predominant hydrophobic character (*i.e.*, **1a**) retain their integrity and hold their cargo in the aqueous phase, while nanoparticles of the macromolecules with a predominant hydrophilic character (*i.e.*, **1e**) slowly lose their fluorescent guests with a concomitant decrease in the emission intensity.
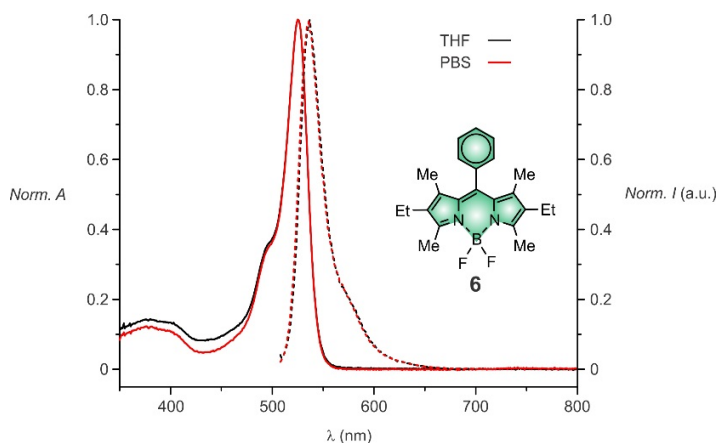
Figure 2.4 Normalized absorption and emission (λ_{Ex} = 500 nm) spectra of either **6** (1 µM) in THF or nanoparticles of **1a** (0.5 mg mL^{-1}), containing **6** (0.34 µM), in PBS recorded at 25 °C.

Table 2.2 Photophysical parameters for **6** encapsulated within nanoparticles of **1a–e**, **2b** and **2c**[a].

	λ_{Ab} [b] (nm)	λ_{Em} [b] (nm)	N_G [c]	ϕ [d]	K_{SV} [e] (M^{-1})
1a	526	538	0.63 (5.28)	0.59	72
1b	525	539	0.20	0.60	56
1c	525	538	0.47	0.72	—
1d	525	537	0.02	0.39	29
1e	526	539	0.005 (0.13)	0.09	8
2b	525	537	0.05	0.78	—
2c	525	539	0.04	0.73	—

[a] Absorption and emission spectra were recorded after combining CH$_2$Cl$_2$ solutions of **6** (0.1 mM, 1 µL for λ_{Ab}, λ_{Em}, N_G, ϕ and 10 µL for K_{SV}) and one of the polymers (2.5 mg mL^{-1}, 0.2 mL), distilling the solvent off under reduced pressure, dispersing the residue in PBS (1 mL) and passing the resulting dispersion through a nanoporous membrane. The concentration of **6** in the filtrate was estimated from the absorbance at λ_{Ab}, using the molar absorption coefficient measured for this compound in THF. That of the polymer was 0.5 mg mL^{-1} in all instances. [b] The wavelengths of the absorption (λ_{Ab}) and emission (λ_{Em})

maxima were determined in PBS at 25 °C. In THF without macromolecules, λ_{Ab} and λ_{Em} are 524 and 536 nm respectively. [c] The average number (N_G) of fluorophores per nanoparticle is the ratio between the molar concentrations of the molecular guests and the supramolecular hosts. The values listed in parenthesis for **1a** and **1e** were determined at the dye-loading (concentration of **6** = 2.3 µM) used for the lifetime (Figure 2.7) and FCS (Figure 2.8) experiments. [d] The fluorescence quantum yield (ϕ) was determined against a rhodamine 6G standard. In the absence of the macromolecules, ϕ is 0.73 and 0.50 for **6** and **8** respectively in THF and it is 0.58 for **8** in PBS. [e] The Stern–Volmer constant (K_{SV}) was determined from plots (Figure 2.16) of the relative emission intensity against the concentration of NaI in PBS at 25 °C. Under the same conditions without the macromolecules, K_{SV} is 14 M^{-1} for **8** (Figure 2.18).
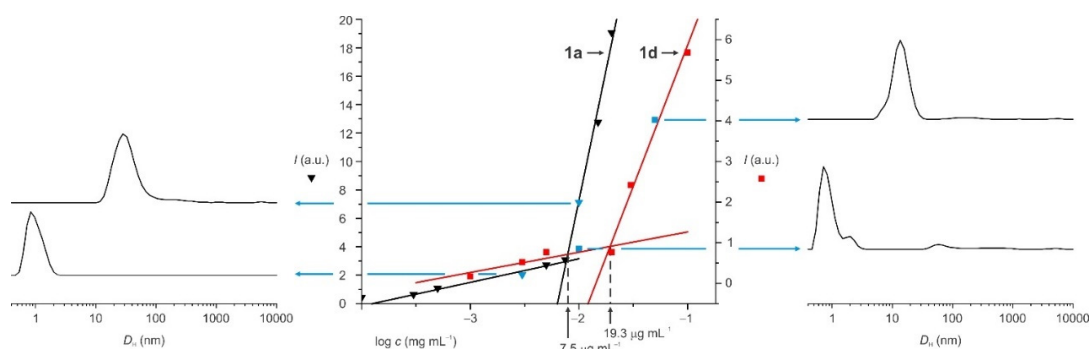
Figure 2.5 Plots of the emission intensity (λ_{Ex} = 500 nm, λ_{Em} = 540 nm), recorded at 25 °C after combining CH$_2$Cl$_2$ solutions of **6** (0.1 mM, 0.1 mL) and either **1a** or **1d** (25 µg mL^{-1}, 4–800 µL or 2.5 mg mL^{-1}, 12–25 µL), distilling the solvent off under reduced pressure, dispersing the residue in PBS (1 mL) and passing the resulting dispersion through a nanoporous membrane, against the polymer concentration and statistical distribution of D$_H$ at the four concentrations indicated in the chart determined by DLS.

Samples for the spectroscopic measurements (Table 2.2 and Figure 2.4) were prepared by combining aliquots of dichloromethane solutions of **6** and one of the amphiphilic polymers, distilling the organic solvent off under reduced pressure, dispersing the residue in PBS and filtering the resulting dispersion through a nanoporous membrane. In these particular experiments, the amount of fluorescent guest in the initial organic solution was 0.08% w/w, relative to the corresponding amphiphilic macromolecule. However, only a fraction of the water-insoluble fluorophores is captured by the water-soluble macromolecules and transported into the aqueous phase. Nonetheless, the concentration of **6** in the final

solutions can be determined from the absorbance at the corresponding λ_{Ab}, using the molar absorption coefficient measured in THF, to estimate the average number (N_G in Table 2.2) of fluorescent guests per supramolecular host. The resulting values of N_G range from 0.005 to 0.63 for **1a–d**, **2b** and **2c**. (The values of N_G are the ratios between the molar concentrations of the molecular guests, measured by absorption spectroscopy, and those of the supramolecular hosts, determined from the mass of corresponding polymer. As a result, these estimates assume that the molecular guests are evenly distributed across the entire population of supramolecular hosts. Alternatively, groups of guests can aggregate, when exposed to the aqueous solution, and the resulting aggregates can be encapsulated within a fraction of the nanocarriers, while the rest of the supramolecular containers remains empty. FCS and lifetime measurements are indicative of significant interchromophoric interactions and, therefore, are consistent with the latter interpretation.) These particular loading conditions ensure a relatively high fluorescence quantum yield (ϕ in Table 2.2). Indeed, ϕ varies from 0.39 to 0.78 and, in some instances, approaches the value determined for **6** in THF (*i.e.*, 0.78).

The behavior of **1e** is instead significantly different. This particular polymer has N_G and ϕ of only 0.005 and 0.09 respectively (Table 2.2) at identical loading conditions. Presumably, the pronounced hydrophilic character of this amphiphilic macromolecule limits the ability of the resulting supramolecular hosts to accommodate fluorescent guests and to protect them from the surrounding aqueous environment. In agreement with this interpretation, comparison of the dependence of the absorption and emission spectra (Figure 2.6) on guest loading for **1a** and **1e** shows significant differences. For the polymer with predominant hydrophobic character (*i.e.*, **1a**), the characteristic BODIPY absorption

grows with guest loading without shifting. The shape of the spectrum recorded at low guest loading is identical to that observed in either THF (Figure 2.4) or ethanol, indicating that **6** is present predominantly as a monomer inside the nanoparticles. At higher concentrations, however, the absorption spectrum shows an increase in the contribution of the shoulder at 495 nm. This trend is indicative of ground-state dimerization of the BODIPY chromophore[178] and is obvious from the bottom panel of Figure 6, which plots the ratio between the absorbance values (A_{495} and A_{527}) at 495 and 527 nm as a function of guest loading. Ratios (A_{495}/A_{527}) of 0.30 and 0.70 were measured in ethanol and in an ethanol/water (1:10, v/v) mixture respectively (Figure 2.12). The spectral characteristics of the dimer (*i.e.*, high A_{495}/A_{527} ratio) are evident even at low guest loading for the macromolecule with predominant hydrophilic character (*i.e.* **1e**). Even more, the band shifts bathochromically at high guest concentrations (Figure 2.12), indicating strong interchromophoric interactions that arise from exposure to the surrounding aqueous buffer. These interactions result in fluorescence self-quenching, as evidenced by the significantly lower fluorescence intensity measured at large guest concentrations (Figure 2.6) in **1e**, but not **1a**. Put together, these observations suggest that the chromophores remain fairly isolated from each other within nanoparticles of **1a** at moderate loading ratios, but not at high loads where the A_{495}/A_{527} ratio shows signs of aggregation. In the case of **1e**, on the other hand, pronounced electronic interactions in the ground state lead to changes in the absorption spectrum and depressive effects on the radiative efficiency, even at the lowest guest concentration investigated in this study.
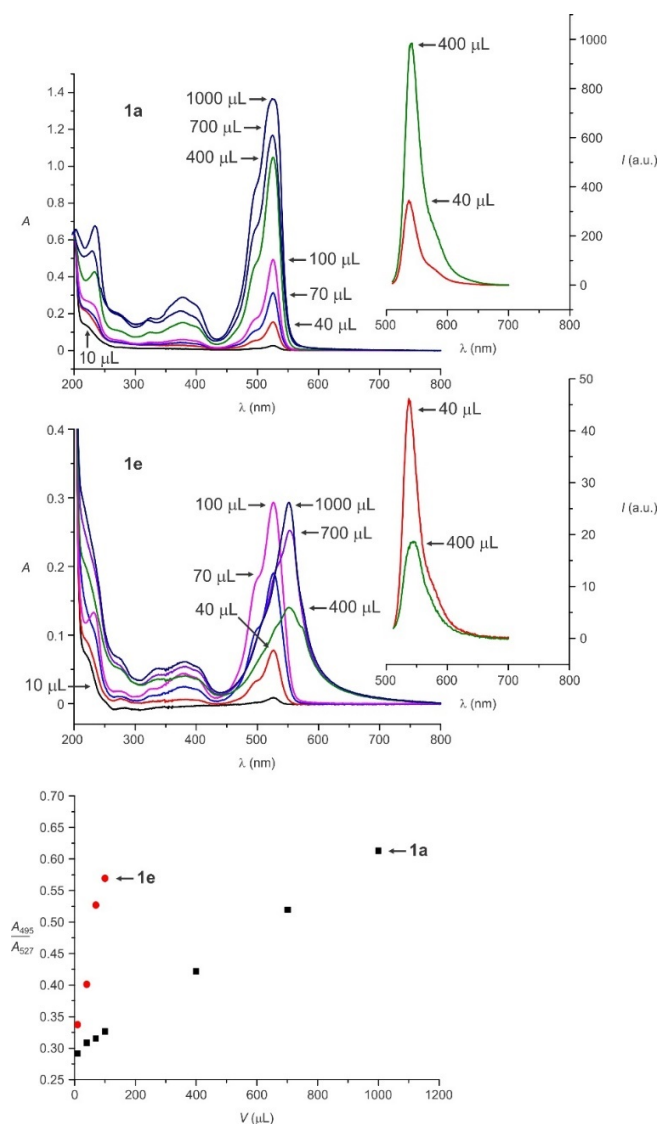
Figure 2.6 Absorption and emission (λ_{Ex} = 500 nm) spectra recorded at 25 °C after combining CH$_2$Cl$_2$ solutions of 6 (0.1 mM, volume indicated in the chart) and either 1a or 1e (1 mg mL^{-1}, 0.5 mL), distilling the solvent off under reduced pressure, dispersing the residue in PBS (1 mL) and passing the resulting dispersion through a nanoporous membrane. Plots of the ratio (A_{495}/A_{527}) between the absorbance values at 495 and 527 nm in the spectra for **1a** or **1e** against the volume of the initial solution of **6**. A value of 0.30 for A_{495}/A_{527} was measured in EtOH (monomeric BODIPY). Larger ratios indicate an increasing contribution of the dimer.

This conclusion is further supported by the results of time-correlated single photon counting (TCSPC) experiments, which show lifetimes that are highly dependent on guest loading and emission wavelength in the case of **1e**, but not **1a**. Two lifetimes (5.1 and 1.9 ns) were needed to fit the fluorescence decays of **6** incorporated into **1a**. The longest

lifetime is identical to the value measured in chloroform (5.1 ns) and its fractional contribution decreases slightly with increasing guest concentration (*a* in Figure 2.7). The fluorescence decays of **6** encapsulated inside **1e** are significantly different. A third short lifetime (<200 ps) is needed to fit the decays and the fractional contribution of this component increases with guest loading and increasing emission wavelength (*b* in Figure 2.7 and Table 2.3). The same dependence on guest concentration was observed in experiments with samples prepared independently containing different concentrations of **6**, and with samples prepared using a high concentration of **6** that were subsequently diluted with empty hosts. This result indicates that filled and empty hosts are able to interact and exchange their cargo, thus redistributing the concentrated dye in a larger number of hosts.
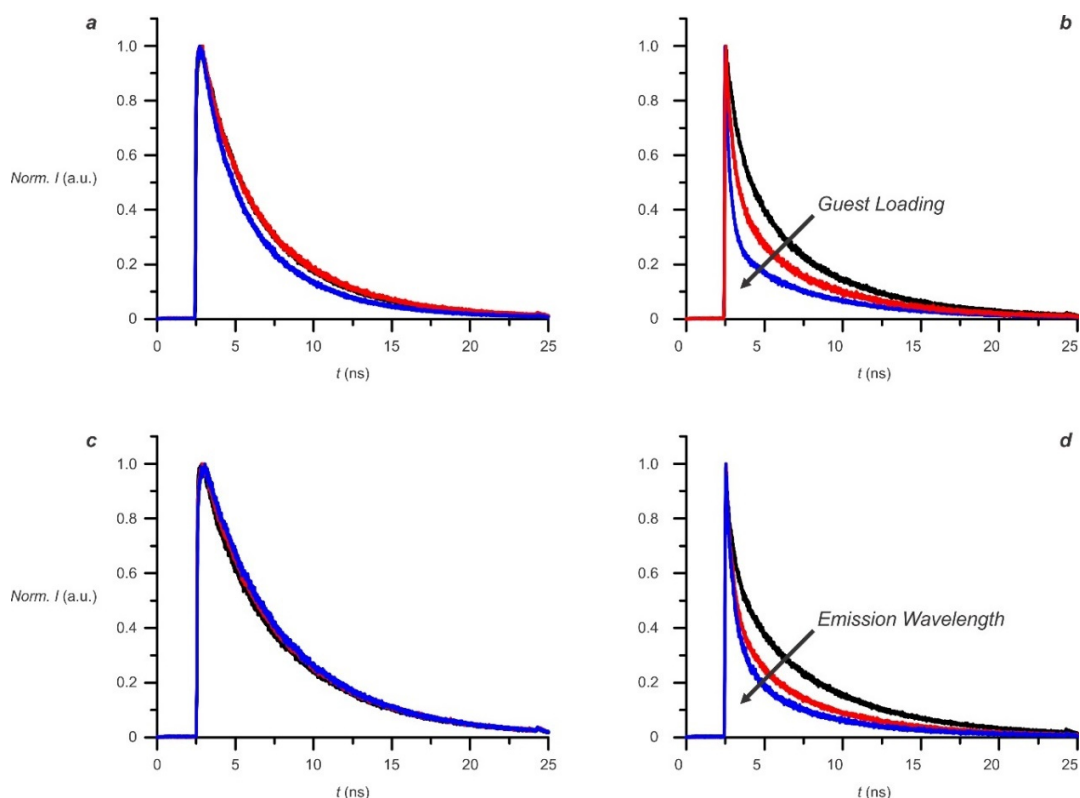
Figure 2.7 Fluorescence intensity decays of **6** encapsulated within nanoparticles of either **1a** (a and c) and **1e** (b and d) dispersed in PBS. Panels a and b show the effect of increasing guest loading and panels c and d show the effect of increasing emission wavelength. a: λ_{Ex} = 525 nm, λ_{Em} = 555 nm, concentration of **6** = 3.0

(blue), 1.9 (red) or 1.6 μM (black). b: λ_{Ex} = 525 nm, λ_{Em} = 555 nm, concentration of **6** = 2.3 (blue), 1.0 (red) or 0.5 μM (black). c: λ_{Ex} = 500 nm, concentration of **6** = 2.5 μM, λ_{Em} = 570 (blue), 550 (red) or 530 nm (black). d: λ_{Ex} = 500 nm, concentration of **6** = 1.0 μM, λ_{Em} = 570 (blue), 555 (red) or 540 nm (black). Decays were fitted with a sum of exponentials (Table 2.3).

The same wavelength-dependent behavior observed with **6** encapsulated in **1e** was also observed in measurements of **6** dissolved in an ethanol/water (1:10, v/v) mixture (Figure 2.13 and Table 2.3) and was also reported for a similar BODIPY in organic solvent/water mixtures[179]. This trend is consistent with the formation of excimers, which are formed when the hydrophobic chromophore is exposed to water. These interchromophoric interactions occur to a greater extent in **1e** than **1a**, because the hydrophilic character of the former polymer limits the ability of the supramolecular host to protect the fluorescent guests from the surrounding water molecules.

The difference between the environments that nanoparticles of **1a** and **1e** provide to the encapsulated chromophores is also evident from their response to the presence of quenchers in the surrounding aqueous medium. Specifically, the emission intensity of **6**, entrapped within nanocarriers of **1e** at a guest loading of 1.9% w/w, decreases to 57% (Figure 2.16) after the addition of 4,000 equivalents of NaI, relative to the BODIPY guest, and remains constant for hours. When **1a** is employed in place of **1e**, under otherwise identical conditions, the emission intensity drops to 36% (Figure 2.16), immediately after the addition of the quencher, and decreases further to a stationary value over the course of tens of minutes. The same experiment performed in the absence of macromolecules with a water-soluble analog of **6**, in the shape of **8** (compound **8** was prepared in one step from known precursors (Figure 2.11). Its absorption and emission spectra (Figure 2.12) show the characteristic bands of the BODIPY chromophore with negligible solvent dependence. ϕ

is 0.50 in THF and 0.58 in PBS (Table 2).), shows a behavior very similar to that observed for **1e**. The emission intensity decreases to 40% (Figure 2.16), but then remains constant for hours. These observations suggest that the hydrophobic character of **1a** slows access of the iodide quenchers to the BODIPY fluorophores, delaying the time required to reach a stationary state, but ultimately enhances quenching efficiency, leading to a pronounced fluorescence decrease. Consistently, Stern–Volmer plots, performed with equilibrated solutions of nanoparticles of **1a**, **1b**, **1d** and **1e**, containing **6** at a guest loading of 1.9% w/w in the presence of increasing amounts of NaI, show linear correlations (Figure 2.17) with a significant dependence of the slope on *m:n*. In particular, the Stern–Volmer constant (K_{SV} in Table 2.2) increases from only 8 M^{-1} for the most hydrophilic polymer (*i.e.*, **1e**) to 72 M^{-1} for the most hydrophobic macromolecule (*i.e.*, **1a**) (A similar analysis (Figure 2.15) indicates K_{SV} to be 20 M^{-1} (Table 2.2) for **8** in the absence of macromolecules.).

2.2.3. Fluorescence Correlation Spectroscopy

Fluorescence correlation spectroscopy (FCS) measurements were carried out using nanoparticles of **1a** and **1e**, containing **6** at different fluorophore/polymer ratios. Briefly, FCS is a technique that relies on the measurement of the fluorescence intensity fluctuations of a small number of molecules contained in an optically-restricted volume[180-181]. The temporal behavior of the measured fluorescence fluctuations are analyzed by means of the autocorrelation function (G(τ)), which contains dynamic information of the different processes that give rise to the measured fluctuations. Brownian motion is the main source of fluorescence fluctuations on the millisecond timescale, under the experimental conditions used in this work[181]. Therefore, the analysis of the measured autocorrelation function yields the diffusion coefficient of the diffusing particles (in this case the guest-

filled supramolecular hosts). The autocorrelation function of a solution containing N fluorescent species is described by:[181]

$$G(\tau) = \frac{\sum_{i=1}^{N} N_i B_i^2 \left(1 + \frac{4D_i\tau}{r_0^2}\right)^{-1}}{(\sum_{i=1}^{N} N_i B_i)^2} \qquad (1)$$

where τ is the correlation lag time, r_0 is the radial semiaxis of the Gaussian observation volume, N_i is the average number of molecules of species i in the observation volume, B_i is their molecular brightness, and D_i their diffusion coefficient. This equation assumes that the volume is elongated in the axial direction (*i.e.*, fluctuations in the axial direction do not contribute to the autocorrelation function), which is the case of our experimental setup. For a single species ($N = 1$), the amplitude of the autocorrelation function ($\tau = 0$ in Eq. 1) equals the inverse of the average number of particles ($G_0 = \langle N \rangle^{-1}$) present in the observation volume (V), and is related to the average concentration of diffusing particles (C) as $G_0 = (V N_a C)^{-1}$, where N_a is Avogadro's number. A value of $V = 7.4$ fL was obtained from the linear relationship between G_0^{-1} and C using 0.1–100 nM solutions of **6** in ethanol (inset in *a* of Figure 2.8). If species of different relative brightnesses are simultaneously present in the observation volume (*e.g.*, hosts containing different amounts of guests), G_0 takes the form:

$$G_0 = \frac{\sum_{i=1}^{N} N_i B_i^2}{(\sum_{i=1}^{N} N_i B_i)^2} = \frac{1}{(\sum_i N_i)} \frac{\langle B_i^2 \rangle}{\langle B_i \rangle^2} = \frac{1}{N_T} \frac{\sigma^2 + \mu^2}{\mu^2} \qquad (2)$$

Where σ^2 and μ are the variance and mean of the probability density function describing the distribution of brightnesses. Therefore, the inverse of G_0 gives an apparent number of particles that deviates from the true number of particles N_T by the factor $(1 + \sigma^2/\mu^2)^{-1}$.
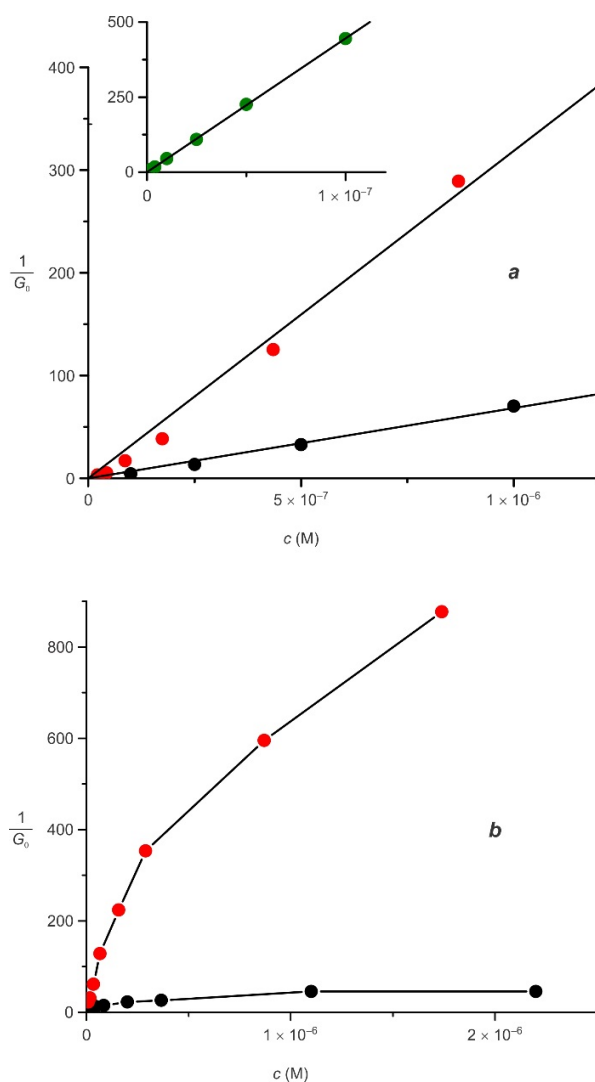
Figure 2.8 Plots of the inverse G_o values, obtained from fitting all autocorrelation decays to Eq. 1, against the concentration of **6**. (*a*) The nanoparticles were prepared with the highest guest concentration and were subsequently diluted with PBS buffer. (*b*) The nanoparticles were prepared with the highest guest concentration and were subsequently diluted with solutions of empty supramolecular hosts. Results for **1a** and **1e** are shown as red and black circles respectively. The inset in panel *a* shows data measured for **6** in EtOH. Lines in panel *a* are the result of linear regression. Lines in *b* are just visual guides.

Measurements with **6** incorporated into nanoparticles of either **1a** or **1e** resulted in FCS amplitudes that appeared to be off by more than one order of magnitude with respect to what was expected for a given concentration of dye (*a* in Figure 2.8). For example, the FCS amplitude of a 1 µM solution of **6**, encapsulated within nanoparticles of **1a**, was the

same as the amplitude measured with a 71 nM solution of **6** in ethanol. Taking into account that the observation volume measured with solutions of **6** in ethanol was 7.4 fL, and assuming that the distribution of guests follows a Poisson distribution and that the brightness of each nanoparticle is proportional to the number of guests, these results translate into an average number of guests per host of 13. This number is about five times higher than the average number of fluorophores per nanoparticle expected from the N_G values determined as the ratio between the molar concentrations of the molecular guests and the supramolecular host (Table 2.2). This is somewhat expected given that the absorption spectrum and fluorescence intensity decay of these nanoparticles already show signs of some aggregation, so it is likely that the brightness of each particle is not truly proportional to the number of encapsulated guests. The results of experiments with **6** incorporated into nanoparticles of **1e** (*a* in Figure 2.8) show even greater deviations from the values expected at a given concentration of dye. The ratio of the slopes of the measurements with **1e** and ethanol translates to 63 guests per host, which is implausible in light of the spectroscopic results that suggest that **1e** cannot accommodate fluorescent guests efficiently because of its hydrophilic character. The shape of the fluorescence intensity decay measured with these nanoparticles (*b* in Figure 2.7) suggests that the distribution of brightnesses is very broad, and that a significant fraction of particles will not be detected during data acquisition because of severe quenching. These two factors contribute to an apparent number of particles that is significantly lower than that measured with **1a** (Eq. 2).

All autocorrelation decays could be fitted with one diffusion term (Eq. 1), suggesting a narrow distribution of the nanoparticle dimensions consistently with the DLS

measurements. In addition, the position of the autocorrelation function does not change, when the samples are diluted sequentially using aqueous buffer (Figure 2.19). These observations show that the amount of free guests in the aqueous buffer is negligible. Significant amounts of free guests would give rise to a clear second faster component in the autocorrelation function, provided that the partition equilibrium between the nanocarriers core and the aqueous medium is slow compared with diffusion[182]. If the guest exchange is faster than the diffusion of either species, then the two species cannot be resolved by FCS and an average diffusion coefficient is obtained instead. In this case, the mean diffusion time is expected to increase with polymer concentration, as the free guest partitions into the supramolecular hosts[182]. These results are consistent with the very low solubility of **6** in PBS, which was determined to be less than 100 pM, and with energy-transfer experiments[168], which suggested that the hydrophobic chromophores do not separate from the amphiphilic polymers to escape into the bulk aqueous solution.

The results of the FCS experiments are significantly different if solutions of filled hosts are diluted with solutions of empty hosts, instead of buffer. In the experiments discussed above, sequential dilutions with buffer do not change the guest/polymer ratio, and because the hydrophobic chromophores are not soluble in the aqueous phase, the average number of molecular guests per supramolecular host does not vary upon dilution. This results in a linear change of the inverse amplitude of the autocorrelation function when the nanoparticles are diluted with PBS buffer (*a* in Figure 2.8). In this new set of experiments, solutions of guest-filled hosts were diluted with solutions of hosts prepared without guests (empty), in order to decrease the guest/polymer ratio while keeping the total concentration of polymer constant. As shown in *b* of Figure 2.8, the reciprocal of the FCS amplitude

(G_0^{-1}) does no longer increase linearly with guest concentration. The fact that diluting with empty hosts leads to markedly different results than diluting with aqueous buffer indicates that hosts containing guests exchange their cargo with empty hosts, which may lead to changes in the mean and variance of the distribution of particle brightnesses. For **1e**, the apparent number of particles in the observation volume does not change when particles containing a total of 2.2 µM BODIPY dye are diluted twofold, in sharp contrast to the factor of two expected because of the increase in the sample volume. A comparison between the TCSPC decays observed at high and low guest concentrations indicates that the distribution of lifetimes shifts to a lower average value and gets broader as the concentration of guest increases. Both effects contribute to the lower apparent number of particles observed at high guest concentrations, as observed experimentally (**b** in Figure 2.8). The curvature observed with **1a** is not as marked as with **1e**, which is consistent with the results of the spectroscopic experiments that show a lower degree of interchromophoric effects at the same dye concentration.

2.3. Conclusions

Amphiphilic macromolecules with a random distribution of decyl and oligo(ethylene glycol) side chains along a common poly(methacrylate) backbone can be prepared from the corresponding hydrophobic and hydrophilic methacrylate monomers under the influence of a radical initiator. The resulting macromolecules readily dissolve in neutral buffer, if the ratio (*m:n*) between their hydrophobic and hydrophilic components is lower than 8:1, and assemble spontaneously into particles with nanoscaled dimensions, when *m:n* is higher than 1:3. The hydrodynamic diameter (D_H) of the self-assembling nanoparticles ranges from 6 to 36 nm. Their supramolecular weight (W_S) varies from 16 to 1130 kDa.

The average number of macromolecules per nanoparticle (N_M) changes from 2.5 to 59. All three parameters (D_H, W_S and N_M) increase monotonically with $m{:}n$.

Hydrophobic BODIPY chromophores can be encapsulated within the hydrophobic interior of all self-assembling nanoparticles in neutral buffer, if the polymer concentration is greater than a critical value (C_c) ranging from 7.1 to 76.8 $\mu g\ mL^{-1}$ with the composition of the macromolecule. Specifically, C_c decreases as $m{:}n$ increases. When the average number (N_G) of encapsulated molecular guests per supramolecular host is lower than 0.63, the absorption and emission bands of the entrapped chromophores are identical to those observed in organic solvents and remain unaffected upon storage for days, as long as $m{:}n$ is greater than 1:2. At these loading conditions, the fluorescence quantum yield (ϕ_F) increases from 0.39 to 0.78 with $m{:}n$ and, for the polymer with the highest relative hydrophobic content, is essentially identical to that measured in THF. As the guest loading increases, interchromophoric interactions lead to significant changes in the shape of the absorption spectrum and a depressive effect on the radiative efficiency of the encapsulated guests. Consistently, the fluorescence of the entrapped chromophores decays multiexponentially with fractional contributions that change with guest loading and emission wavelength. Once again, these effects are also related to $m{:}n$. A decrease in the relative hydrophobic content tends to promote interactions between encapsulated guests and excimer formation can even be observed for the most hydrophilic supramolecular host. Similarly, an increase in the relative hydrophilic content also facilitates the access of hydrophilic quenchers to the encapsulated guests, which remain relatively shielded in the most hydrophobic supramolecular host instead.

FCS measurements confirm the entrapment of the small fluorescent guests into large supramolecular hosts and do not reveal any free fluorophores diffusing in the bulk aqueous solution. These experiments also show that groups of chromophores are entrapped within the same supramolecular container at high guest loading conditions, and that guests redistribute when mixed with empty hosts.

In summary, our results concur in demonstrating that m:n is the main structural parameter that ultimately controls the properties of these self-assembling supramolecular hosts. The tendency of the amphiphilic building blocks to form nanoparticles, the physical dimensions of the resulting assemblies and the ability of these supramolecular hosts to encapsulate fluorescent guests, while preserving their photophysical properties and shielding them from the surrounding environment, all increase with the relative hydrophobic content. Indeed, an excess of hydrophobic side chains, relative to their hydrophilic counterparts, is essential to produce optimal supramolecular hosts. When the former components are decyl chains, the latter are oligo(ethylene glycol) tails and the macromolecular backbone is a poly(methacrylate) scaffold, the best choice for m:n is a value of 6:1 in the shape of polymer **1a**. Thus, this particular structural composition appears to be the ideal one for the further development of our experimental protocols to deliver and operate photoresponsive molecules within live cells and developing embryos[90, 94, 124, 168-175].

2.4. Experimental Procedures

Chemicals were purchased from commercial sources and used as received. CH_2Cl_2 and MeCN were distilled over CaH_2. THF was distilled over Na and benzophenone. H_2O (18.2 $M\Omega$-cm) was purified with a Barnstead International NANOpure DIamond Analytical system. Compounds **3**, **4**, **6** and **7** (Figure 2.14) were prepared according to literature

procedures[175, 183-184]. GPC was performed with a Phenomenex Phenogel 5-μm MXM column (7.8 × 300 mm) operated with a Varian ProStar system, coupled to a ProStar 330 photodiode array detector, in THF at a flow rate of 1.0 mL min^{-1}. Monodisperse polystyrene standards (2,700–200,000) were employed to determine the M_n and PDI of the polymers from the GPC traces, following a literature protocol[185]. Matrix-assisted laser-desorption ionization (MALDI) mass spectra were recorded with a Bruker BioFlex IV spectrometer. NMR spectra were recorded with a Bruker Avance 400 spectrometer. DLS measurements were performed with a Malvern ZEN1600 apparatus. The values listed for D_H in Table 1 are averaged over ten independent experiments of ten runs of 10 s each. SLS measurements were performed with the same apparatus. The values of W_S listed in Table 1 were determined from the concentration dependence of the scattering intensity, following a literature protocol. Absorption spectra were recorded with a Varian Cary 100 Bio spectrometer, using quartz cells with a path length of 1.0 cm. Emission spectra were recorded with a Varian Cary Eclipse spectrometer in aerated solutions. Fluorescence quantum yields were determined with a rhodamine 6G standard, following a literature protocol[1].

Synthesis of 1a–e. A solution of **3** (**a** = 565 mg, 3 mmol; **b** and **c** = 452 mg, 2 mmol; **d** = 113 mg, 0.5 mmol; **e** = 23 mg, 0.1 mmol; **f** = 11 mg, 0.05 mmol), **4** (1.0 g, 0.5 mmol) and AIBN (**a**, **b** and **d**–**f** = 5 mg, 0.03 mmol; **c** = 0.5 mg, 0.003 mmol) in degassed THF (8 mL) was heated at 75 °C for 3 days in a sealed tube. After cooling down in an ice bath, the solvent was distilled off under reduced pressure. The residue was purified by column chromatography [SiO$_2$, CHCl$_3$/MeOH (40:1, v/v)] to give the corresponding polymer as a white solid.

1a (1.13 g): GPC: M_n = 19.0 kDa, PDI = 1.28. ^{1}H NMR (CDCl$_3$): δ = 0.84–0.93 (18H, br s), 0.97–1.09 (6H, br s), 1.22–1.39 (54H, br s), 1.69–1.77 (6H, br s), 3.37–3.41 (3H, s), 3.54–3.77 (~180H, m), 3.87–4.02 (7H, br s), 4.06–4.16 (2H, br s).

1b (813 mg): GPC: M_n = 21.0 kDa, PDI = 1.32. ^{1}H NMR (CDCl$_3$): δ = 0.84–0.93 (11H, br s), 0.97–1.09 (3H, br s), 1.22–1.39 (33H, br s), 1.69–1.77 (5H, br s), 3.37–3.41 (3H, s), 3.54–3.77 (~180H, m), 3.87–4.02 (4H, br s), 4.06–4.16 (2H, br s).

1c (613 mg): GPC: M_n = 81.0 kDa, PDI = 1.11. ^{1}H NMR (CDCl$_3$): δ = 0.84–0.93 (11H, br s), 0.97–1.09 (4H, br s), 1.22–1.39 (35H, br s), 1.69–1.77 (8H, br s), 3.37–3.41 (3H, s), 3.54–3.77 (~180H, m), 3.87–4.02 (4H, br s), 4.06–4.16 (2H, br s).

1d (745 mg): GPC: M_n = 21.0 kDa, PDI = 1.16. ^{1}H NMR (CDCl$_3$): δ = 0.84–0.93 (3H, br s), 0.97–1.09 (3H, br s), 1.22–1.39 (9H, br s), 1.69–1.77 (6H, br s), 3.37–3.41 (3H, s), 3.54–3.77 (~180H, m), 3.87–4.02 (1H, br s), 4.06–4.16 (2H, br s).

1e (710 mg): GPC: M_n = 17.0 kDa, PDI = 1.16. ^{1}H NMR (CDCl$_3$): δ = 0.84–0.93 (2H, br s), 0.97–1.09 (3H, br s), 1.22–1.39 (5H, br s), 1.69–1.77 (6H, br s), 3.37–3.41 (3H, s), 3.54–3.77 (~180H, m), 3.87–4.02 (1H, br s), 4.06–4.16 (2H, br s).

1f (548 mg): GPC: M_n = 22.0 kDa, PDI = 1.23. ^{1}H NMR (CDCl$_3$): δ = 0.84–0.93 (1H, br s), 0.97–1.09 (3H, br s), 1.22–1.39 (4H, br s), 1.69–1.77 (5H, br s), 3.37–3.41 (3H, s), 3.54–3.77 (~180H, m), 3.87–4.02 (1H, br s), 4.06–4.16 (2H, br s).

Synthesis of 2a–c. A solution of **3** (**a** = 1.13 g, 5 mmol; **b** = 262 mg, 1 mmol; **c** = 75 mg, 0.3 mmol), **5** (640 mg, 1 mmol) and AIBN (5 mg, 0.03 mmol) in degassed THF (8 mL) was heated at 75 °C for 3 days in a sealed tube. After cooling down in an ice bath, the solvent was distilled off under reduced pressure. The residue was purified by column

chromatography [SiO$_2$, CHCl$_3$/MeOH (40:1, v/v)] to give the corresponding polymer as a colorless oil.

2a (833 mg): GPC: M_n = 23.0 kDa, PDI = 1.14. ^{1}H NMR (CDCl$_3$): δ = 0.84–0.93 (36H, br s), 0.97–1.09 (7H, br s), 1.22–1.39 (115H, br s), 1.69–1.77 (5H, br s), 3.37–3.41 (3H, s), 3.54–3.77 (~52H, m), 3.87–4.02 (15H, br s), 4.06–4.16 (2H, br s).

2b (416 mg): GPC: M_n = 19.0 kDa, PDI = 1.26. ^{1}H NMR (CDCl$_3$): δ = 0.84–0.93 (10H, br s), 0.97–1.09 (3H, br s), 1.22–1.39 (24H, br s), 1.69–1.77 (3H, br s), 3.37–3.41 (3H, s), 3.54–3.77 (~52H, m), 3.87–4.02 (4H, br s), 4.06–4.16 (2H, br s).

2c (368 mg): GPC: M_n = 19.0 kDa, PDI = 1.16. ^{1}H NMR (CDCl$_3$): δ = 0.84–0.93 (4H, br s), 0.97–1.09 (3H, br s), 1.22–1.39 (9H, br s), 1.69–1.77 (2H, br s), 3.37–3.41 (3H, s), 3.54–3.77 (~52H, m), 3.87–4.02 (1H, br s), 4.06–4.16 (2H, br s).

Synthesis of 5. A solution of *N,N'*-dicyclohexylcarbodiimide (DCC, 4.6 g, 22 mmol) in CH$_2$Cl$_2$ (20 mL) was added dropwise, over the course of 20 min, to a solution of polyethylene glycol (M_n = 0.6 kDa, 12.0 g, 20 mmol), 4-dimethylaminopyridine (DMAP, 2.3 g, 20 mmol), and methacrylic acid (1.8 g, 22 mmol) in CH$_2$Cl$_2$ (100 mL) maintained at 0 °C. The reaction mixture was allowed to warm up to ambient temperature and then was stirred for 12 hours under these conditions. The resulting precipitate was filtered off and the solvent of the filtrate was distilled off under reduced pressure. The residue was purified by column chromatography [SiO$_2$, CH$_2$Cl$_2$/MeOH (10:1, v/v) to afford **5** (6.8 g, 53%) as a colorless oil. ESIMS: *m/z* =659 [M + H]$^+$. ^{1}H NMR (CDCl$_3$): δ = 1.89 (3H, s), 3.39 (3H, s), 3.50–3.72 (~44H, m), 4.25 (2H, s), 5.52 (1H, s), 6.08 (1H, s).

Synthesis of 8. A solution of **7** (106 mg, 0.3 mmol), poly(ethylene glycol) methyl ether (M_n = 2,000, 600 mg, 0.3 mmol), and 4-(*N,N*-dimethylamino)pyridine (DMAP, 31 mg, 0.3

mmol) in CH$_2$Cl$_2$ (30 mL) was stirred for 10 min at 0 °C. *N,N'*-Dicyclohexylcarbodiimide (DCC, 62 mg, 0.3 mmol) was added and the resulting solution was stirred for a further 30 min at 0 °C. The mixture was allowed to warm up to ambient temperature, stirred for 24 hours under these conditions and filtered. The filtrate was concentrated under reduced pressure and the residue was purified by column chromatography [SiO$_2$, CH$_2$Cl$_2$/ MeOH (95:5, v/v)] to give **8** (162 mg, 27%) as a red solid. MALDI: *m/z* = 2404 [M + H]$^+$; ^{1}H NMR (CDCl$_3$): δ = 8.20 (2H, d, 8 Hz), 7.42 (2H, d, 8 Hz), 4.00–3.51 (176H, m), 3.40 (3H, s), 2.53 (6H, s), 2.32 (4H, q, 8 Hz), 1.28 (6H, s), 1.00 (6H, t, 8 Hz).

Doped Polymer Nanoparticles. CH$_2$Cl$_2$ solutions of **6** (0.1 mM, 1–1000 µL) and one of the polymers (2.5 mg mL^{-1}, 0.2 mL or 1 mg mL^{-1}, 0.5 mL) were combined. The solvent was distilled off under reduced pressure, the residue was dispersed in PBS (1 mL) and the mixture was sonicated for 5 min. After storage for 10 min at ambient temperature, the dispersion was passed through a syringe filter with a pore size of 200 nm and the filtrate was used for the imaging and spectroscopic experiments without further purification. The concentration of **6** in the filtrate was estimated from the absorbance at λ$_{Ab}$ (Table 2), using the molar absorption coefficient measured for this compound in THF.

TCSPC. Lifetime measurements were performed in a TCSPC setup. The excitation light was a Fianium supercontinuum laser (SC-450-4-PP) operating at 20 MHz equipped with an Acousto-Optic Tunable Filter (AOTF) to select the excitation wavelength. A polarizer in the excitation pathway was used to excite the sample with vertically-polarized light. Samples were contained in standard 1 cm path length fluorescence cuvettes. The emission polarizer was set at the magic angle (54.7° with respect to the excitation) to eliminate artefacts in the data due to anisotropic properties, such as rotational diffusion. The

wavelengths of collected emission were selected by an emission monochromator and the signal was detected with a Hamamatsu MCP-PMT R3809U-50 photomultiplier tube. The TCSPC decay curves were recorded by a Becker and Hickl TCSPC Timing Card (B&H SPC830). All TCSPC decay curves were analyzed using ASUFIT, a MATLAB-based program developed at ASU that uses a standard deconvolution procedure and nonlinear regression. The instrument response function (IRF) was measured by scattering excitation light off of a 3% Ludox solution. Typically, the IRF was around 50–80 ps. The fluorescence intensity decay was fit to a sum of exponentials. The goodness of the fit was judged by the χ^2 value and the randomness of the residuals.

FCS. Measurements were carried out using a setup built in-house and described elsewhere[186-187]. Briefly, the instrument uses a continuous 532 nm Coherent Compass 215M-10 laser, an oil-immersion objective lens (Olympus Apochromat 100x/1.4 NA), avalanche photodiode detectors (Perkin Elmer SPCM AQR-14) and a dedicated hardware correlator card (ALV-5000/EPP Multiple Tau Digital Correlator). The samples were placed in silicone perfusion chambers on a glass coverslip. For every series of FCS measurements, the setup was calibrated with a rhodamine dye of known diffusion coefficient (TAMRA, 420 $\mu m^2\ s^{-1}$)[188-189]. Autocorrelation curves of free TAMRA were fit with Equation 1 with the known diffusion coefficient fixed in order to determine the radial semi-axis of the observation volume (r_0). The autocorrelation curves obtained with the micelles were then analyzed with the same equation to determine the diffusion coefficient (D).
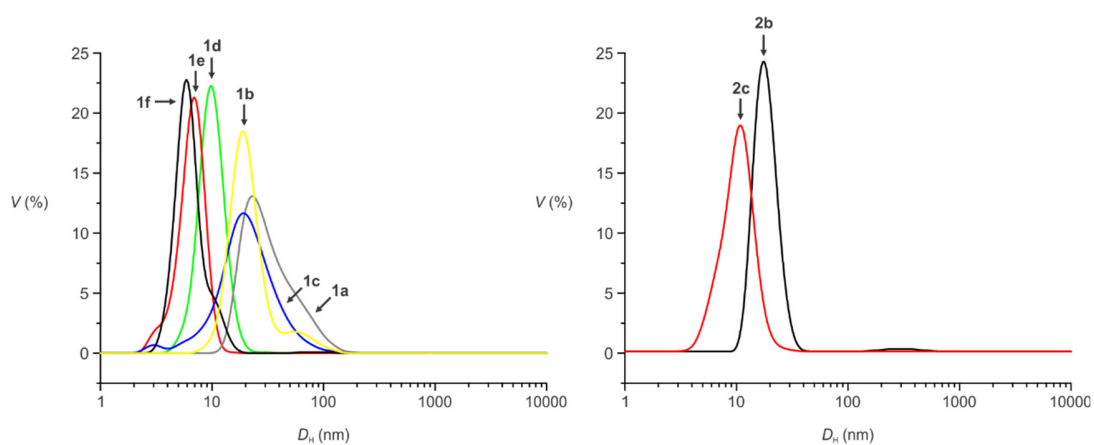
Figure 2.9 Statistical distributions of D_H for **1a–f**, **2b** and **2c** (0.5 mg mL^{-1}) determined by DLS in PBS at 22 °C.
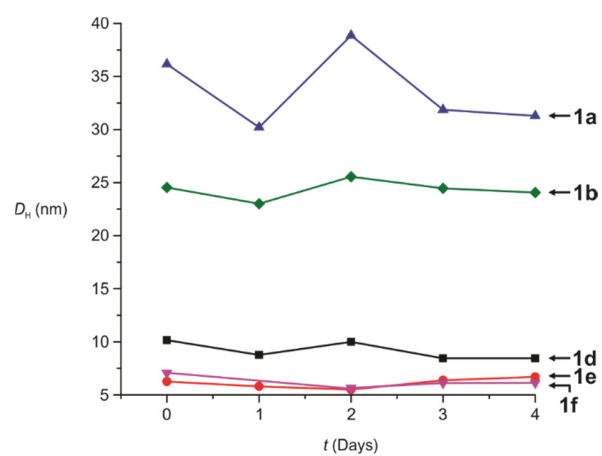
Figure 2.10 Temporal dependence of D_H for **1a**, **1b** and **1d–f** (0.5 mg mL^{-1}) in PBS at 22 °C.
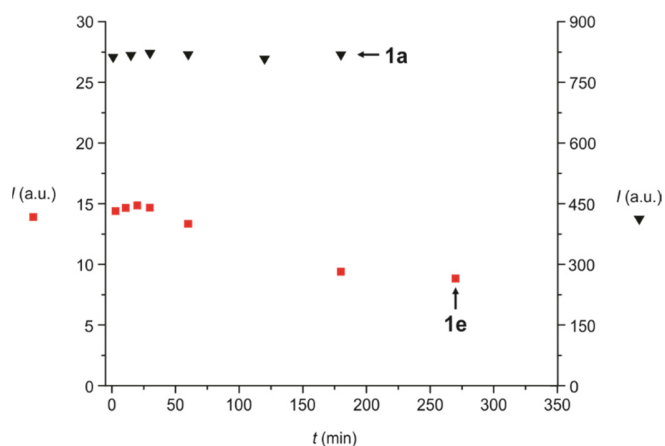
Figure 2.11 Emission intensity (λ_{Ex} = 500 nm, λ_{Em} = 540 nm) of nanoparticles of either **1a** or **1e**, containing **6** (6.6 µM for **1a** and 3.9 µM for **1e**), recorded in PBS at 25 °C.
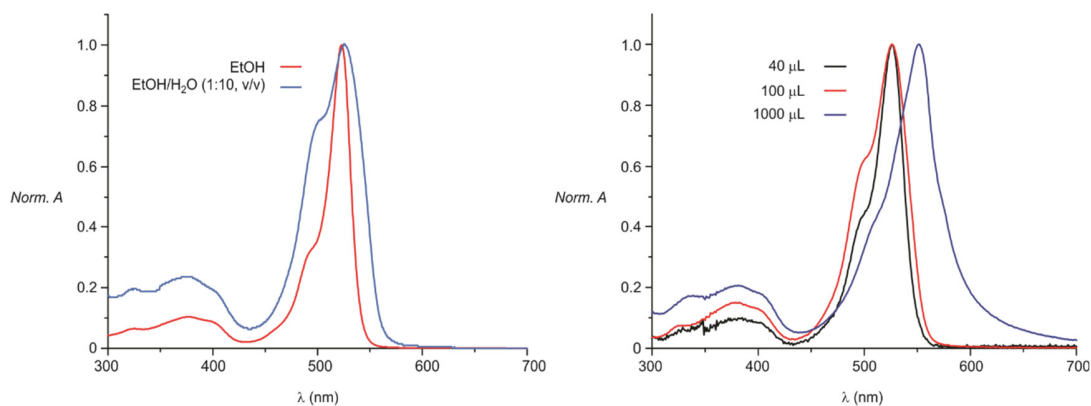
Figure 2.12 Normalized absorption spectra of **6** in EtOH, EtOH/H$_2$O (1:10, v/v) or after combining CH$_2$Cl$_2$ solutions of **6** (0.1 mM, volume indicated in the chart) and **1e** (1 mg mL^{-1}, 0.5 mL), distilling the solvent off under reduced pressure, dispersing the residue in PBS (1 mL) and passing the resulting dispersion through a nanoporous membrane.
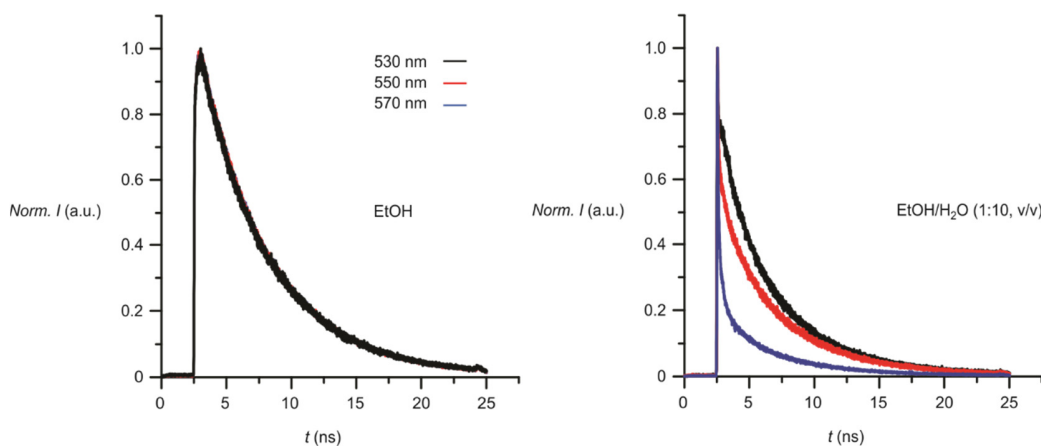
Figure 2.13 Fluorescence intensity decays [λ_{Ex} = 500 nm, λ_{Em} = 570 (blue), 550 (red) or 530 nm (black)] of 6 in EtOH or EtOH/H$_2$O (1:10, v/v). Decays were fitted with a sum of exponentials (Table 2.3).
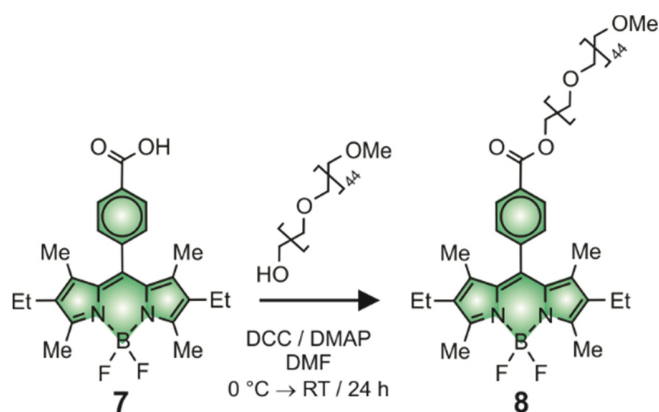
Figure 2.14 Synthesis of 8.
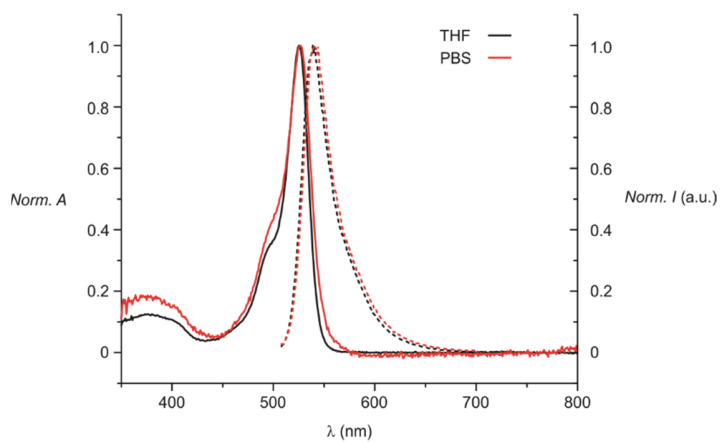
Figure 2.15 Normalized absorption and emission (λ_{Ex} = 500 nm) spectra of **8** in THF or PBS at 25 °C.
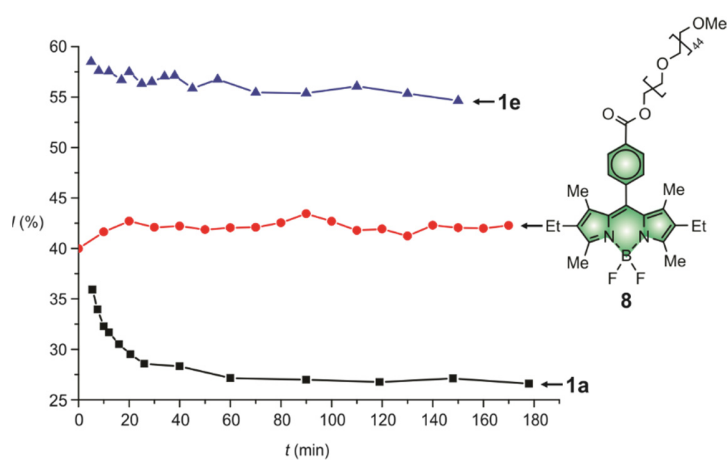
Figure 2.16 Temporal evolution of the emission intensity (λ_{Ex} = 500 nm, λ_{Em} = 540 nm) of nanoparticles of **1a** or **1e**, containing **6** (7.2 μM for **1a** and 2.8 μM for **1e**), recorded in PBS at 25 °C after the addition of NaI (0.1 mM) and reported relative to that measured in the absence of NaI, together with the relative emission intensity of **8** (0.1 mM) recorded after the addition of NaI (0.1 mM) under the same conditions.

Table 2.3 Fitting parameters [a] for the fluorescence decays of 6 [b].

	λ_{Ex} (nm)	λ_{Em} (nm)	τ_1 (ns)	%	τ_2 (ns)	%	τ_3 (ns)	%
1a (2.48 μM)	500	530	5.8	78	1.3	22%	—	—
	500	550	5.8	82	1.8	18%	—	—
	500	570	5.9	77	3.0	23%	—	—
1e (1 μM)	500	540	6.1	34	1.1	19%	0.1	47
	500	555	5.8	22	1.2	22%	0.2	56
	500	570	5.6	16	1.1	25%	0.2	59
1a (1.64 μM)	525	555	5.1	64	1.9	36%	—	—
1a (1.93 μM)	525	555	5.4	63	1.8	37%	—	—
1a (3.04 μM)	525	555	4.7	53	1.7	47%	—	—
1e (0.52 μM)	525	555	5.8	30	1.2	26%	0.08	44
1e (1 μM)	525	555	5.7	24	1.1	24%	0.2	52
1e (2.3μM)	525	555	5.8	14	0.7	17%	0.1	69
EtOH/H$_2$O (1:10, v/v)	500	530	5.0	14	1.5	7%	0.02	79
	500	550	5.1	19	1.3	7%	0.05	74
	500	570	4.8	6	0.7	6%	0.05	88
EtOH	500	530	5.3	100	—	—	—	—
	500	550	5.3	100	—	—	—	—
	500	570	5.2	100	—	—	—	—

[a] The fluorescence decays (Figure 2.7 and Figure 2.13) were fitted with one, two or three exponential terms, as needed to obtain random residuals. [b] The concentration of **6** is listed in parentheses for the experiments with **1a** and **1e**.
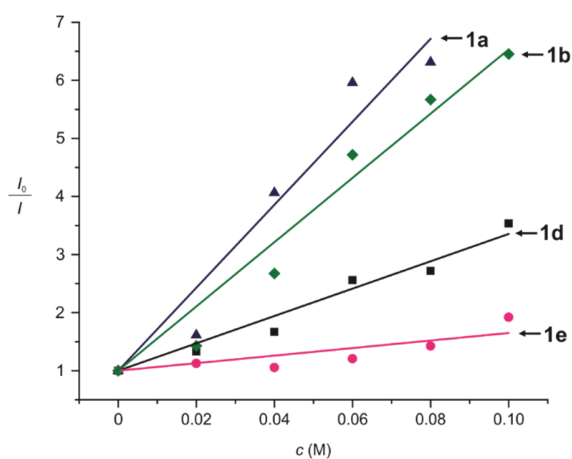
Figure 2.17 Plots of the relative emission intensity (λ_{Ex} = 500 nm, λ_{Em} = 540 nm) of nanoparticles of **1a**, **1b**, **1d** or **1e**, containing **6** (7.2 μM for **1a**, 7.8 μM for **1b**, 2.8 μM for **1d** and 2.8 μM for **1e**), recorded in PBS at 25 °C after the addition of increasing amounts of NaI and storage in the dark for 3 hours, against the iodide concentration.
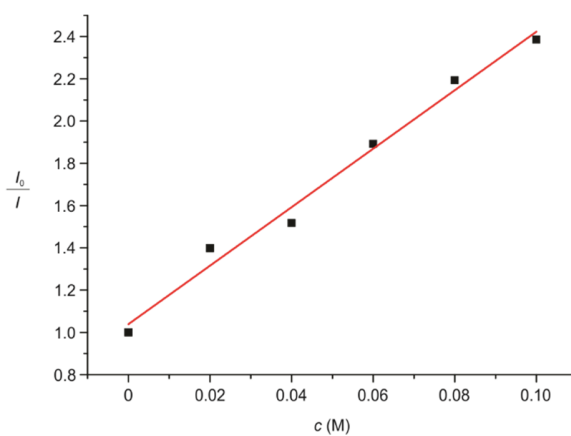
Figure 2.18 Plot of the relative emission intensity (λ_{Ex} = 500 nm, λ_{Em} = 540 nm) of **8** (25 μM), recorded at 25 °C in PBS and the presence of increasing amounts of NaI, against the iodide concentration.

Determination of an Upper Bound for the Solubility of 6 in PBS. First, EtOH solutions of **6** at different concentrations were prepared and the photon count rate of each solution was measured in the same FCS instrument used to acquire the autocorrelation functions reported in the manuscript. The lowest concentration with a photon count rate three times above the background was 100 pM and, therefore, it was concluded that the limit of detection of compound **6** in our instrument was 100 pM. Then, **6** was dissolved in PBS buffer and the photon count rate was measured in the same instrument. The result was indistinguishable from background, from which we conclude that the solubility of **6** in PBS is less than 100 pM.
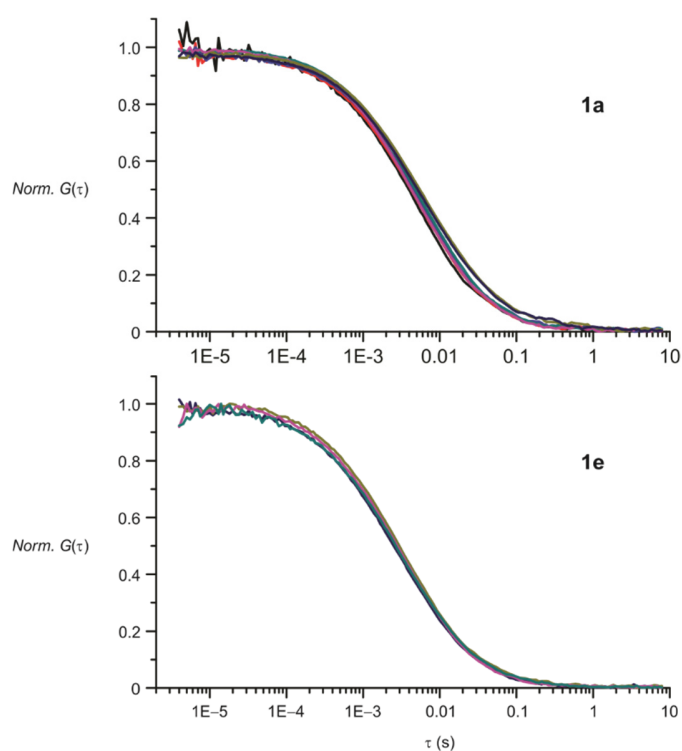
Figure 2.19 Autocorrelation decays of **6** incorporated into nanoparticles of either **1a** or **1e**. Samples were prepared using a concentration of 0.5 mg mL^{-1} for the polymer. The concentration of guest, after filtration, was 2.4 μM for **1a** and 1.0 μM for **1e.** The solutions were sequentially diluted using PBS buffer in 6 steps, until the concentration of polymer was 6.25 μg mL^{-1} (1:80) for **1a** and 50 μg mL^{-1} (1:10) for **1e** (the supramolecular hosts are not stable at lower polymer concentrations). Results show negligible changes in the autocorrelation function.

CHAPTER 3 Highlighting Cancer Cells with Halochromic Switches
3.1. Background

Cancer detection with fluorescence measurements requires first the development of probes with appropriate signaling and targeting capabilities[190]. Generally, these requirements are satisfied with the integration of a fluorophore and a ligand in the same construct. The former component should have a large molar absorption coefficient (ε) at the excitation wavelength (λ_{Ex}) in conjunction with a high fluorescence quantum yield (ϕ) to provide optimal brightness ($\varepsilon \times \phi$)[191]. The latter should recognize surface receptors expressed preferentially on cancer cells and associate with them selectively[192]. For example, folate receptors are overexpressed in *ca.* 40% of human cancers and bind folic acid with association constants approaching 10^{10} M^{-1} [193]. As a result, fluorescent derivatives of folic acid can mark selectively circulating tumor cells and malignant tissues[193]. The optical sensing of the former in blood through skin offers the opportunity to detect cancer noninvasively at early stages of its development[194]. The visual observation of the latter can facilitate the identification and surgical removal of tumors[195]. In fact, the potential of both methodologies has already been demonstrated with representative examples based on the covalent attachment of folic acid to fluorescent chromophores[196-203]. However, two fundamental problems, inherent to the photophysical properties of the signaling unit, limit the performance of these fluorophore–ligand constructs. The pairing of a *single* fluorophore to the targeting ligand restricts the brightness accessible per binding event to modest values. The concomitant emission of *unbound* probes contributes significant background fluorescence. Therefore, the relatively weak fluorescence of the probes bound

69

to the target must often be identified against an emissive background with detrimental consequences on the signal-to-noise ratio. Innovative signaling mechanisms to ensure high brightness with infinite contrast are very much needed to overcome these stringent limitations.

In principle, the complications associated with conventional labeling strategies can be avoided with the incorporation of *multiple* signaling units, designed to switch from a nonemissive to a fluorescent state upon binding the target, into a single construct. Under these conditions, only the *bound* probes can contribute fluorescence, ensuring optimal contrast, and their multichromophoric character can enhance ε, possibly imposing large brightness as well. The latter parameter, however, is equal to the product of ε and ϕ and interchromophoric interactions tend to depress, or even suppress completely, ϕ[204]. As a result, the brightness of multichromophoric assemblies generally remains relatively low, unless their size is increased sufficiently to maintain the fluorescent chromophores apart and retain an acceptable ϕ. In fact, the identification of structural designs to assemble compact multichromophoric constructs with bright fluorescence remains far from trivial[204-205] and the need to engineer switchable character on their emissive components can only complicate their realization even further. In this context, the fate of folate receptors, after binding derivatives of folic acid, is particularly convenient. These receptor–ligand complexes form on the outer surface of the cell membrane, but then are engulfed within endosomes to be transported inside the actual cell[193]. In proximity to the cell membrane the pH is close to neutrality, while it can be as low as 4.3 within the intracellular compartments[206]. Such a pronounced difference in pH can be exploited to induce the release cytotoxic drugs[207-209] as well as to activate chromophores for photodynamic

therapy[210] and contrast agents for magnetic resonance imaging[211]. Presumably, the very same pH change could be designed to alter the structure of a signaling unit and turn its fluorescence on exclusively after cellular internalization. Indeed, a seminal report[212] demonstrates that the pH in the acidic organelles of cancer cells can be exploited to suppress photoinduced electron transfer[213] and enhance the fluorescence of borondipyrromethene (BODIPY) chromophores internalized with the aid of a targeting antibody. Nonetheless, the contrast accessible with switching mechanisms based solely on the suppression of a quenching pathway remains inherently limited by the photophysical properties of the signaling component[214]. Unitary quenching efficiencies are hard, if at all possible, to achieve and, therefore, any quenched probe left in the extracellular matrix can contribute some level of background fluorescence. Infinite contrast can, instead, be achieved with activation mechanisms based on significant changes in the ability of the fluorescent chromophore to absorb exciting photons at λ_{Ex}[214]. Specifically, some organic chromophores modify their structure upon acidification to alter drastically their absorbance in the visible region of the electromagnetic spectrum with concomitant changes in color. This phenomenon, termed halochromism[215], is responsible for the operating principles of colorimetric indicators[216] and governs the behavior of pH-sensitive inks[217-219]. Furthermore, certain halochromic compounds alter also their emission properties, in addition to changing their ability to absorb visible light, and can be exploited to probe the intracellular environment with fluorescence measurements[220].

Our laboratory developed a family of molecular switches[221] with activatable fluorescence based on the halochromic opening of oxazine rings[222-223]. These pH-sensitive fluorophores permit the monitoring of proton diffusion in polymer films[224], the reconstruction of images

with subdiffraction resolution[224-225] and the probing of the intracellular environment[226]. Their halochromic transformations are designed to extend the electronic conjugation of a fluorescent chromophore over to an appropriate auxochromic unit and cause a pronounced bathochromic shift in absorption. The resulting spectral change can be exploited to excite the reaction product selectively, in the presence of the corresponding reactant, with concomitant emission. In fact, intense fluorescence is generated only after the halochromic activation of the molecular switch. This behavior suggests that our halochromic switches, in combination with the targeting ability of folic acid, should permit the selective labeling of cancer cells and their detection with optimal signal-to-noise ratios. In particular, the internalization of such halochromic–folate probes in the acidic organelles of target cells should result in the activation of the signaling chromophores to permit their selective excitation, even in the presence of relatively large amounts of their inactive counterparts in the extracellular space. Thus, these operating principles should allow the detection of the fluorescence of the internalized chromophores against an essentially dark background and translate into signal-to-noise ratios that cannot be replicated with activatable fluorophores solely based on the suppression of a quenching mechanism upon protonation[227-229]. In addition to contrast enhancement, a significant brightness increase, relative to conventional fluorophore–ligand constructs, should also be possible, if a viable strategy to integrate multiple halochromic components into a single assembly, without compromising their photophysical properties, is identified. These considerations suggested (1) the noncovalent encapsulation of multiple halochromic switches in their interior of self-assembling nanocarriers with folate ligands on their surface as well as (2) the covalent connection of such switchable chromophores and targeting ligands to a

common macromolecular scaffold. This article reports the preparation of these supramolecular assemblies and macromolecular constructs, their structural and spectroscopic characterizations as well as their response to folate-receptor negative and positive cells.

3.2. Results and Discussion

3.2.1. Design and Synthesis
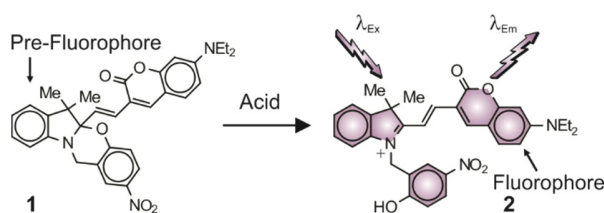
Figure 3.1 Conversion of pre-fluorophore **1** into fluorophore **2** under acidic conditions with concomitant fluorescence activation.

Compound **1** (Figure 3.1) combines a coumarin chromophore and an oxazine auxochrome within the same covalent skeleton[230]. Upon acidification in acetonitrile, the oxazine ring opens to form **2**[224]. This structural modification extends the electronic conjugation of the coumarin fragment over the adjacent 3H-indolium cation and shifts its main absorption bathochromically by more than 160 nm with a concomitant change in color. Because of such a pronounced spectral shift, illumination of the sample at an excitation wavelength (λ_{Ex} in Figure 3.1) positioned within the shifted band excites **2** selectively, even in the presence of an excess of **1**, to produce intense fluorescence at the corresponding emission wavelength (λ_{Em} in Figure 3.1). As a result, this halochromic transformation converts a pre-fluorophore into a fluorophore and activates fluorescence with infinite contrast in response to acidification. In principle, the identification of a viable strategy to replicate

this mechanism in aqueous media, under physiological conditions, might lead to sensing schemes for the signaling of intracellular acidic compartments with optimal contrast.

Compound **1** is essentially insoluble in water, but it can be transferred into aqueous solutions with the supramolecular assistance of amphiphilic polymers[231]. Specifically, reaction of **3** and **4** (Figure 3.2) in tetrahydrofuran (THF), under the influence of azobis(*i*-butyrronitrile) (AIBN), produces a poly(methacrylate) backbone with a random distribution of hydrophobic and hydrophilic side chains in the shape of **5** (The number average molecular weights (M_n) of **5**, **7**, **10**, **12** and **13** are 21.0, 16.7, 17.2, 17.8, and 18.9 kDa respectively. These values were determined by gel permeation chromatography (GPC). The ratio (*m:n* in Figure 3.2) between the hydrophobic and hydrophilic components of **5** is 3.5:1. This value was estimated by ^{1}H nuclear magnetic resonance (NMR) spectroscopy from the integrals of the resonances associated with the methyl protons at the termini of the side chains.). This amphiphilic macromolecule forms particles with nanoscaled dimensions in phosphate buffer saline (PBS) (The average hydrodynamic diameters of the nanoparticles formed by **5**, **8**, **12** and **13** in PBS are 26, 25, 17 and 24 nm respectively. These values were determined by dynamic light scattering (DLS) and do not change significantly, even after storing aqueous dispersions of the nanoparticles for up to 21 days at 25 °C in the dark (Figure 3.11). The critical concentrations, required for the formation of nanoparticles in PBS, of **5**, **8**, **12** and **13** are 21.4, 6.7, 15.0 and 14.5 $\mu g \ mL^{-1}$ respectively. These values were estimated from plots (Figure 3.12 and Figure 3.13) of the emission intensity of **20**, detected after treating a fixed amount of this water-insoluble fluorophore with increasing aliquots of the corresponding macromolecule in PBS, against the polymer concentration.). In the process of assembling, the nanoparticles can capture **1**

in their hydrophobic interior and transfer this, otherwise insoluble, pre-fluorophore into the aqueous phase.
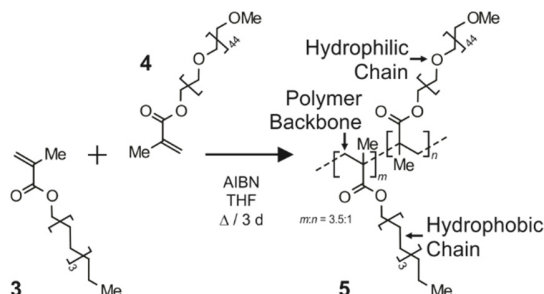
Figure 3.2 Synthesis of amphiphilic polymer 5.

The synthetic protocol for the preparation of **5** can be modified to allow the subsequent connection of folate ligands to part of the many oligo(ethylene glycol) side chains. In particular, reaction of **3**, **4** and **6** (Figure 3.3) in THF, with the assistance of AIBN, produces amphiphilic polymer **7** with primary amino groups at the ends of some of the hydrophilic tails. Treatment of **7** with folic acid in dimethylsulfoxide (DMSO), under the influence of *N*,*N'*-dicyclohexylcarbodiimide (DCC) and 4-dimethylaminopyridine (DMAP), couples folate ligands to a fraction of the primary amino groups to generate **8**. The resulting macromolecular construct readily dissolves in PBS to form particles with nanoscaled dimensions, capable of capturing **1** in their interior and transfer this pre-fluorophore into the aqueous phase, in analogy to the behavior of **5**.
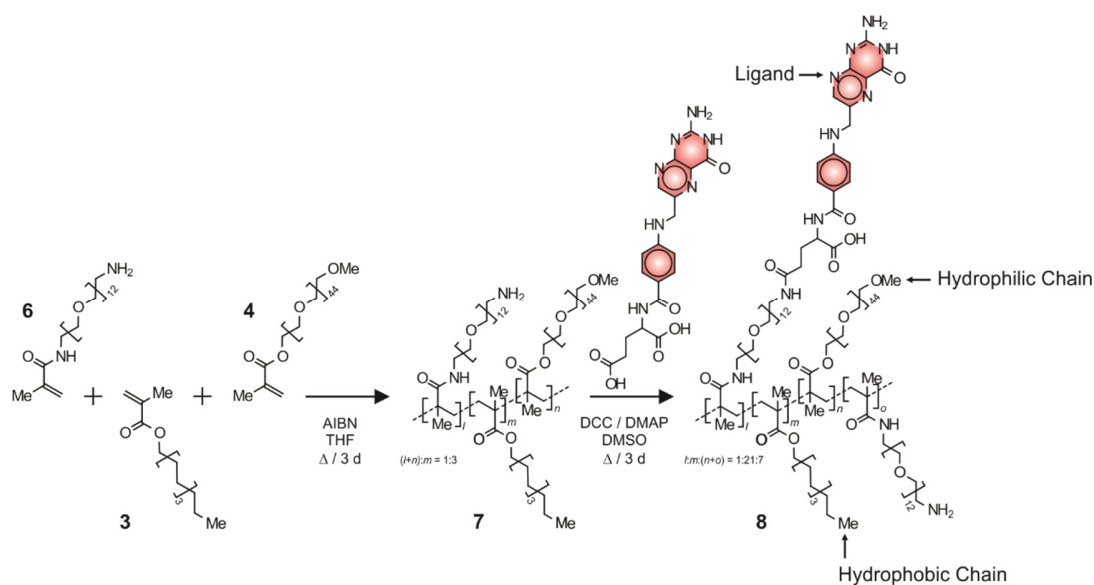
Figure 3.3 Synthesis of amphiphilic polymer **7** and covalent connection of folate ligands to form **8**.

In alternative to the noncovalent entrapment of pre-fluorophores within the hydrophobic interior of hydrophilic and nanosized hosts (Figure 3.2), the covalent attachment of switchable components to the polymer backbone of an amphiphilic macromolecule can be exploited to assemble water-soluble halochromic constructs. Specifically, the synthetic protocols for the preparation of **5** and **7** can be adapted to generate an amphiphilic polymer with azide groups at the termini of its hydrophobic side chains that can then be connected to appropriate derivatives of pre-fluorophore **1**. Indeed, reaction of **4**, **6** and **9** (Figure 3.4), in the presence of AIBN, produces **10**. The subsequent treatment of this macromolecule with **11** results in the covalent connection of an average of 2 pre-fluorophores per polymer chain in the shape of **12**. Further reaction of the resulting polymer with folic acid, in the presence of DCC and DMAP, couples folate ligands to some of the primary amino groups to produce **13**.
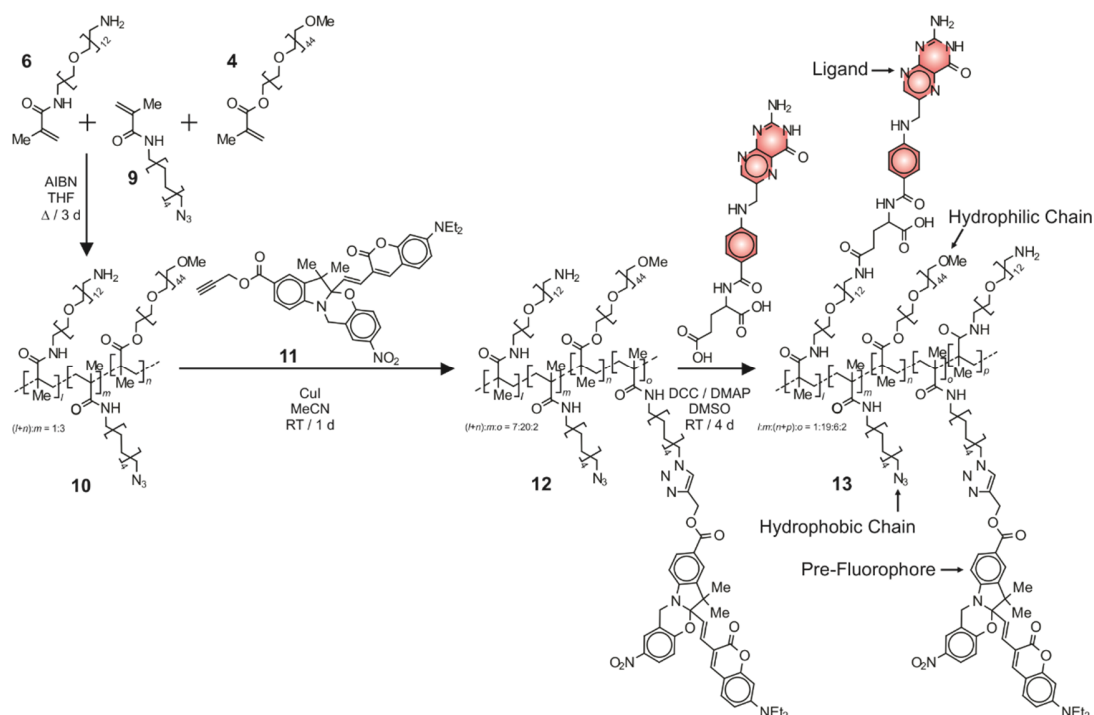
Figure 3.4 Synthesis of amphiphilic polymer **7** and covalent connection of folate ligands to form **8**.

3.2.2. Absorption and Emission Spectroscopies

In the presence of sufficient amounts of either **5** or **8** to form nanosized hosts, 1 readily dissolves in neutral buffer. The corresponding absorption spectra (*a* and *b* in Figure 3.5) show the characteristic band of the coumarin chromophore at 414 nm ($^P\lambda_{Ab}$ in Table 3.1). The absorbance at this particular wavelength indicates the average number (*N* in Table 3.1) of pre-fluorophore guests per nanoparticle host to be 23 in both instances. This absorption is essentially identical to that recorded for an acetonitrile solution of **1**, in the absence of any amphiphilic polymer (Figure 3.14), and remains unchanged, even after storing aqueous dispersions of the loaded nanoparticles for hours at 25 °C in the dark (Figure 3.15). These observations indicate that (1) the environment within the interior of the nanosized hosts is similar to an organic solvent and (2) the supramolecular nanocarriers retain their cargo for prolonged periods of time.
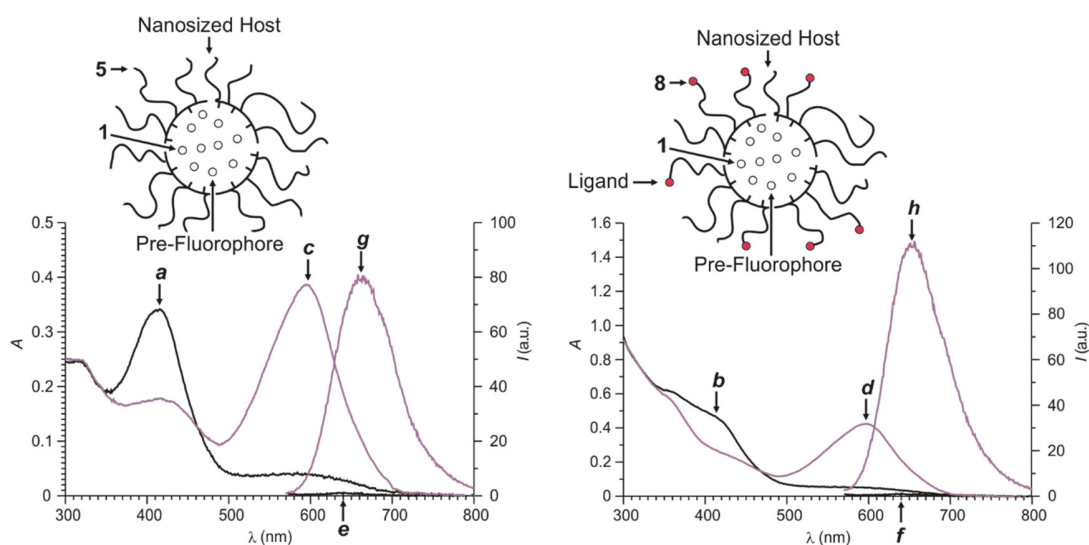
Figure 3.5 Absorption and emission (λ_{Ex} = 560 nm) spectra of **1** and **5** in buffer at a pH of 7.15 (*a* and *e*) or 4.01 (*c* and *g*) and of **1** and **8** in buffer at a pH of 7.15 (*b* and *f*) or 4.01 (*d* and *h*).

Table 3.1 Photophysical parameters for 1 and 11–13 [a].

	Solvent	$^P\lambda_{Ab}$ (nm)	$^F\lambda_{Ab}$ (nm)	N	ε (mM^{-1} cm^{-1})	λ_{Em} (nm)	ϕ	$\varepsilon \times \phi$ (mM^{-1} cm^{-1})
1	MeCN	411	593	1	46.1	660	0.06	2.7
1 + 5	H$_2$O	414	596	23	1053	658	0.20	208
1 + 8	H$_2$O	414	596	23	1046	656	0.25	265
11	MeCN	410	613	1	69.9	669	0.03	1.9
12	H$_2$O	423	626	61	4245	660	0.07	289
13	H$_2$O	411	623	75	5238	667	0.09	456

[a] The wavelength of the absorption maximum for the pre-fluorophore ($^P\lambda_{Ab}$) was determined at 25 °C in either MeCN or phosphate buffer with a pH of 7.15 for **5** and **8** or 6.88 for **12** and **13**. The wavelength of the absorption ($^F\lambda_{Ab}$) and emission (λ_{Em}) maxima for the fluorophore and its fluorescence quantum yield (ϕ) were determined at 25 °C in either MeCN, after the addition of CF$_3$CO$_2$H (1.0 eq. for **1** or 10 eq. for **11**), or phosphate buffer with a pH of 4.01 for **5** and **8** or 3.02 for **12** and **13**. The number (N) of pre-fluorophores per nanoparticle was estimated from the absorbance at $^P\lambda_{Ab}$. The molar absorption coefficient (ε) listed for **1** and **11** was measured at $^F\lambda_{Ab}$ in MeCN, after the addition of CF$_3$CO$_2$H (1.0 eq. for **1** or 10 eq. for **11**). Those reported for **5** and **8** are the products of N and the ε listed for **1** in MeCN. Those reported for **12** and **13** are the products of N and the ε listed for **11** in MeCN. The parameters reported for **1** in H$_2$O were determined in the presence of either **5** or **8** at a pre-fluorophore loading of 0.1%w/w, relative to the polymer.

The oxazine ring of **1** opens to generate **2** (Figure 3.1) in the interior of the nanoparticles of either **5** or **8**, when the pH of the surrounding aqueous solution is lowered to 4.01. This structural transformation brings the coumarin chromophore in conjugation with the

adjacent 3*H*-indolium auxochrome and shifts its absorption to a wavelength ($^F\lambda_{Ab}$ in Table

3.1) of 596 nm (*c* and *d* in Figure 3.5). Once again, the absorbance at this wavelength

remains constant for hours (Figure 3.15), if the solution is maintained at 25 °C in the dark,

indicating that the supramolecular assemblies remain intact also under these conditions.

Furthermore, the pronounced bathochromic shift in absorption, which accompanies the

conversion of **1** into **2**, permits the selective excitation of the latter with concomitant

fluorescence. Specifically, illumination of the sample at a λ_{Ex} of 560 nm does not produce

any fluorescence at a pH of 7.15 (*e* and *f* in Figure 3.5), but results in intense emission at a

pH of 4.01 (*g* and *h* in Figure 3.5). In fact, the fluorescence intensity at the wavelength

(λ_{Em} in Table 3.1) corresponding to the emission maximum becomes significant only at pH

values lower than 6.0 for both supramolecular assemblies (*a* and *b* in Figure 3.6).
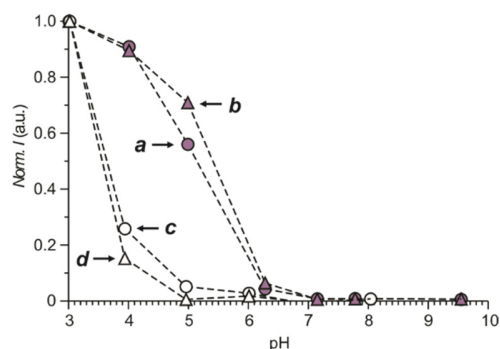
Figure 3.6 Plots of the fluorescence intensity measured at the emission maximum for **1** and **5** (*a*), **1** and **8** (*b*), **12** (*c*) or **13** (*d*) against the pH of the buffer.

In acetonitrile, pre-fluorophore **1** switches to fluorophore **2** quantitatively, after the addition

of only 1 eq. of CF_3CO_2H. Under these conditions, ε at $^F\lambda_{Ab}$ and ϕ for 2 are 46.1 mM^{-1}

cm^{-1} and 0.06 respectively (Table 3.1). These values correspond to a brightness of 2.7

mM^{-1} cm^{-1} ($\varepsilon \times \phi$ in Table 3.1). Encapsulation of **2** within nanoparticles of either **5** or **8**

does not affect the absorption band of the 3*H*-indolium chromophore of the former (Figure

3.14), suggesting that the entrapment of the fluorescent guest within the nanosized host has a negligible effect on ε. The supramolecular container, however, discourages the nonradiative deactivation of the excited state and raises ϕ to 0.20 for **5** and 0.25 for **8**. This significant increase, in conjunction with the presence of multiple fluorophores within each supramolecular host, corresponds to a brightness per nanoparticle of 208 mM^{-1} cm^{-1} for **5** and 265 mM^{-1} cm^{-1} for **8**. Thus, the clustering of multiple fluorophores within the same supramolecular assembly translates into an enhancement in brightness of two orders of magnitude, relative to the individual fluorophores dissolved in organic solvent. Additionally, these results demonstrate the photophysical properties of the fluorescent guests to be almost identical in the two sets of nanosized hosts, suggesting that the presence of folate ligands in **8** has negligible influence on the entrapped fluorophores.

The absorption spectrum (Figure 3.16) of **12** in neutral buffer also shows the characteristic band of the coumarin chromophore at a $^P\lambda_{Ab}$ of 423 nm. Comparison of the spectrum of **12** in neutral buffer to that of **11** in acetonitrile (Figure 3.14), however, shows a bathochromic shift of 13 nm (Table 3.1) in the $^P\lambda_{Ab}$ of the polymer. This change suggests that the environment around the chromophore differs in the two instances. The further covalent connection of folate ligands to the macromolecular backbone to produce **13** results instead in a hypsochromic shift of $^P\lambda_{Ab}$ back to 411 nm (Table 3.1 and Figure 3.16). Presumably, this structural modification alters the polymer conformation and the environment around the coumarin chromophore. The behavior of **11**–**13** appears to be in contrast with that of **1**, whose spectral response in acetonitrile is identical to that observed within nanoparticles of either **5** or **8** dispersed in neutral buffer. Thus, covalent connection, in one instance, and the noncovalent encapsulation, in the other, impose distinct spectral

outputs on the pre-fluorophore. Furthermore, the structural design of **12** and **13** results in the incorporation of more pre-fluorophores per nanoparticle than in the case of **5** and **8**. Specifically, the absorbance at $^P\lambda_{Ab}$ indicates N to be 61 and 75 for **12** and **13** respectively. Under acidic conditions, the oxazine rings of the pre-fluorophores incorporated within **12** and **13** open with the concomitant appearance of the characteristic absorption (Figure 3.16) for the corresponding fluorophores at a $^F\lambda_{Ab}$ of 626 and 623 nm respectively (Table 3.1). Once again, the pronounced bathochromic shift in absorption, observed upon acidification, offers the opportunity to excite selectively the protonated forms at a λ_{Ex} of 560 nm. In fact, fluorescence at a λ_{Em} of 660 and 667 nm respectively (Table 3.1) is observed, under these illumination conditions, only after changing the pH from 6.88 to 3.02 (Figure 3.16). The pH dependence of the emission intensity observed for **12** and **13** (*c* and d in Figure 3.6), however, differs from that recorded for nanoparticles of **5** or **8**, containing **1**, (*a* and *b* in Figure 3.6). The fluorescence intensity raises abruptly below pH thresholds of *ca.* 5 for the covalently-connected pre-fluorophores and *ca.* 6 for the noncovalently entrapped counterparts. This difference parallels the behavior of **1** and **11** in acetonitrile (Figure 3.14). Only 1 eq. of CF_3CO_2H is sufficient to switch **1** quantitatively to **2**, while up to 10 eq. are required to convert **11**. Presumably, the electron withdrawing carboxylic ester in position 5 of the 3*H*-indole heterocycle of **11** has a depressive effect on the stability of the cationic chromophore that has to be formed with the opening of the oxazine ring upon protonation. The very same functional group has a depressive effect also on ϕ, which decreases with substitution from 0.06 for **1** to 0.03 for **11** (Table 3.1). However, the covalent incorporation of **11** into **12** or **13** also increases ϕ significantly (Table 3.1), as observed for the noncovalent encapsulation of **1** within nanoparticles of either **5** or **8**.

Presumably, the close proximity of the fluorescent chromophore to the macromolecular construct in all instances restricts its conformational freedom, relative to acetonitrile solution, discourages the nonradiative deactivation of its excited state and, ultimately, enhances ϕ. Specifically, ϕ raises to 0.07 for **12** and 0.09 for **13**. This change, together with the presence of multiple fluorophores within each supramolecular assembly, corresponds to a brightness per nanoparticle of 289 mM^{-1} cm^{-1} for **12** and 456 mM^{-1} cm^{-1} for **13**.

3.2.3. Fluorescence Imaging

Literature data[232-233] indicate that Human Embryonic Kidney 293 (HEK-293) and Michigan Cancer Foundation 7 (MCF-7) cells are folate-negative and -positive respectively. Despite the significant difference in the ability of these cells to express the folate receptor, their incubation with nanoparticles of either **5** or **8**, containing **1**, for only 1 hour causes intense intracellular fluorescence in all instances (*a–d* in Figure 3.7 and Figure 3.17 and Figure 3.18). These observations suggest that the noncovalently-entrapped pre-fluorophores can reach acidic intracellular compartments of both cell types on a relatively short timescale, even in the absence of folate ligands on the surface of their nanocarriers, and then switch to the corresponding fluorophores to produce fluorescence. The rather surprising behavior of the nanocarriers with noncovalently-encapsulated cargo is, presumably, a result of the discharge of the hydrophobic pre-fluorophores into the plasma membrane of the cells and their subsequent internalization in acidic intracellular compartments. Indeed, similar supramolecular hosts have been observed to dump their water-insoluble guests into the plasma membranes of the cellular blastoderm of *Drosophila melanogaster* embryos[234]. The separation of the signaling units from the macromolecular

components is, instead, impossible for the nanostructured constructs with covalently-connected pre-fluorophores. In fact, incubation of either HEK-293 or MCF-7 cells with nanoparticles of **12**, which lack folate ligands on their surface, does not result in any detectable intracellular fluorescence (*e* and *f* in Figure 3.7 and Figure 3.19), under otherwise identical conditions. Essentially the same result is also observed when the folate-
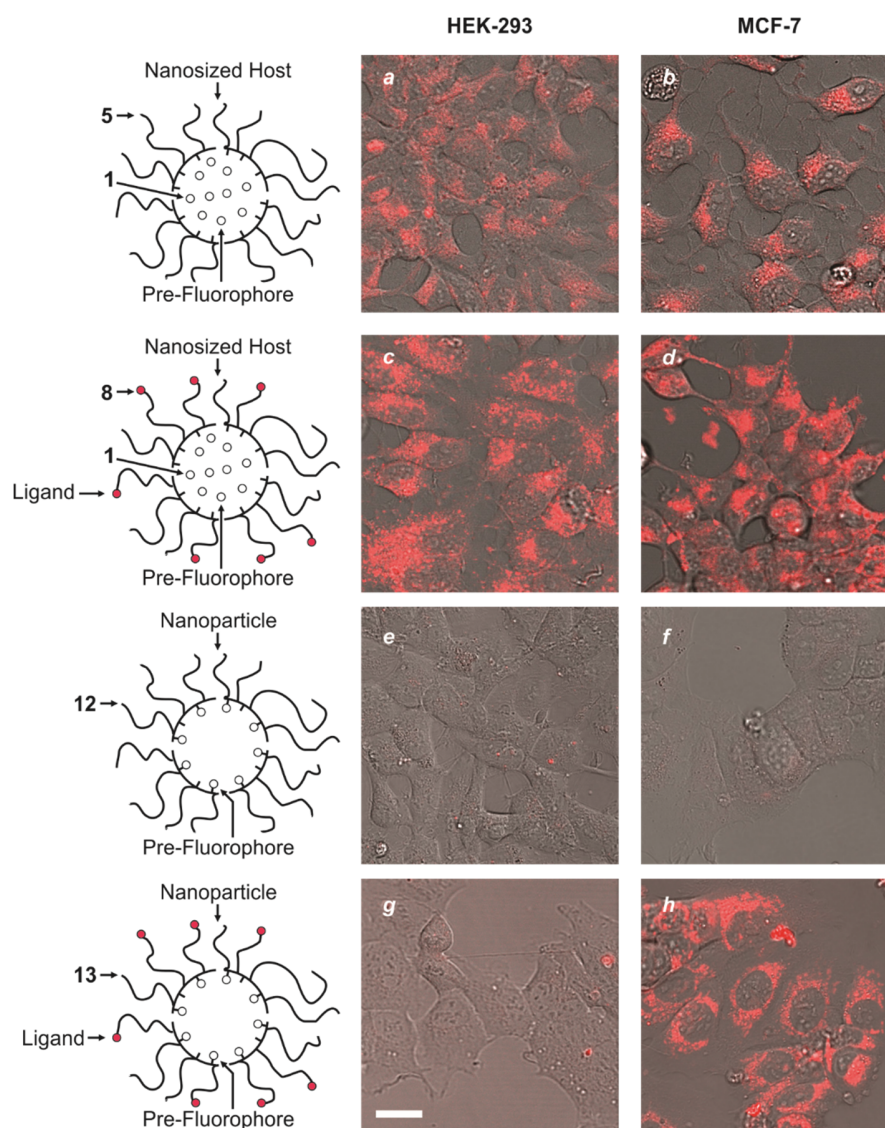
Figure 3.7 Overlaid fluorescence and transmittance images (λ_{Ex} = 561 nm, λ_{Em} = 575–750 nm, scale bar = 25 μm) recorded after incubation of HEK-293 and MCF-7 cells with PBS solutions of either **1** and **5** (*a* and *b*) or **1** and **8** (*c* and *d*) for 1 hour or with PBS solutions of **12** (*e* and *f*) or **13** (*g* and *h*) for 2 hours.

negative cells are incubated with nanoparticles of **13** (***g*** in Figure 3.7 and Figure 3.20).
Instead, intense intracellular fluorescence appears when these nanostructured constructs,
which incorporate folate ligands on their surface, are incubated with the folate-positive
cells (***h*** in Figure 3.7 and Figure 3.20). Furthermore, comparison of the intracellular
fluorescence intensities detected for HEK-293 and MCF-7 after increasing incubation
times with **13** shows that the emission remains negligible for the folate-negative cells but
increases dramatically for the folate-positive ones (Figure 3.21). These observations
demonstrate that the pre-fluorophores covalently connected to the amphiphilic polymers
can reach acidic intracellular compartments *only if* the macromolecular backbone is also
connected to folate ligands. In agreement with the ability of these ligands to mediate the
internalization of the activatable emitters, the addition of increasing amounts of folic acid
to the extracellular matrix causes a decrease in the fluorescence intensity detected
intracellularly (Figure 3.21). Indeed, folic acid competes with **13** for the folate receptors
of the MCF-7 cells and inhibits the intracellular transport of the pre-fluorophores.

The halochromic character engineered into the emissive components of **13** ensures the
activation of their fluorescence exclusively after internalization in the target cells. Indeed,
the corresponding image (***h*** in Figure 3.7) shows negligible extracellular emission.
Comparison to a model fluorophore–ligand construct (**14** in Figure 3.8), which incorporates
a borondipyrromethene (BODIPY) chromophore that is not pH activatable, shows such a
level of contrast to be inaccessible with a conventional signaling unit. Specifically,
incubation of MCF-7 cells with a mixture of **13** and **14** results in the internalization of
significant fractions of both. The two sets of fluorescent probes emit in distinct spectral
regions and can be imaged in separate detection channels. The resulting images (***a*** and ***b***

in Figure 3.8) indicate the ratio between the intracellular and extracellular fluorescence to be 3.6 for **14** and 11.9 for **13**. The 3-fold enhancement in contrast is a consequence of the activatable fluorescence of the latter, which turns on only in the acidic intracellular environment. Instead, the non-activatable emission of the former is significant also in the extracellular matrix and contributes plenty of background fluorescence. In fact, the overlap (*c* in Figure 3.8) of the two detection channels reveals the co-localization of the two sets of internalized fluorophores in addition to emission coming from the non-activatable species residing outside the cells.
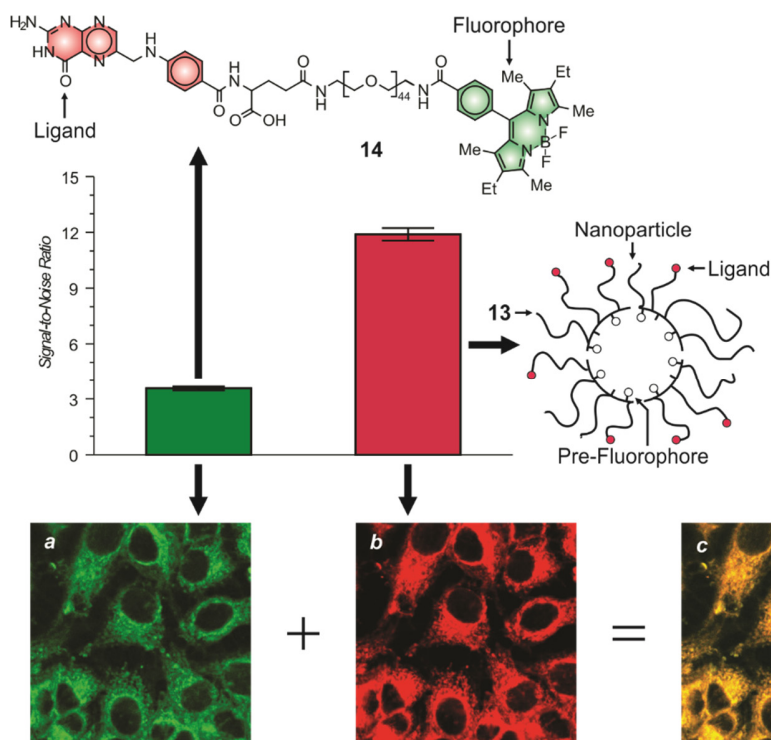
Figure 3.8 Ratios between the intracellular and extracellular emission intensities in fluorescence images (*a*, λ_{Ex} = 514 nm, λ_{Em} = 525–600 nm; *b*, λ_{Ex} = 561 nm, λ_{Em} = 575–750 nm; *c* is an overlap of *a* and *b*; scale bar = 25 μm) recorded after incubation of MCF-7 cells with a PBS solution of **13** and **14** for 2 hours.

3.3. Conclusions

A water-insoluble pre-fluorophore can be either encapsulated noncovalently within the hydrophobic interior of self-assembling nanocarriers of amphiphilic polymers or connected covalently to the poly(methacrylate) backbone of the macromolecular components and transferred into aqueous environments as a result. At neutral pH, the pre-fluorophore does not produce any detectable fluorescence. Under acidic conditions, its oxazine core opens to switch bathochromically the main absorption of an adjacent coumarin chromophore and activate intense fluorescence in the visible region of the electromagnetic spectrum. Indeed, the brightness ($\varepsilon \times \phi$) of these nanostructured constructs approaches $5 \times 10^5 \, \mathrm{M}^{-1} \, \mathrm{cm}^{-1}$ — a 170-fold enhancement relative to the constituent fluorophores dissolved individually in organic solvent. Such a dramatic increase is a result of the clustering of multiple chromophores within the same construct, which facilitates the absorption of exciting photons by raising ε, and the constrained environment around the fluorophores within the nanostructured assemblies, which increases ϕ by discouraging their nonradiative deactivation. Additionally, folate ligands can be attached covalently to the macromolecular components of these supramolecular assemblies without any detrimental effects on the photophysical properties of the fluorophores. Furthermore, these ligands direct the nanostructured assemblies into acidic intracellular compartments of folate-positive cells (MCF-7) and, when the pre-fluorophores are also covalently connected to the same macromolecular components, allow the pH-induced activation of fluorescence selectively in the intracellular environment of these particular cells. Instead, the relatively fast internalization and activation of the pre-fluorophores occurs, even in the absence of folate ligands, when these components are entrapped within the nanostructured constructs solely

on the basis of noncovalent interactions. In addition to allowing the selective detection of MCF-7 cells with high brightness, the covalent nanostructured constructs ensure also minimal background fluorescence from the extracellular matrix, because of the halochromic character designed into their emissive components. Specifically, their pH-activatable fluorescence translates into a 4-fold enhancement in contrast, relative to that accessible with a nonactivatable fluorophore–ligand model. Thus, the structural design of these supramolecular assemblies together with the halochromic character and photophysical properties engineered into their emissive components translate into nanoparticles with activatable and bright fluorescence for the selective detection of folate-positive cells and might ultimately evolve into unique cancer highlighters for diagnostic and surgical applications.

3.4. Experimental Procedures

Chemicals were purchased from commercial sources and used as received. MeCN was distilled over CaH$_2$. THF was distilled over Na and benzophenone. H$_2$O (18.2 MΩ-cm) was purified with a Barnstead International NANOpure DIamond Analytical system. Compounds **1**, **3**, **4**, **6**, **17**, **18** and **20** were prepared according to literature procedures[175, 227, 230, 235-237]. GPC was performed with a Phenomenex Phenogel 5-μm MXM column (7.8 × 300 mm) operated with a Nexera X2 system, in THF at a flow rate of 1.0 mL min^{-1} and a detection wavelength of 250 nm for **5**, **7** and **12** and 290 nm for **8** and **13**. Monodisperse polystyrene standards (3,700–250,000) were employed to determine the M_n and polydispersity index (PDI) of the polymers from the GPC traces, following a literature protocol[185]. NMR spectra were recorded with a Bruker Avance 400 spectrometer. DLS and SLS measurements were performed with a Malvern ZEN1600 apparatus. The values

reported for the hydrodynamic diameter are averaged over ten independent experiments of ten runs of 10 s each. The values reported for the average supramolecular weight were determined from the concentration dependence of the scattering intensity, following a literature protocol[185]. Absorption spectra were recorded with a Varian Cary 100 Bio spectrometer, using quartz cells with a path length of 1.0 cm. Emission spectra were recorded with a Varian Cary Eclipse spectrometer in aerated solutions. Fluorescence quantum yields were determined against a methanol solution of the acetate salt of cresyl violet ($\phi = 0.54$), following a literature protocol[238]. Fluorescence images were recorded with a Leica SP5 confocal laser-scanning microscope.
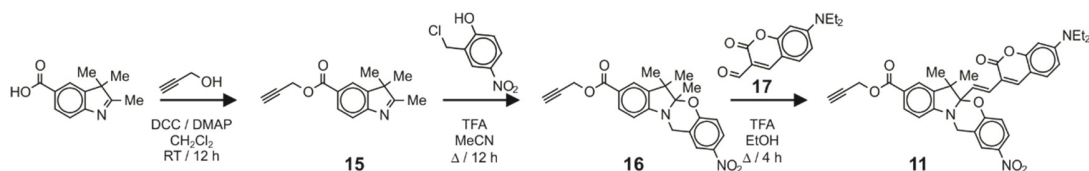
Figure 3.9 Synthesis of 11.

5. A solution of **3** (452 mg, 2 mmol), **4** (1.0 g, 0.5 mmol) and AIBN (0.5 mg, 0.003 mmol) in degassed THF (8 mL) was heated at 75 °C for 3 days in a sealed tube. After cooling down in an ice bath, the solvent was distilled off under reduced pressure. The residue was purified by column chromatography [SiO_2, $CHCl_3$/MeOH (40:1, v/v)] to give **5** (872 mg) as a white solid. GPC: $M_n = 21.0$ kDa, PDI = 1.16. ^{1}H NMR ($CDCl_3$): $\delta = 0.84$–0.93 (10H, br s), 1.22–1.39 (42H, br s), 1.69–1.77 (8H, br s), 3.37–3.41 (3H, s), 3.54–3.77 (176H, m), 3.87–4.02 (6H, br s), 4.06–4.16 (2H, br s).

7. A solution of **3** (904 mg, 4.0 mmol), **4** (2.0 g, 1.0 mmol), **6** (65 mg, 0.1 mmol) and AIBN (5 mg, 0.03 mmol) in degassed THF (20 mL) was heated at 75 °C for 3 days in a sealed tube. After cooling down to ambient temperature, the solvent was distilled off under reduced pressure. The residue was purified by column chromatography [SiO_2,

CH$_2$Cl$_2$/MeOH (20:1, v/v)] to give **7** (2.0 g) as a white solid. GPC: M_n = 16.7 kDa, PDI = 1.43; ^{1}H NMR (CDCl$_3$): δ = 0.84–0.93 (10H, br s), 1.22–1.39 (42H, br s), 1.69–1.77 (8H, br s), 2.25–2.32 (0.2H, m), 2.46–2.56 (0.2H, m), 3.37–3.41 (3H, s), 3.54–3.77 (180H, m), 3.87–4.02 (6H, br s), 4.06–4.16 (2H, br s).

8. A solution of **7** (146 mg, 0.06 mmol), folic acid (265 mg, 0.6 mmol), DCC (124 mg, 0.6 mmol) and DMAP (73 mg, 0.6 mmol) in DMSO (20 mL) was stirred at 40 °C for 3 days. The resulting precipitate was filtered off, dissolved in CH$_2$Cl$_2$ (150 mL) and washed with aqueous NaCl (1M, 6 × 100 mL). The solvent was distilled off under reduced pressure and the residue was purified by column chromatography [SiO$_2$, CH$_2$Cl$_2$/MeOH (10:1, v/v)] to afford **8** (42 mg) as a red solid. GPC: M_n = 19.2 kDa, PDI = 1.44; ^{1}H NMR (CDCl$_3$): δ = 0.84–0.93 (10H, br s), 1.22–1.39 (42H, br s), 1.69–1.77 (8H, br s), 3.37–3.41 (3H, s), 3.54–3.77 (176H, m), 3.87–4.02 (6H, br s), 4.06–4.16 (2H, br s).

9. A solution of 10-azidodecan-1-amine (990 mg, 5 mmol), methacrylic acid (516 mg, 6 mmol), DCC (1030 mg, 5 mmol) and DMAP (610 mg, 5 mmol) in CH$_2$Cl$_2$ (20 mL) was stirred at ambient temperature for 24 hours. The resulting precipitate was filtered off and the residue was purified by column chromatography [SiO$_2$, hexane/EtOAc (5:1, v/v)] to afford **9** (839 mg, 63%) as a colorless liquid. ESIMS: m/z = 267.1121 [M]+ (calcd. for C$_{14}$H$_{26}$N$_4$O = 266.3890); ^{1}H NMR (CDCl$_3$): δ = 1.27–1.14 (14H, m), 1.40–1.59 (4H, m), 1.88 (3H, s), 3.12–3.27 (2H, m), 5.21 (1H, s), 5.60 (1H, s), 6.18 (1H, br s).

10. A solution of **4** (904 mg, 4.0 mmol), **6** (65 mg, 0.1 mmol), **9** (2.0 g, 1.0 mmol) and AIBN (5 mg, 0.03 mmol) in degassed THF (20 mL) was heated at 75 °C for 3 days in a sealed tube. After cooling down to ambient temperature, the solvent was distilled off under reduced pressure. The residue was purified column chromatography (Sephadex LH-20,

MeOH) to give **10** (1.89 g) as a white solid. GPC: M_n = 17.2 kDa, PDI = 1.15; ^{1}H NMR (CDCl$_3$): δ = 0.95–1.08 (2H, br s), 1.21–1.42 (37H, br s), 1.89–2.09 (5H, br s), 2.23–2.30 (3H, br s), 3.23–3.30 (2H, br s), 3.38 (3H, s), 3.45–3.83 (176H, m), 3.87–4.01 (2H, br s), 4.03–4.20 (2H, br s).

11. A solution of **15** (204 mg, 0.5 mmol), **17** (147 mg, 0.6 mmol) and TFA (250 µL) in EtOH (20 mL) was heated under reflux for 4 hours. After cooling down to ambient temperature, the solvent was distilled off under reduced pressure and the residue was purified by column chromatography [SiO$_2$, hexane/EtOAc (3:1, v/v)] to afford **11** (241 mg, 76%) as a green solid. ESIMS: m/z = 634.2562 [M]$^+$ (calcd. for C$_{37}$H$_{35}$N$_3$O$_7$ = 633.7010); ^{1}H NMR (CDCl$_3$): δ = 0.87 (6H, t), 1.22 (6H, s), 2.03 (1H, s), 2.61–2.70 (2H, m), 3.43 (4H, q), 4.40 (2H, t), 4.66 (2H, d, 3 Hz), 6.49 (1H, s), 6.57–6.66 (3H, m), 6.88–6.99 (2H, m), 7.25 (1H, d, 8 Hz), 7.52 (1H, s), 7.82 (1H, s), 7.90 (1H, d, 8 Hz), 7.98–8.06 (2H, m).

12. CuI (4 mg, 0.02 mmol) was added to a solution of **10** (64 mg, 0.1 mmol) and **11** (1.0 g) in degassed MeCN. The mixture was stirred at ambient temperature for 12 hours under Ar. The solvent was distilled off under reduced pressure and the residue was purified by column chromatography (Sephadex LH-20, MeOH) to give **12** (890 mg) as a green solid. GPC: M_n = 17.8 kDa, PDI = 1.21; ^{1}H NMR (CDCl$_3$): δ = 1.03–1.17 (3H, br s), 1.22–1.47 (45H, br s), 2.05–2.52 (8H, br s), 3.21–3.33 (2H, br s), 3.40 (3H, s), 3.52–3.83 (190H, m), 3.85–3.99 (3H, br s), 4.03–4.20 (2H, br s).

13. A solution of **12** (400 mg), folic acid (22 mg, 0.5 mmol), DCC (10 mg, 0.05 mmol) and DMAP (6 mg, 0.05 mmol) in DMSO (2 mL) was stirred at 40 °C for 4 days in the dark. After cooling down to ambient temperature, the resulting precipitate was filtered off and the filtrate diluted in CH$_2$Cl$_2$ (50 mL) and washed with aqueous NaCl (1M, 3 × 50 mL).

The solvent was distilled off under reduced pressure and the residue was purified by column chromatography (Sephadex LH-20, MeOH) to give **13** (322 mg) as a green solid. GPC: M_n = 18.9 kDa, PDI = 1.45; ^{1}H NMR (CDCl$_3$): δ = 1.02–1.18 (3H, br s), 1.21–1.48 (46H, br s), 2.01–2.55 (8H, br s), 3.23–3.30 (2H, br s), 3.38 (3H, s), 3.50–3.83 (180H, m), 3.87–4.01 (3H, br s), 4.03–4.20 (2H, br s).

14. A solution of DCC (103 mg, 0.5 mmol), folic acid (220 mg, 0.5 mmol), **19** (120 mg, 0.05 mmol) and DMAP (61 mg, 0.5 mmol) in DMSO (20 mL) was stirred at 40 °C for 3 days. The resulting precipitate was filtered off and the mixture was dissolved in CH$_2$Cl$_2$ (150 mL) and washed with aqueous NaCl (1M, 6 × 100 mL). The solvent was distilled off under reduced pressure and the residue was purified by column chromatography [SiO$_2$, CH$_2$Cl$_2$/MeOH (10:1, v/v)] to afford **14** (24 mg, 17%) as a red solid. ^{1}H NMR [(CD$_3$)$_2$SO]: δ = 1.13 (6H, t, 8 Hz), 1.27 (6H, s), 2.29 (4H, m), 2.44 (4H, q, 8 Hz), 2.56 (6H, s), 3.27–3.48 (176H, m), 4.33 (1H, br), 4.46 (2H, br), 6.63 (2H, br), 6.91 (1H, br), 7.58 (2H, d, 8 Hz), 7.78 (1H, s), 8.09 (2H, d, 6 Hz), 8.64 (1H, s).

15. A solution of 2,3,3-trimethyl-5-carboxy-3*H*-indole (1015 mg, 5 mmol), propargyl alcohol (420 mg, 6 mmol), DCC (1030 mg, 5 mmol) and DMAP (610 mg, 5 mmol) in CH$_2$Cl$_2$ (20 mL) was stirred at ambient temperature for 12 hours. The resulting precipitate was filtered off and the residue was purified by column chromatography [SiO$_2$, hexane/EtOAc (3:1, v/v)] to afford **15** (800 mg, 62%) as a white solid. ESIMS: *m/z* = 256.1347 [M]$^+$ (calcd. for C$_{16}$H$_{17}$NO$_2$ = 255.3170); ^{1}H NMR (CDCl$_3$): δ = 1.32 (6H, s), 2.01 (1H, t, 3 Hz), 2.28 (3H, s), 2.53–2.58 (2H, m), 4.37 (2H, t, 9 Hz), 7.48 (1H, d, 8 Hz), 7.90 (1H, s), 7.99 (1H, d, 8 Hz).

16. A solution of **15** (400 mg, 1.6 mmol) and 2-chloromethyl-4-nitrophenol (375 mg, 2 mmol) in MeCN (30 mL) was heated under reflux for 12 hours. After cooling down to ambient temperature, the solvent was distilled off under reduced pressure and the residue was purified by column chromatography [SiO_2: hexane/EtOAc (4:1, v/v)] to afford **16** (204 mg, 32%) as a yellow solid. ESIMS: m/z = 407.1603 $[M]^+$ (calcd. for $C_{23}H_{22}N_2O_5$ = 406.4380); ^{1}H NMR (CDCl$_3$): δ = 1.19 (3H, s), 1.58 (6H, d, 8 Hz), 2.01 (1H, t, 3 Hz), 2.60–2.65 (2H, m), 4.37 (2H, t, 7 Hz), 4.67 (2H, d, 4 Hz), 6.60 (1H, d, 9 Hz), 6.73 (1H, d, 9 Hz), 7.79 (1H, d, 2 Hz), 7.87 (1H, dd, 2 and 2 Hz), 7.96 (1H, dd, 3 and 3 Hz), 8.01 (1H, d, 3 Hz).

19. A solution of DCC (41 mg, 0.2 mmol) in CH_2Cl_2 (5 mL) was added dropwise over 10 min to a solution of **18** (42 mg, 0.1 mmol), poly(ethylene glycol) bis(amine) (M_n = 2.0 kDa, 400 mg, 0.2 mmol) and DMAP (25 mg, 0.2 mmol) in CH_2Cl_2 (15 mL) maintained at 0 °C. The reaction was allowed to warm up to ambient temperature and then stirred for 12 hours under these conditions. The resulting precipitate was filtered off and the solvent of the filtrate was distilled off under reduced pressure. The residue was purified by column chromatography [SiO_2, CH_2Cl_2/MeOH (10:1, v/v)] to afford **19** (140 mg, 63%) as a red solid. ^{1}H NMR (CDCl$_3$): δ = 1.03 (6H, t, 8 Hz), 1.31 (6H, s), 2.35 (4H, q, 8 Hz), 2.57 (6H, s), 3.78–3.62 (176H, m), 7.38 (2H, d, 8 Hz), 8.00 (2H, d, 8 Hz).
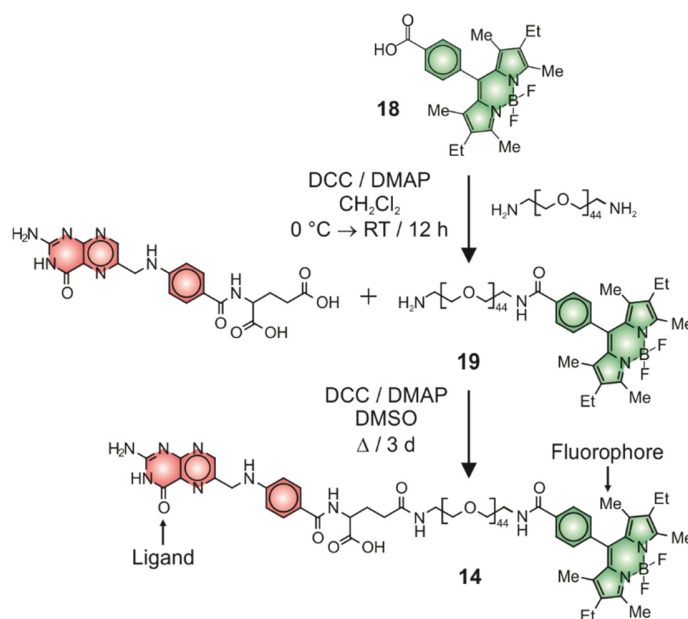
Figure 3.10 Synthesis of 14.

Doped Polymer Nanoparticles for Spectroscopy. CH_2Cl_2 solutions of **1** (0.2 mM, 50 µL)
and either **5** or **8** (2.5 mg mL^{-1}, 200 µL) were mixed and the solvent was distilled off under
reduced pressure. The residue was dispersed in phosphate buffer (1.0 mL) with pH ranging
from 3.0 to 10.0. The resulting dispersions were sonicated for 5 min, stored for 10 min at
ambient temperature and used for the spectroscopic experiments without further
purification. The concentration of **1** in the final solutions was estimated from the
absorbance for the coumarin chromophore and the ε measured in acetonitrile, which is 17.6
mM^{-1} cm^{-1}. The concentration of the nanoparticles was determined from the mass of **5**
and **8** and the corresponding average supramolecular weight, which is 588 and 435 kDa
respectively according to SLS measurements. The ratio between the concentrations of
molecular guest and supramolecular host is 23 in both instances. This value is the average
number of pre-fluorophores per nanosized container.

Doped Polymer Nanoparticles for Imaging. CH_2Cl_2 solutions of **1** (0.5 mM, 40 μL) and either **5** or **8** (10 mg mL^{-1}, 100 μL) were mixed and the solvent was evaporated under reduced pressure. The residue was dispersed in Dulbecco's PBS (400 μL). The resulting dispersions were sonicated for 5 min, stored for 10 min at ambient temperature and passed through a syringe filter with a pore size of 200 nm. The filtrate was used for the imaging experiments without further purification.

Cell Culture. HEK-293 cells were cultured in Dulbecco's modified Eagle's media supplemented with fetal bovine serum (10% v/v), penicillin (100 U mL^{-1}) and streptomycin (0.01% v/v). MCF-7 cells were cultured in Roswell Park Memorial Institute medium supplemented with fetal bovine serum (10% v/v), penicillin (100 U mL^{-1}) and streptomycin (0.01% v/v). Cells were maintained in a humidified CO_2 (5% v/v) atmosphere at 37 °C, seeded in 96-well glass-bottom plates at a density of 10^5 cells cm^{-2} and incubated overnight. The culture medium was switched to L-15 and then a PBS solution (10 μL) of *(i)* nanoparticles of **5** containing **1**, *(ii)* nanoparticles of **8** containing **1**, *(iii)* **12** (5.0 mg mL^{-1}), *(iv)* **13** (5.0 mg mL^{-1}) or *(v)* a mixture of **13** (5.0 mg mL^{-1}) and **14** (0.2 mM) was added to the cells (20 μL). For the inhibition experiments, a PBS solution of folic acid (0.02–0.50 M) was added to the cells and, after 0.5 hours, a PBS solution of **13** (5.0 mg mL^{-1}) was also added to the sample. All cells were incubated at 25 °C for 2–24 hours and imaged without any washing.
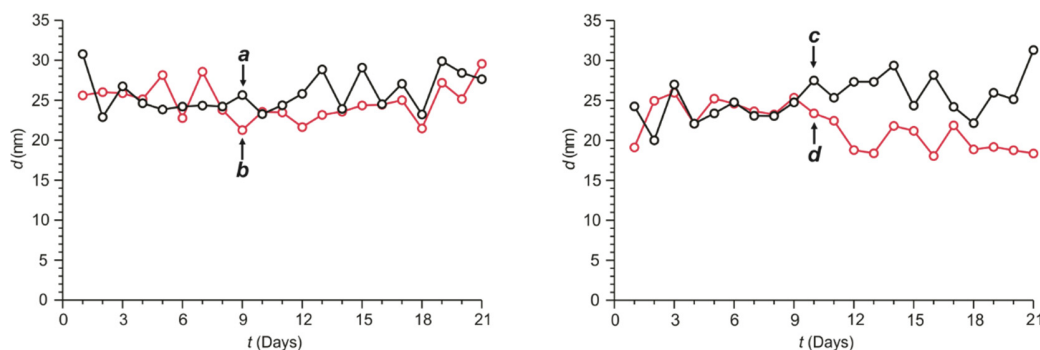
Figure 3.11 Temporal evolutions of the average hydrodynamic dynamic diameter of **5** (*a*), **8** (*b*), **12** (*c*) and **13** (*d*) in buffer at a pH of 7.15.
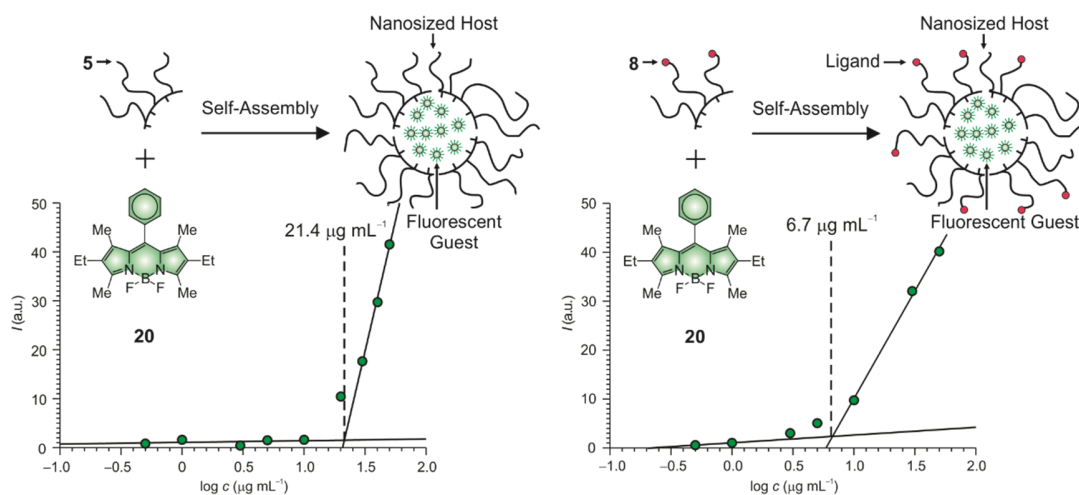
Figure 3.12 Plots of the emission intensity (λ_{Ex} = 500 nm, λ_{Em} = 540 nm), recorded at 25 °C after combining CH$_2$Cl$_2$ solutions of **20** (0.1 mM, 10 µL) and either **5** or **8** (50 µg mL^{-1}, 20–100 µl or 500 µg mL^{-1}, 100–1000 µL), distilling the solvent off under reduced pressure, dispersing the residue in buffer (1.0 mL) with pH of 7.15 and passing the resulting dispersion through a nanoporous membrane (200 nm), against the polymer concentration.

Figure 3.13 Plots of the emission intensity (λ_{Ex} = 500 nm, λ_{Em} = 540 nm), recorded at 25 °C after combining CH$_2$Cl$_2$ solutions of **20** (0.1 mM, 10 µL) and either **12** or **13** (50 µg mL^{-1}, 20–100 µl or 500 µg mL^{-1}, 100–1000 µL), distilling the solvent off under reduced pressure, dispersing the residue in buffer (1.0 mL) with pH of 7.15 and passing the resulting dispersion through a nanoporous membrane (200 nm), against the polymer concentration.

Figure 3.14 Normalized absorption and emission (λ_{Ex} = 560 nm) spectra of **1** (10 µM), before (**a**) and after (**b** and **c**) the addition of CF$_3$CO$_2$H (1 eq.) in MeCN, of **1** and **5** in buffer with pH of 7.15 (**d**) or 4.01 (**e** and **f**), of **11** (10 µM), before (**g**) and after (**h** and **i**) the addition of CF$_3$CO$_2$H (10 eq.) in MeCN, and of **12** (500 µg mL^{-1}) in buffer at a pH of 6.88 (**j**) or 3.02 (**k** and **l**).
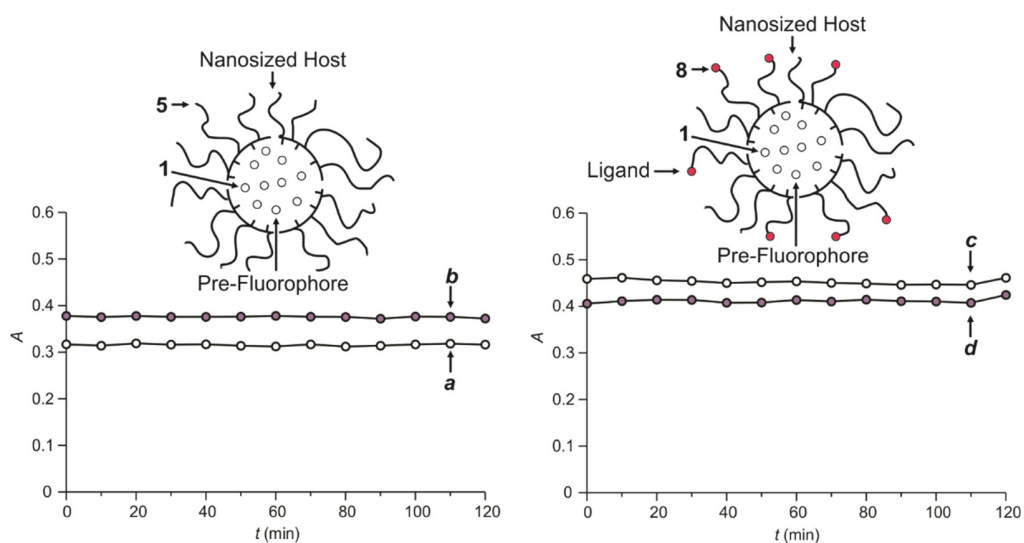
Figure 3.15 Temporal evolution of the absorbance detected at 414 (*a* and *c*) and 596 nm (*b* and *d*) for either **1** and **5** or **1** and **8** in buffer with pH of either 7.15 (*a* and *c*) or 4.01 (*b* and *d*).
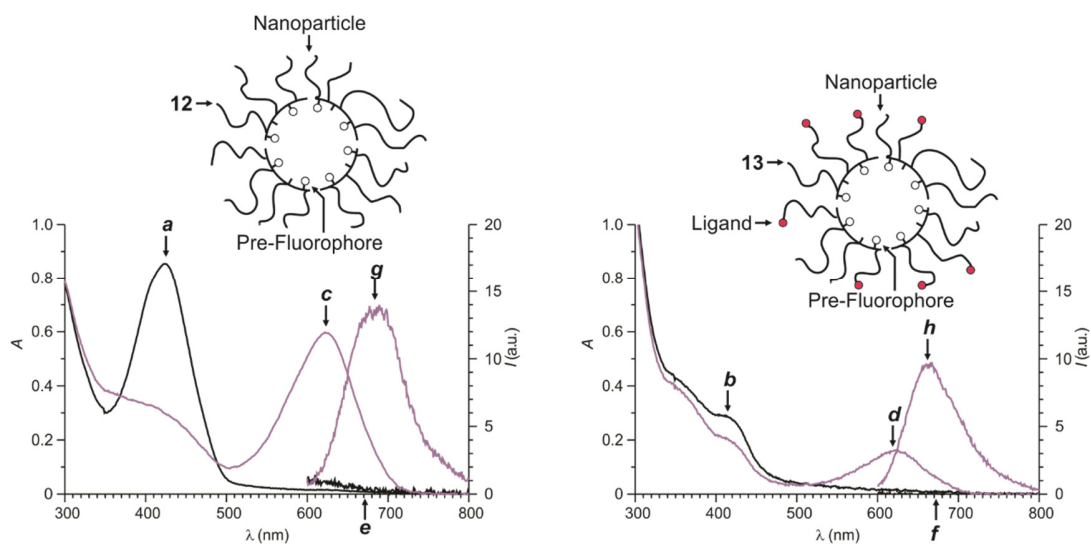
Figure 3.16 Absorption and emission (λ_{Ex} = 560 nm) spectra of **12** in buffer at a pH of 6.88 (*a* and *e*) or 3.02 (*c* and *g*) and of **13** in buffer at a pH of 6.88 (*b* and *f*) or 3.02 (*d* and *h*).
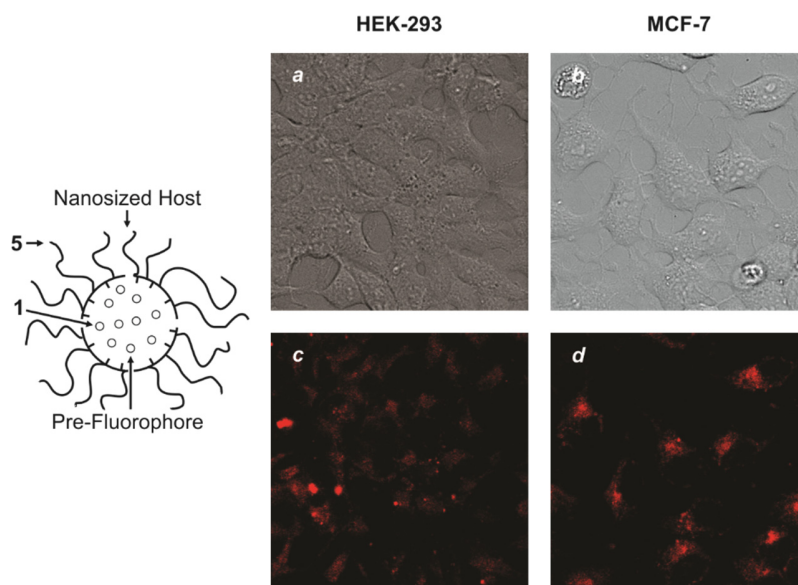
Figure 3.17 Transmittance (*a* and *c*) and fluorescence (*b* and *d*) images (λ_{Ex} = 561 nm, λ_{Em} = 575–750 nm, scale bar = 25 µm) recorded after incubation of HEK-293 and MCF-7 cells with PBS solutions of **1** and **5** for 1 hour.
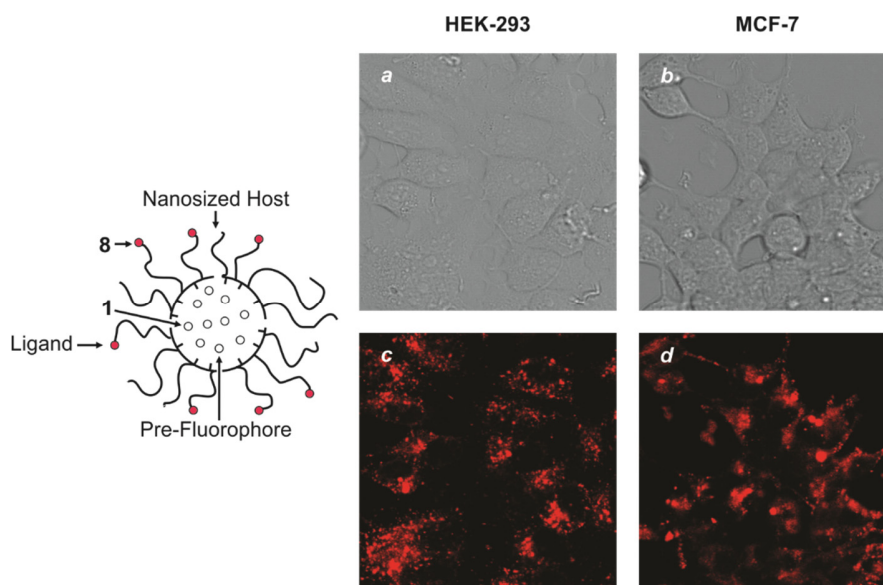
Figure 3.18 Transmittance (*a* and *c*) and fluorescence (*b* and *d*) images (λ_{Ex} = 561 nm, λ_{Em} = 575–750 nm, scale bar = 25 µm) recorded after incubation of HEK-293 and MCF-7 cells with PBS solutions of **1** and **8** for 1 hour.
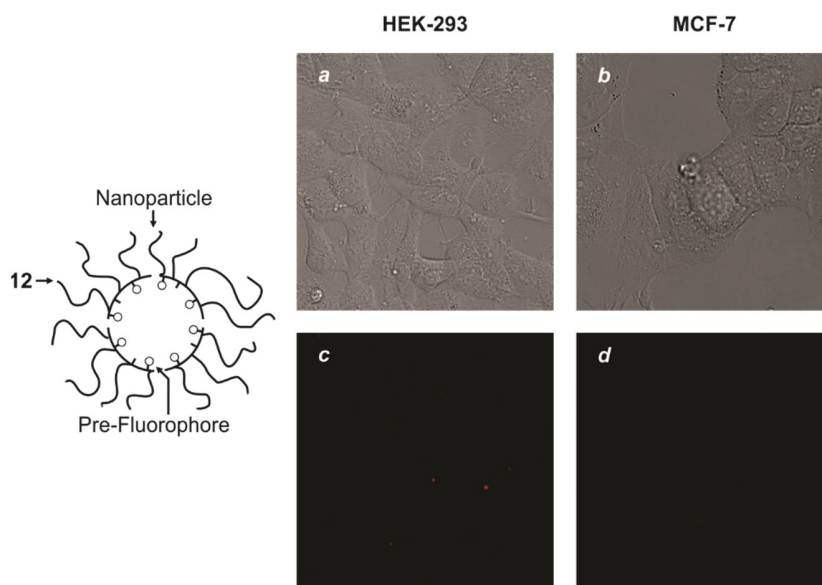
Figure 3.19 Transmittance (*a* and *c*) and fluorescence (*b* and *d*) images (λ_{Ex} = 561 nm, λ_{Em} = 575–750 nm, scale bar = 25 µm) recorded after incubation of HEK-293 and MCF-7 cells with PBS solutions of **12** for 2 hours.
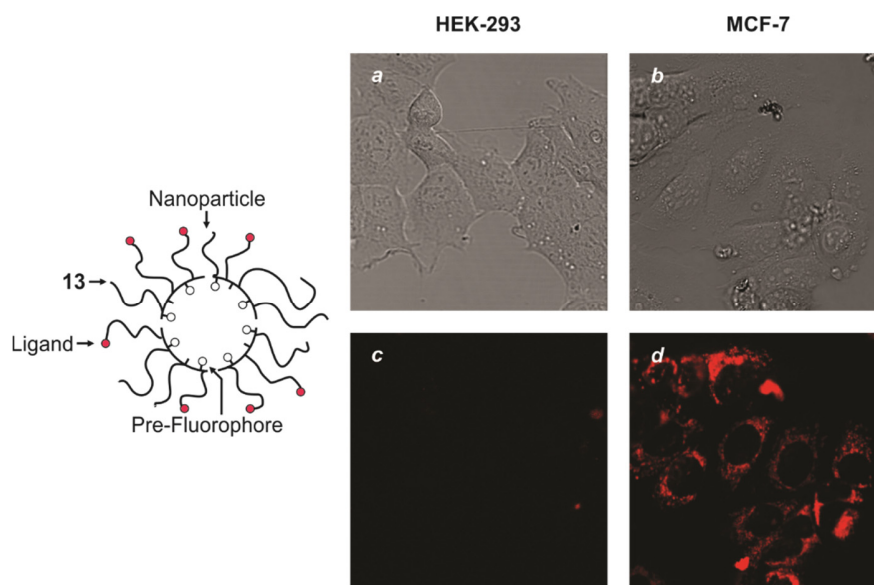
Figure 3.20 Transmittance (*a* and *c*) and fluorescence (*b* and *d*) images (λ_{Ex} = 561 nm, λ_{Em} = 575–750 nm, scale bar = 25 µm) recorded after incubation of HEK-293 and MCF-7 cells with PBS solutions of **13** for 2 hours.
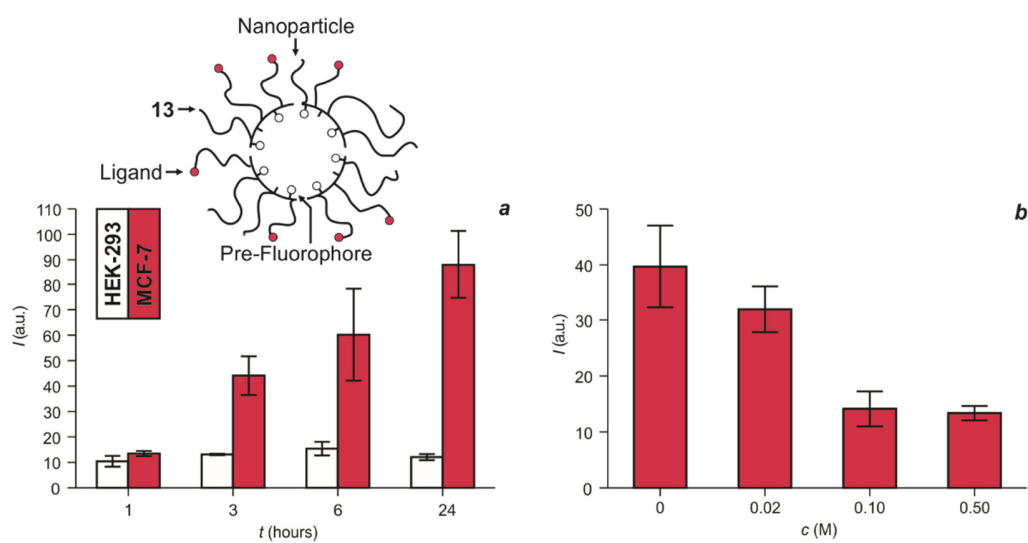
Figure 3.21 Average intracellular emission intensities (λ_{Ex} = 561 nm, λ_{Em} = 575–750 nm) recorded after incubation of (***a***) HEK-293 and MCF-7 cells with PBS solutions of **13** for the time indicated on the horizontal axis or (***b***) MCF-7 cells with first a PBS solution of folic acid, at the concentration indicated on the horizontal axis, for 0.5 hours and then a PBS solution of **13** for 2 hours.

CHAPTER 4 Photochemical Barcodes

4.1. Background

The vast majority of experimental studies in chemical research requires the manipulation of collections of identical species, ranging from small molecules to large particles, diffusing in fluids and base their conclusions on the average behavior of such a multitude of components. Most synthetic protocols, for example, rely on the combination of multiple copies of complementary reactants in solution to allow their chemical reaction and the generation of multiple copies of a target product[239]. However, they cannot provide any information on the fate of the individual components of the reacting mixture to establish which reactant molecule is converted into which product molecule. The overwhelming challenge in monitoring the evolution of specific individuals out of a large population of identical species extends also to the biological world. The processes responsible for embryogenesis, for example, demand multiple copies of identical cells to migrate in the interior of a developing embryo and assemble into diverse tissues and, eventually, generate distinct organs[240]. Tracking the progression of individual cells in the course of such an intricacy of processes with spatiotemporal precision to establish where a given cell ultimately localizes in a certain organ is a daunting task. Similar analogies can be extended from developmental to behavioral biology, which often requires the need to monitor the behavior of selected individuals out of a large population of animals for prolonged periods of time[241]. The development of a general tool to mark chosen members of collections of identical species, ranging from tiny molecules to developed organisms, with recognizable labels and allow their spatiotemporal tracking without imposing any significant perturbation on their behavior would, therefore, be of utmost significance in a diversity of

disciplines across the biological and chemical sciences. On the basis of these considerations, our laboratories designed a photochemical strategy to encode optical barcodes[242-245], in the form of unique combinations of multiple fluorescence signals, within selected members of a given population of components with microscaled precision. Our innovative method relies on the photochemical and photophysical properties of photoactivatable fluorophores[214, 246-250] to write optical codes with spatial control and then track the marked species in time with the sequential acquisition of fluorescence images. This article reports the experimental implementation of these unprecedented operating principles and demonstrates their ability to permit the differentiation of multiple species and their simultaneous monitoring for prolonged periods of time *in vivo* with a representative example.

4.2. Results and Discussion

Our laboratories recently developed a mechanism for fluorescence activation based on the unique photochemical behavior of 2*H*,4*H*-[1,3]oxazine heterocycles[251] and outstanding photophysical properties of BODIPY chromophores[32, 40, 252-254]. These studies ultimately identified a viable structural design to shift bathochromically the main absorption of a BODIPY chromophore with the photoinduced cleavage of an oxazine ring[171, 255-256]. The resulting spectral shift can be exploited to excite selectively the photochemical product and allow the activation of its fluorescence with ultrahigh contrast levels that would be, otherwise, impossible to achieve with conventional mechanisms based on the photoinduced suppression of quenching pathways[257-260]. This behavior suggested the design of a compound (**1** in Figure 4.1) capable of undergoing two consecutive photochemical reactions. It incorporates a BODIPY fluorophore and two photocleavable oxazines within

the same covalent skeleton and can be synthesized in two steps from commercial and known precursors (Figure 4.7). Upon illumination at an activation wavelength (λ_{Ac}) within the spectral region where the 2-nitrobenzyl chromophores absorb, the two oxazine heterocycles cleave sequentially to convert **1** into **2** first and then **2** into **3** with the release of two equivalents of **4** (Figure 4.1). Consistently, high-performance liquid chromatography (HPLC) traces show the gradual decrease of a peak for **1** with the concomitant increase of peaks for **2** and **3** during the photolytic transformation (Figure 4.8). Analysis of the dependence of the relative peak intensities on the irradiation time indicates the quantum yields (Table 4.1) for the two consecutive photochemical reactions to be 0.005 and 0.001 respectively.
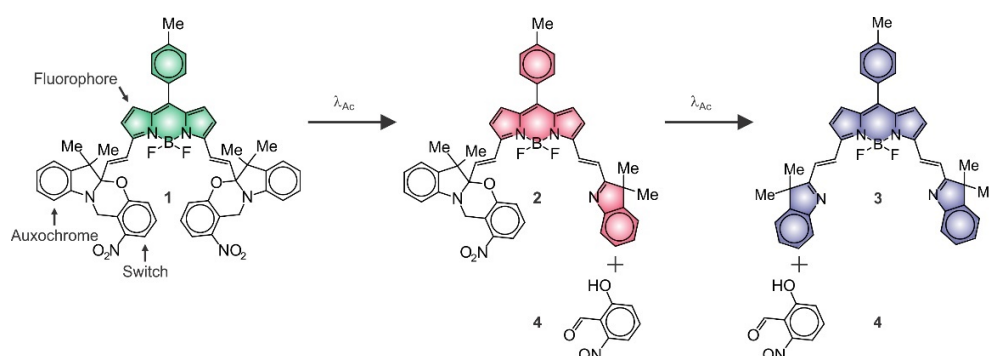
Figure 4.1 Photoinduced transformation of 1 into 2, 3 and 4.

The absorption and emission spectra (*a* and *d* in Figure 4.2) of **1** show bands with maxima at wavelengths (Table 4.1) of 574 and 600 nm respectively. The photoinduced disconnection of one of the two 2-nitrobenzyl switches changes the hybridization of the carbon atom in position 2 of the 2*H*,3*H*-indole heterocycle from sp^3 in **1** to sp^2 in **2**. This structural transformation brings the BODIPY chromophore in electronic conjugation with the adjacent indole auxochrome and shifts bathochromically the absorption and emission bands (*b* and *e* in Figure 4.2) to 619 and 628 nm respectively. The subsequent

photoinduced cleavage of the other oxazine heterocycle converts **2** into **3** and extends the electronic conjugation of the BODIPY chromophore over yet another indole auxochrome. As a result, the absorption and emission bands (*c* and *f* in Figure 2) shift even further to 663 and 673 nm respectively.
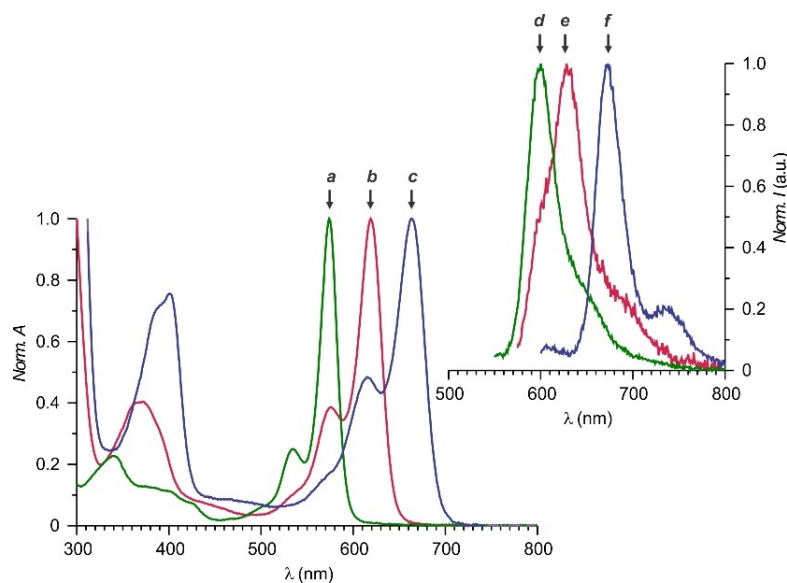
Figure 4.2 Normalized absorption (*a*–*c*) and emission (*d*–*f*) spectra of **1** (*a* and *d*, λ_{Ex} = 540 nm), **2** (*b* and *e*, λ_{Ex} = 565 nm) and **3** (*c* and *f*, λ_{Ex} = 590 nm) in MeCN at 25 °C.

The pronounced spectral shifts associated with the transformation of **1** into **2** and **3** provide the opportunity to monitor the gradual conversion of these species with the sequential acquisition of absorption and emission spectra (Figure 4.9) in acetonitrile solution during the photolytic transformation. Similarly, the course of the two consecutive photochemical reactions can be probed with the sequential acquisition of fluorescence images of either poly(methyl methacrylate) (PMMA) films (Figure 4.10) or polystyrene (PS) beads (Figure 4.11) doped with these photoswitchable compounds. In both instances, any given region of interest within the sample can be irradiated at a λ_{Ac} of 405 nm to induce the two sequential photochemical transformations. Concomitantly, the resolved emissions of **1**, **2** and **3** can be recorded in three separate detection channels of the same fluorescence

microscope. On the basis of this experimental protocol, the relative amounts of three interconverting species, and hence the emission intensities detected in the three channels, can be regulated in any illuminated area simply by controlling the irradiation time. For example, PS beads with an average diameter of 3.0 μm can be doped with **1** (5% w/w), deposited on a glass slide and imaged in transmittance mode (*a* in **Figure 4.3**). Different regions of the sample can be illuminated individually at λ_{Ac} with identical power, but for four distinct times. Then, fluorescence images of the activated sample can be recorded in three detection channels and overlapped in a single frame (*b* of **Figure 4.3**). The emission in one channel (green) can be collected between 575 and 600 nm, upon illumination at an excitation wavelength (λ_{Ex}) of 561 nm, to detect predominantly the fluorescence of **1**. The emission in the other two channels (red and blue) can instead be recorded at 645–660 and 750–800 nm respectively with a λ_{Ex} of 633 nm in both instances to detect predominantly the fluorescence of **2** and **3** respectively. A plot (*c* in **Figure 4.3**) of the resulting red and blue emission intensities, reported relative to the green, clearly reveals that pristine (1 in *b* of **Figure 4.3**) and activated beads (2–5 in *b* of **Figure 4.3**) can clearly be distinguished. Specifically, each one of these five beads has a unique combination (barcode) of emission values that allows their differentiation. Thus, individual members of a relatively large population of identical beads can be marked photochemically with distinct barcodes to permit the identification of these, otherwise undistinguishable, objects.
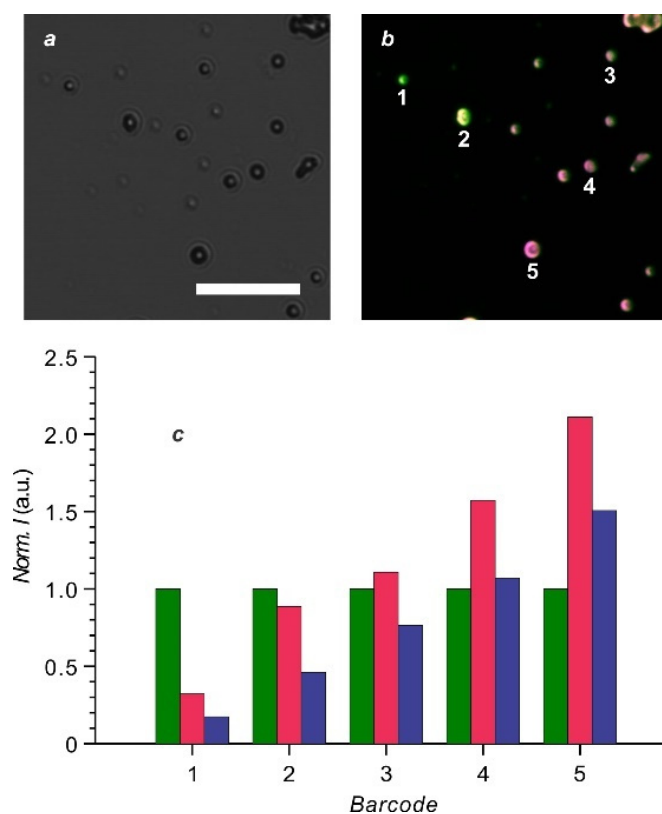
Figure 4.3 Transmittance image (*a*, scale bar = 15 µm) and overlap of three fluorescence images (*b*) of PS beads, doped with **1** (5% w/w), recorded with a λ_{Ex} of 561 nm and a detection window of 575–600 nm (*b*–*e*), a λ_{Ex} of 633 nm and a detection window of 645–660 nm or a λ_{Ex} of 633 nm and a detection window of 750–800 nm after illumination of individual beads at a λ_{Ac} of 405 nm (50 mW cm^{-2}) for 0 (Bead 1), 2 (Bead 2), 3 (Bead 3), 5 (Bead 4) or 20 min (Bead 5) together with the relative emission intensities (*c*) of the five beads.

The mild visible illumination conditions sufficient to induce the transformation of **1** into **2** and **3** suggest that it should be possible to write barcodes within living organisms with no toxic effects. In order to test this possibility, the nematode *Caenorhabditis elegans* was incubated with an aqueous dispersion of PS beads, doped with **1**, to allow the uptake of the fluorescent particles *via* pharyngeal pumping into the intestine. Sequential fluorescence images reveal bead accumulation in the gut lumen, consistently with a previous study[261]. Treatment of the labeled worms with muscimol, a GABA-A receptor agonist[262], paralyzes the organism[263] sufficiently to allow stable illumination and photoconversion of particles

within distinct regions of the gut lumen. Indeed, overlaps of fluorescence images, collected in the three detection channels before and after (*a* and *b* in Figure 4) irradiation exclusively within the posterior intestine, clearly demonstrate that the photochemical transformation is restricted to the illuminated region. Magnifications of the activated area, recorded before (*c* in Figure 4.4) and after illumination for 5, 10 and 20 min (*d–f* in Figure 4.4), together with the corresponding barcodes (*g* in Figure 4.4) confirm the gradual conversion of **1** into **2** and **3**.
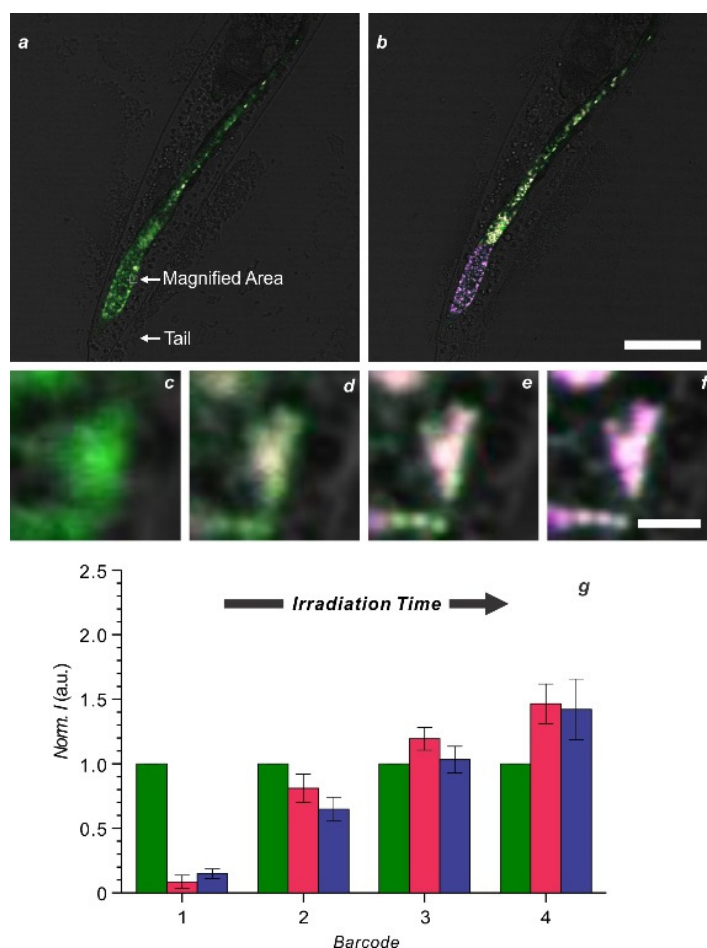
Figure 4.4 Overlaps of brightfield transmittance and three fluorescence images (scale bar = 100 μm) of a *Caenorhabditis elegans* worm labeled with PS beads, doped with **1** (5% w/w), recorded with a λ_{Ex} of 561 nm and a detection window of 575–600 nm, a λ_{Ex} of 633 nm and a detection window of 645–660 nm or a λ_{Ex} of 633 nm and a detection window of 750–800 nm before (*a*) and after (*b*) illumination of the nematode tail at a λ_{Ac} of 405 nm (50 mW cm^{-2}) for 30 min and magnifications (scale bar = 3 μm) of the tail acquired before

(*c*) and after illumination for 5 (*d*), 10 (*e*) and 20 min (*f*) together with the corresponding relative emission intensities (*g*).
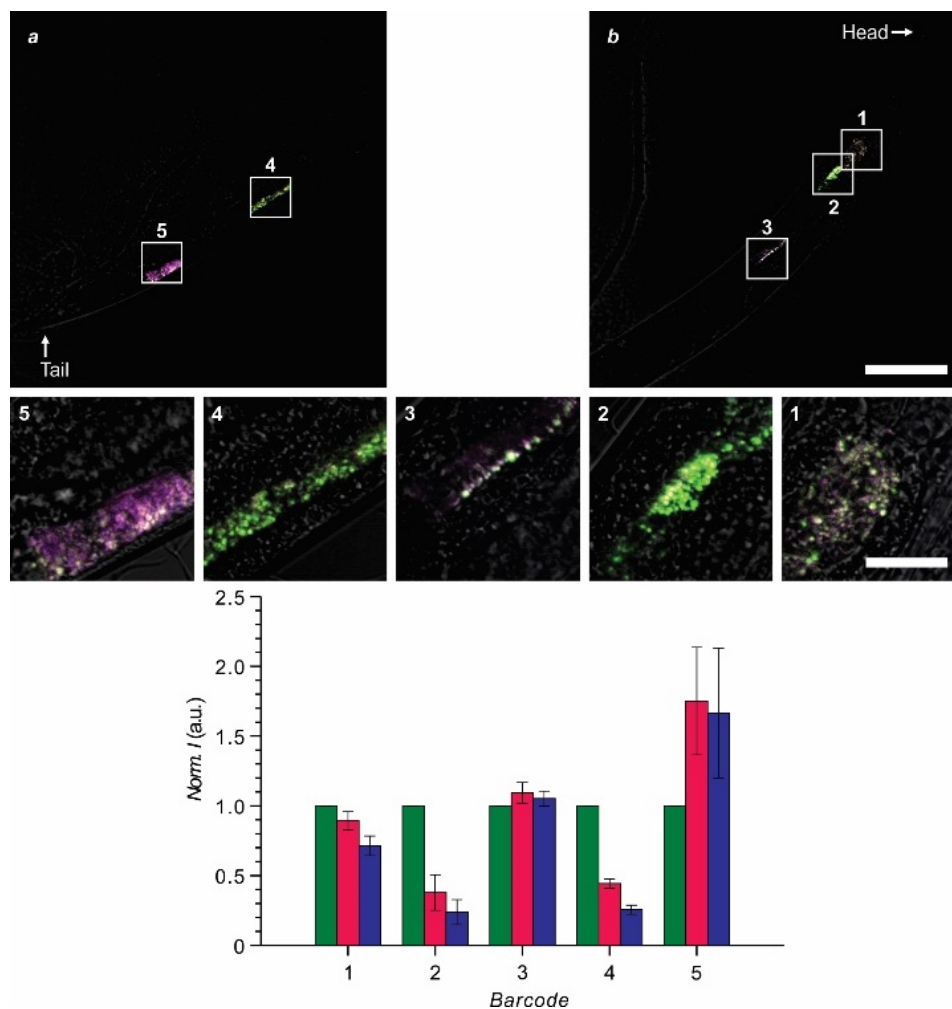
Figure 4.5 Overlap of brightfield transmittance and fluorescence images (*a* and *b*, scale bar = 100 μm) of a *Caenorhabditis elegans* labeled with PS beads, doped with **1** (5% w/w), recorded with a λ_{Ex} of 561 nm and a detection window of 575–600 nm, a λ_{Ex} of 633 nm and a detection window of 645–660 nm or a λ_{Ex} of 633 nm and a detection window of 750–800 nm after illumination of individual regions within the nematode at a λ_{Ac} of 405 nm (50 mW cm^{-2}) for 5 (Area 1), 0 (Area 2), 10 (Area 3), 0 (Area 4) and 20 min (Area 5) together with the corresponding magnifications (scale bar = 20 μm) and relative emission intensities.

The very same experimental protocol can be exploited to write distinct barcodes in different regions of the same animal and then monitor their temporal evolution. Once again, images (Figure 4.12) of a nematode incubated with the doped PS beads and treated with muscimol

show fluorescence in the animal interior. Illumination of three regions of the labeled organism at λ_{Ac} with the same power, but for different times, produces distinct relative amounts of **1**, **2** and **3**. Comparison of the corresponding images (1, 3 and 5 in Figure 4.5) to those (2 and 4 in Figure 4.5) of areas that were not activated clearly confirms the photochemical conversion. Indeed, each one of the activated area (1, 3 and 5) has a unique barcode (Figure 4.5) that differs from those of the pristine areas (2 and 4) of the animal. Over the course of a few hours, the effects of muscimol fade and the paralyzed nematode gradually resumes its normal activity. Sequential fluorescence images, collected during this period of time, clearly demonstrate that the animal survives the bead uptake as well as the irradiation conditions required to induce the photochemical transformations. Furthermore, the barcodes imprinted in the nematode remain unchanged to allow the tracking of the labeled areas in time. For example, four images collected consecutively over 77 s show the translocation of one barcoded region (2 in Figure 4.6) along the intestinal tract of the animal. The pharyngeal pump pushes this particular area from the head to the tail of the animal and then back, while the other two barcoded regions (1 and 3 in Figure 4.6) maintain their original position. During these dynamic processes, the relative emission intensities of the three channels in each labeled region remain approximately constant and the barcodes detected in the initial and final frames are essentially identical (Figure 4.6).
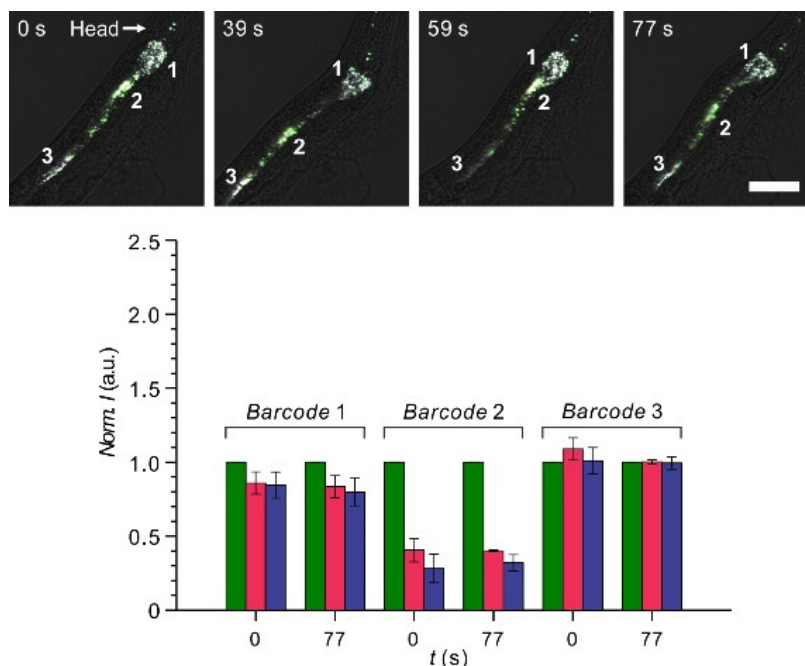
Figure 4.6 Overlaps of brightfield transmittance and fluorescence images (scale bar = 50 μm) of a *Caenorhabditis elegans* labeled with PS beads, doped with **1** (5% w/w), recorded sequentially over the course of 77 s with a λ_{Ex} of 561 nm and a detection window of 575–600 nm, a λ_{Ex} of 633 nm and a detection window of 645–660 nm or a λ_{Ex} of 633 nm and a detection window of 750–800 nm after illumination of individual regions within the nematode at a λ_{Ac} of 405 nm (50 mW cm^{-2}) for 5 (Area 1), 0 (Area 2) and 10 min (Area 3) together with the relative emission intensities measured for each area in the initial and final frames.

Our results demonstrate that the consecutive disconnection of two photocleavable oxazines from the same BODIPY chromophore, under the influence of mild visible illumination, can be exploited to generate mixtures of three fluorophores with resolved emissions inside polymer beads. The illumination conditions can be adjusted to regulate precisely the relative amounts of the three-emissive species to imprint barcodes, each consisting of three fluorescence signals, within individual beads. On the basis of this protocol, selected members of relatively large populations of, otherwise identical, beads can be marked with unique and detectable codes to allow their individual tracking in time. Furthermore, the visible wavelengths and moderate intensities, sufficient to induce these photochemical transformations, permit the photochemical imprinting of barcodes also in living nematodes.

Different regions of the very same animal, labeled with the photoswitchable beads, can be marked with distinct barcodes and their dynamics tracked for prolonged periods of time. Thus, our operating principles for photochemical barcoding can evolve into a general strategy for the imprinting of multiple, but distinguishable, labels *in vivo* with unprecedented spatial and temporal control.

4.3. Experimental Procedures

Chemicals were purchased from commercial sources and used as received. CH_2Cl_2 and MeCN were distilled over CaH_2. H_2O (18.2 MΩ cm) was purified with a Barnstead International NANOpure DIamond Analytical system. Compounds **5–7** were prepared following literature protocols[171, 264]. Electrospray ionization mass spectrometry (EISMS) was performed with a Bruker micrOTO-Q II spectrometer. NMR spectra were recorded with a Bruker Avance 400 spectrometer. Doped polymer nanoparticles were prepared by combining CH_2Cl_2 solutions of **1** (0.1 mg mL^{-1}, 50 μL) and **7** (2.5 mg mL^{-1}, 200 μL) and heating the resulting mixture at 40 °C in an open vial. After the evaporation of the solvent, the residue was purged with air, dispersed in PBS (1 mL), sonicated for 5 min and flashed through a syringe filter with a pore size of 0.2 μm. The filtrate was used for the imaging and spectroscopic measurements without further purification. Absorption spectra were recorded with a Varian Cary 100 Bio spectrometer in quartz cells with a path length of 1.0 cm. Emission spectra were recorded with a Varian Cary Eclipse spectrometer in aerated solutions. Fluorescence quantum yields were determined against EtOH solutions of either the acetate salt of Cresyl Violet ($\phi_F = 0.54$) or the perchlorate salt of Oxazine 1 ($\phi_F = 0.15$), following a literature protocol[238]. Photolyses were performed in aerated solutions with a Luzchem Research LZC-4V photoreactor, operating at 350 nm (4.2 mW cm^{-2}), and the

corresponding quantum yields were determined with a potassium ferrioxalate actinometer, according to an established procedure[265]. HPLC was performed with an Agilent Microsorb 100-5 BDS column (4.6 × 250 mm) operated with a Shimadzu Nexera X2 system in MeCN/H$_2$O (9:1, v/v) at a flow rate of 1.0 mL min^{-1} and detection wavelength of 275 nm. Doped polymer films were prepared by spin coating CH$_2$Cl$_2$ solutions of PMMA (120 kDa, 20 mg mL^{-1}) and **1** (50 μg mL^{-1}) with a Chemat Technologies KW-4A spin coater at 1,200 rpm for 60 s on glass coverslips. Doped polymer beads were prepared by pouring dropwise aliquots (1.0 mL) of THF solutions of PS (44 kDa, 1.0 mg mL^{-1}) and **1**, **2** or **3** (50 μg mL^{-1}) into H$_2$O/EtOH (6:1, v/v, 5.0 mL). The resulting dispersions were maintained at ambient temperature for 3 hours in an open vial and used directly for the photolysis and spectroscopic experiments. Aliquots (10 μL) of the dispersions were transferred on glass coverslips, dried in an oven at 120 °C for 2 min and imaged. Fluorescence images were recorded with a Leica SP5 confocal laser-scanning microscope.
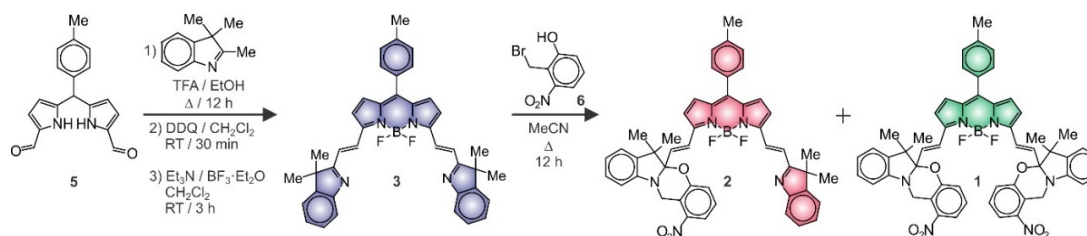
Figure 4.7 Synthesis of 1–3.

1 and **2**. A solution of **3** (200 mg, 0.32 mmol) and **6** (298 mg, 1.3 mmol) in MeCN (30 mL) was heated under reflux for 12 hours. The solvent was distilled off under reduced pressure and the residue was purified by column chromatography [SiO$_2$, hexanes/AcOEt (95:5 → 90:10, v/v)] to give **1** (30 mg, 10%) as a pink solid and **2** (20 mg, 10%) as a purple solid. **1**: ESIMS: *m/z* = 923.3530 [M + H]$^+$ (*m/z* calcd. for C$_{54}$H$_{46}$BF$_2$N$_6$O$_6$ = 923.3540);

^{1}H NMR (CD3Cl): δ = 7.75 (1H, d, 8 Hz), 7.64 (1H, d, 8 Hz), 7.44 (2H, d, 16 Hz), 7.37–7.29 (5H, m), 7.26–7.23 (1H, m), 7.21–7.07 (6H, m), 6.90 (2H, t, 7 Hz), 6.82–6.73 (4H, m), 6.69 (2H, d, 8 Hz), 6.64–6.56 (2H, m), 5.14 (2H, d, 19 Hz), 4.84 (2H, d, 19 Hz), 2.46 (3H, s), 1.64 (6H, s), 1.26 (6H, s); ^{13}C NMR [(CD$_3$)$_2$CO]: δ = 154.73, 152.94, 147.30, 146.84, 140.77, 137.90, 135.96, 132.51, 131.04, 130.32, 129.13, 127.78, 127.41, 123.85, 123.76, 122.31, 120.64, 117.71, 117.52, 116.89, 108.76, 101.48, 101.35, 50.49, 39.87, 34.67, 31.58, 29.06, 26.37, 25.28, 22.64, 21.40, 20.69, 18.77, 14.10, 11.41. **2**: ESIMS: *m/z* = 772.3288 [M + H]$^+$ (m/z calcd. for C$_{47}$H$_{41}$BF$_2$N$_5$O$_3$ = 772.3271); ^{1}H NMR (CD$_3$CN): δ = 8.14 (1H, d, 16 Hz), 7.69 (2H, dd, 1 and 8 Hz), 7.50 (4H, t, 7 Hz), 7.46–7.36 (6H, m), 7.32 (1H, dd, 1 and 7 Hz), 7.28 (1H, dd, 1 and 8 Hz), 7.25–7.21 (2H, m), 7.12 (1H, td, 1 and 8 Hz), 7.08 (1H, d, 5 Hz), 6.97 (2H, t, 5 Hz), 6.89 (1H, td, 1 and 8 Hz), 6.80 (1H, d, 8 Hz), 5.10 (1H, d, 19 Hz), 4.87 (1H, d, 19 Hz), 2.47 (3H, s), 1.62 (3H, s), 1.50 (6H, d, 3 Hz), 1.25 (3H, s).

3. A solution of **5** (500 mg, 1.7 mmol), 2,3,3-trimethyl-3*H*-indole (1.08 mg, 6.8 mmol) and trifluoroacetic acid (TFA, 50 μL, 0.7 mmol) in EtOH (30 mL) was heated under reflux for 12 hours. After cooling down to ambient temperature, the solvent was distilled off under reduced pressure. The residue was dissolved in AcOEt (50 mL) and washed with aqueous HCl (1 M, 3 × 50 mL). The organic layer was dried over Na$_2$SO$_4$ and the solvent was distilled off under reduced pressure. The residue was dissolved in CH$_2$Cl$_2$ (30 mL) and the resulting solution was degassed with Ar. 2,3-Dichloro-5,6-dicyano-1,4-benzoquinone (DDQ, 454 mg, 2.0 mmol) was added and the solution was stirred at ambient temperature under Ar for 30 min. After the sequential addition of Et$_3$N (3 mL, 21.5 mmol) and BF$_3$·Et$_2$O (3 mL, 23.4 mmol), the mixture was stirred for a further 3 hours under the

same conditions and washed with a saturated aqueous solution of $NaHCO_3$ (3×30 mL). The organic layer was dried over Na_2SO_4 and the solvent was distilled off under reduced pressure. The residue was purified by column chromatography [SiO_2, hexanes/AcOEt ($95:5 \rightarrow 70:30$, v/v)] to give **3** (120 mg, 12%) as a dark green solid. ESIMS: $m/z =$ 621.3021 $[M + H]^+$ (*m/z* calcd. for $C_{40}H_{36}BF_2N_4 = 621.3001$); ^1H NMR [$(CD_3)_2CO$]: $\delta =$ 8.41 (2H, d, 16 Hz), 7.67–7.58 (6H, m), 7.53–7.47 (3H, m), 7.46 (3H, d, 5 Hz), 7.42–7.37 (2H, m), 7.31 (2H, t, 7 Hz), 7.07 (2H, d, 4 Hz), 2.50 (3H, s), 1.53 (12H, s); ^{13}C NMR [$(CD_3)_2CO$]: $\delta = 182.37, 154.43, 153.68, 147.23, 140.96, 137.30, 130.96, 130.68, 130.58,$ 129.29, 127.88, 127.48, 126.95, 126.37, 121.43, 121.20, 118.35, 52.66, 48.44, 39.30, 22.66, 20.58.

Nematode Imaging. *Caenorhabditis elegans* KG1180 *lite-1(ce314)* strain[266] was grown at 20 °C on standard nematode growth medium (NGM) plates seeded with *Escherichia coli* OP50 bacteria and used for imaging experiments, as described previously[263, 266]. A dispersion of PS beads (0.02 mg mL^{-1}), doped with **1** (5% w/w), in sterile phosphate buffer saline (100 μL) was deposited dropwise on a standard seeded NGM plate. Age-matched adult hermaphrodites (~24 hours past the L4 larval stage) were transferred onto the plate and incubated at 20 °C for 2–5 hours to allow the bead uptake. Nematodes were transferred into a drop (~3 μL) of a H_2O solution of muscimol (10 mM) deposited on a 3% agarose pad prepared on a glass slide. After paralysis, the worms were covered with a coverslip, transferred on the stage of a confocal laser-scanning microscope and imaged. Muscimol allowed the retention of the fluorescent beads in the gut lumen during long-term imaging. At the end of the experiment, the coverslip was removed and the worms were transferred back to seeded NGM plates to reverse the muscimol block and confirm animal viability.
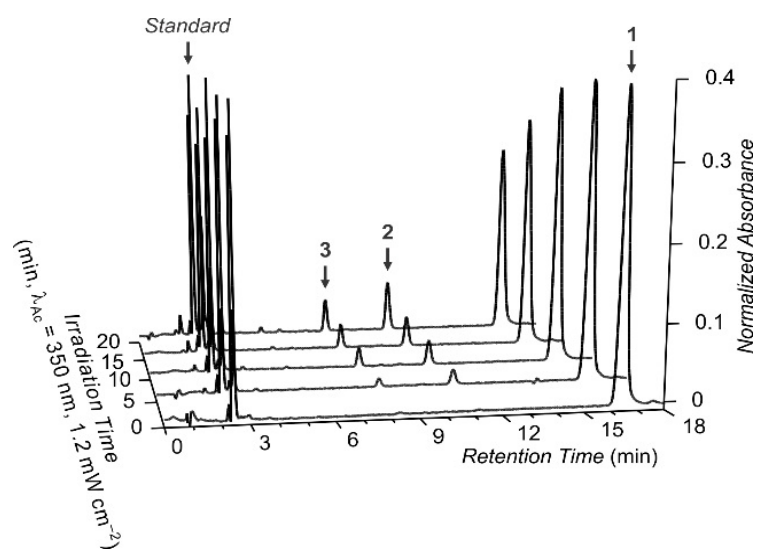
Figure 4.8 Chromatograms recorded before and after irradiation of a MeCN solution of **1** (10 μM) at 25 °C.
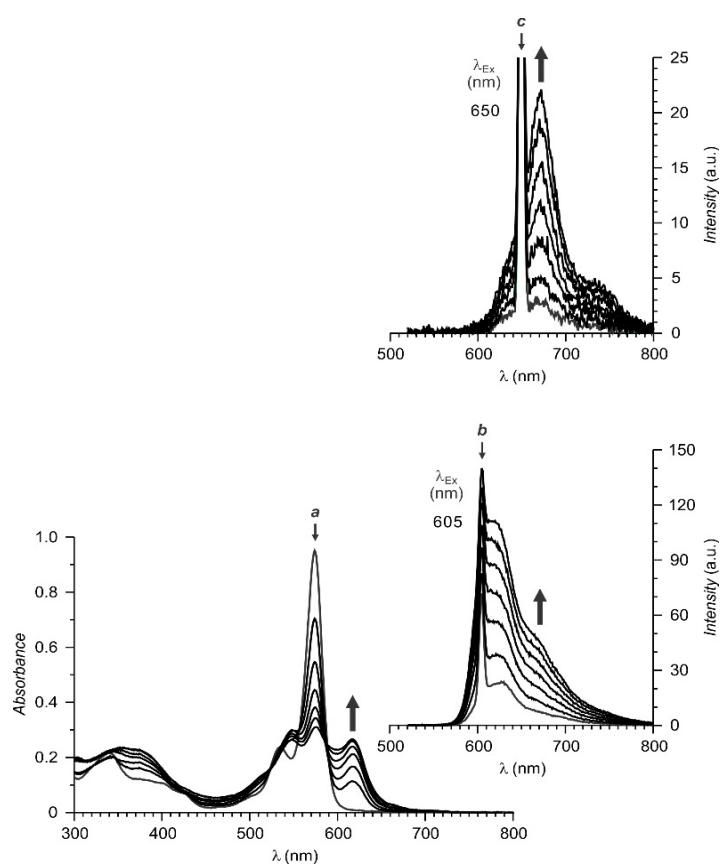
Figure 4.9 Absorption (*a*) and emission (*b* and *c*) spectra recorded before and during the photolysis (λ_{Ac} = 350 nm, 4.2 mW cm^{-2}) of a MeCN solution of **1** (10 μM) for 30 min at 25 °C.

Table 4.1 Absorption (λ_{Ab}) and emission (λ_{Em}) wavelengths, molar absorption coefficient (ε), fluorescence quantum yield (ϕ_F), brightness ($\varepsilon \times \phi_F$) and activation quantum yield (ϕ_A) of **1**–**3** in aerated MeCN at 25 °C [a].

	λ_{Ab} (nm)	λ_{Em} (nm)	ε (mM^{-1} cm^{-1})	ϕ_F (10^{-2})	$\varepsilon \times \phi_F$ (mM^{-1} cm^{-1})	ϕ_A (10^{-3})
1	574	600	95.1	1	1	5
2	619	628	69.5	4	3	1
3	663	673	84.5	16	14	—

[a] The values of ϕ_F were determined against EtOH solutions of either the acetate salt of Cresyl Violet ($\phi_F = 0.54$) or the perchlorate salt of Oxazine 1 ($\phi_F = 0.15$). The values of ϕ_A were determined against a potassium ferrioxalate actinometer from the temporal evolutions of the concentrations of **1**–**3** monitored by HPLC during photolysis.
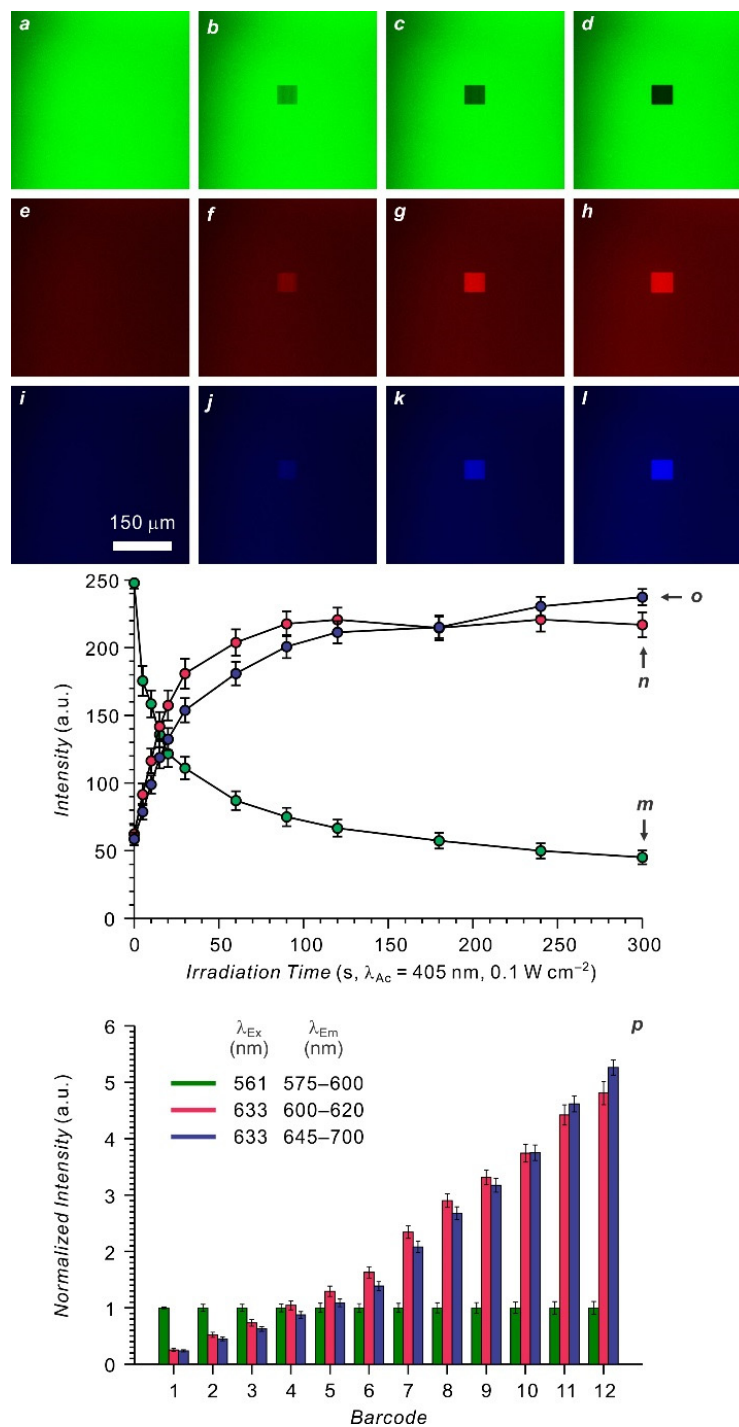
Figure 4.10 Fluorescence images of a PMMA film, doped with **1** (0.25% w/w), before (**a**, **e** and **i**) and after (**b–d**, **f–h** and **j–l**) irradiation of a square in the center of the imaging field for increasing times, temporal evolutions of the average emission intensities (**m–o**), measured in the central square, and corresponding relative emission intensities (**p**).
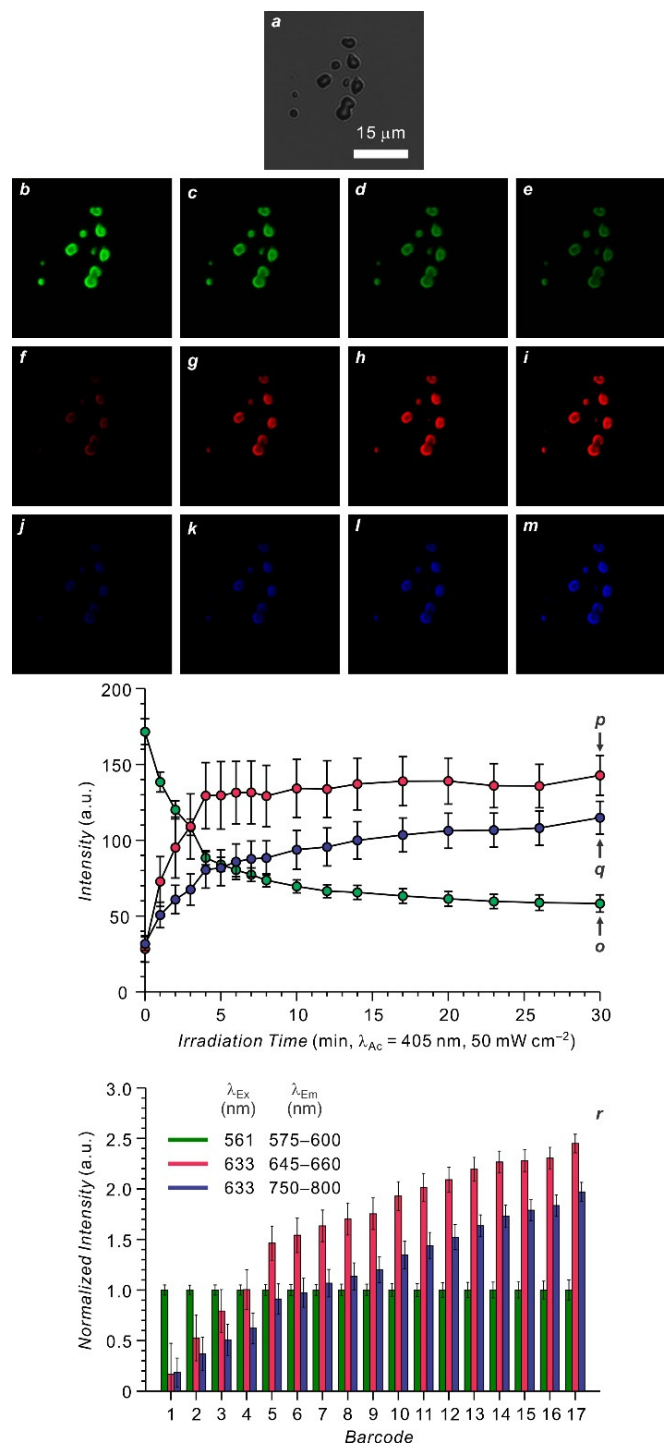
Figure 4.11 Brightfield (*a*) and fluorescence images of PS beads, doped with **1** (5% w/w), recorded before (*b*, *f* and *j*) and after (*c–e*, *g–i* and *k–m*) irradiation of the entire imaging field for increasing times, temporal evolutions of the emission intensities (*o–q*), averaged across five beads, and corresponding relative emission intensities (*r*).
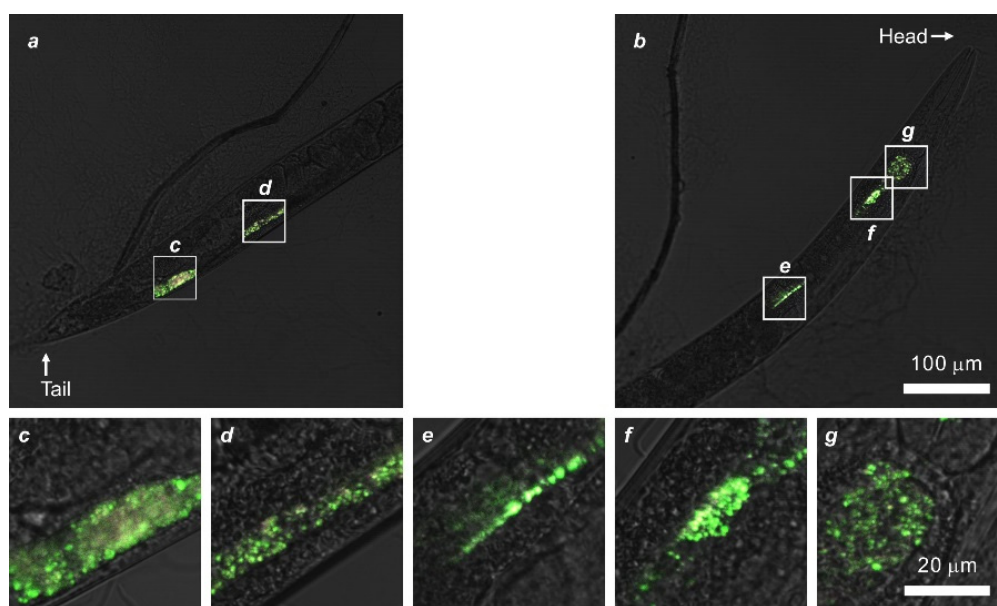
Figure 4.12 Overlaps (*a* and *b*) of brightfield images and three fluorescence channels (green: λ_{Ex} = 561 nm, λ_{Em} = 575–600 nm; red: λ_{Ex} = 633 nm, λ_{Em} = 645–660 nm; blue: λ_{Ex} = 633 nm, λ_{Em} = 750–800 nm) of a *C. elegans* labeled with PS beads, doped with **1** (5% w/w), and magnifications (*c*–*g*) of selected regions.

Reference

1.   Lakowicz, J. R., *Principles of fluorescence spectroscopy*. Springer: New York, USA, 2006.

2.   Fass, L., Imaging and cancer: a review. *Mol Oncol* **2008,** *2* (2), 115-52.

3.   Choy, G.; Choyke, P.; Libutti, S. K., Current advances in molecular imaging: noninvasive in vivo bioluminescent and fluorescent optical imaging in cancer research. *Mol. Imaging* **2003,** *2* (4), 303-312.

4.   Matsumura, Y., Poly (amino acid) micelle nanocarriers in preclinical and clinical studies. *Adv Drug Deliv Rev* **2008,** *60* (8), 899-914.

5.   Subramaniam, V.; Li, H.; Wong, M.; Kitching, R.; Attisano, L.; Wrana, J.; Zubovits, J.; Burger, A. M.; Seth, A., The RING-H2 protein RNF11 is overexpressed in breast cancer and is a target of Smurf2 E3 ligase. *Br J Cancer* **2003,** *89* (8), 1538-44.

6.   Weiss, R. B.; Donehower, R. C.; Wiernik, P. H.; Ohnuma, T.; Gralla, R. J.; Trump, D. L.; James R. Baker, J.; Echo, D. A. V.; Hoff, D. D. V.; Leyland-Jones, B., Hypersensitivity reactions from taxol. *J. Clin. Oncol* **1990,** *8*, 1263-1268.

7.   Rijcken, C. J.; Soga, O.; Hennink, W. E.; van Nostrum, C. F., Triggered destabilisation of polymeric micelles and vesicles by changing polymers polarity: an attractive tool for drug delivery. *J Control Release* **2007,** *120* (3), 131-48.

8.   Wurth, C.; Hoffmann, K.; Behnke, T.; Ohnesorge, M.; Resch-Genger, U., Polymer- and glass-based fluorescence standards for the near infrared (NIR) spectral region. *J Fluoresc* **2011,** *21* (3), 953-61.

9.   Jamme, F.; Kascakova, S.; Villette, S.; Allouche, F.; Pallu, S.; Rouam, V.; Refregiers, M., Deep UV autofluorescence microscopy for cell biology and tissue histology. *Biol Cell* **2013,** *105* (7), 277-88.

10.   Smith, A. M.; Mancini, M. C.; Nie, S., Bioimaging: second window for in vivo imaging. *Nat Nanotechnol* **2009,** *4* (11), 710-1.

11.   Reineck, P.; Gibson, B. C., Near-infrared fluorescent nanomaterials for bioimaging and sensing. *Adv Opt Mater* **2017,** *5* (2), 1600446.

12.   Barnes, K. D.; Shafirstein, G.; Webber, J. S.; Koonce, N. A.; Harris, Z.; Griffin, R. J., Hyperthermia-enhanced indocyanine green delivery for laser-induced thermal ablation of carcinomas. *Int J Hyperthermia* **2013,** *29* (5), 474-9.

13.   Mishra, A.; Behera, R. K.; Behera, P. K.; Mishra, B. K.; Behera, G. B., Cyanines during the 1990s: a review. *Chem. Rev.* **2000,** *100,* 1973-2011.

14.   Yuan, L.; Lin, W.; Zheng, K.; He, L.; Huang, W., Far-red to near infrared analyte-responsive fluorescent probes based on organic fluorophore platforms for fluorescence imaging. *Chem Soc Rev* **2013,** *42* (2), 622-61.

15.   Landsman, M. L. J.; Kwant, G.; Mook, G. A.; Zijlstra, W. G., Light-absorbing properties, stability, and spectral stabilization of indocyanine green *J Appl Phys* **1976,** *40* (4), 575-583.

16.   Ishizawa, T.; Bandai, Y.; Harada, N.; Muraoka, A.; Ijichi, M.; Kusaka, K.; Shibasaki, M.; Kokudo, N., Indocyanine green-fluorescent imaging of hepatocellular carcinoma during laparoscopic hepatectomy: an initial experience. *Asian J Endosc Surg* **2010,** *3* (1), 42-45.

17.   Ishizawa, T.; Fukushima, N.; Shibahara, J.; Masuda, K.; Tamura, S.; Aoki, T.; Hasegawa, K.; Beck, Y.; Fukayama, M.; Kokudo, N., Real-time identification of liver cancers by using indocyanine green fluorescent imaging. *Cancer* **2009,** *115* (11), 2491-504.

18.   Umezawa, K.; Matsui, A.; Nakamura, Y.; Citterio, D.; Suzuki, K., Bright, color-tunable fluorescent dyes in the Vis/NIR region: establishment of new "tailor-made" multicolor fluorophores based on borondipyrromethene. *Chemistry* **2009,** *15* (5), 1096-106.

19.   Górecki, T.; Patonay, G.; Strekowski, L.; Chin, R.; Salazar, N., Synthesis of novel near-infrared cyanine dyes for metal ion determination. *J Heterocyclic Chem* **1996,** *33* (6), 1871-1876.

20.   Patonay, G.; Antoine, M. D.; Devanathan, S.; Strekowski, L., Near-infrared probe for determination of solvent hydrophobicity. *Appl Spectrosc* **1991,** *45* (3), 457-461.

21.   James, N. S.; Chen, Y.; Joshi, P.; Ohulchanskyy, T. Y.; Ethirajan, M.; Henary, M.; Strekowsk, L.; Pandey, R. K., Evaluation of polymethine dyes as potential probes for near infrared fluorescence imaging of tumors: part - 1. *Theranostics* **2013,** *3* (9), 692-702.

22.   Yarmoluk, S. M.; Kovalska, V. B.; Lukashov, S. S.; Slominskii, Y. L., Interaction of cyanine dyes with nucleic acids. xii.~-substituted carbocyanines as possible fluorescent probes for nucleic acids detection. *Bioorg Med Chem Lett* **1999,** *9* (12), 1677-1678.

23.   Kovalska, V. B.; Volkova, K. D.; Losytskyy, M. Y.; Tolmachev, O. I.; Balanda, A. O.; Yarmoluk, S. M., 6,6'-Disubstituted benzothiazole trimethine cyanines--new fluorescent dyes for DNA detection. *Spectrochim Acta A Mol Biomol Spectrosc* **2006,** *65* (2), 271-7.

24.   Chen, X.; Peng, X.; Cui, A.; Wang, B.; Wang, L.; Zhang, R., Photostabilities of novel heptamethine 3H-indolenine cyanine dyes with different N-substituents. *J Photoch Photobio A* **2006,** *181* (1), 79-85.

25.   Song, F.; Peng, X.; Lu, E.; Zhang, R.; Chen, X.; Song, B., Syntheses, spectral properties and photostabilities of novel water-soluble near-infrared cyanine dyes. *J Photoch Photobio A* **2004,** *168* (1-2), 53-57.

26.   Peng, X.; Song, F.; Lu, E.; Wang, Y.; Zhou, W.; Fan, J.; Gao, Y., Heptamethine cyanine dyes with a large stokes shift and strong fluorescence: a paradigm for excited-state intramolecular charge transfer. *J Am Chem Soc* **2005,** *127* (12), 4170-4171.

27.   Zhou, L.-C.; Zhao, G.-J.; Liu, J.-F.; Han, K.-L.; Wu, Y.-K.; Peng, X.-J.; Sun, M.-T., The charge transfer mechanism and spectral properties of a near-infrared heptamethine cyanine dye in alcoholic and aprotic solvents. *J Photoch Photobio A* **2007,** *187* (2-3), 305-310.

28.   Kim, J. S.; Kodagahally, R.; Strekowski, L.; Patonay, G., A study of intramolecular H-complexes of novel bis(heptamethine cyanine) dyes. *Talanta* **2005,** *67* (5), 947-54.

29.   Wang, T.; Zhao, Q. J.; Hu, H. G.; Yu, S. C.; Liu, X.; Liu, L.; Wu, Q. Y., Spirolactonized Si-rhodamine: a novel NIR fluorophore utilized as a platform to construct Si-rhodamine-based probes. *Chem Commun* **2012,** *48* (70), 8781-3.

30.   Koide, Y.; Urano, Y.; Hanaoka, K.; Piao, W.; Kusakabe, M.; Saito, N.; Terai, T.; Okabe, T.; Nagano, T., Development of NIR fluorescent dyes based on Si-rhodamine for in vivo imaging. *J Am Chem Soc* **2012,** *134* (11), 5029-31.

31.   Koide, Y.; Kawaguchi, M.; Urano, Y.; Hanaoka, K.; Komatsu, T.; Abo, M.; Terai, T.; Nagano, T., A reversible near-infrared fluorescence probe for reactive oxygen species based on Te-rhodamine. *Chem Commun* **2012,** *48* (25), 3091-3.

32.   Boens, N.; Leen, V.; Dehaen, W., Fluorescent indicators based on BODIPY. *Chem Soc Rev* **2012,** *41* (3), 1130-72.

33.   Palma, A.; Tasior, M.; Frimannsson, D. O.; Vu, T. T.; Me´allet-Renault, R.; O'Shea, D. F., New on-bead near-infrared fluorophores and fluorescent sensor constructs. *Org Lett* **2009,** *11* (16), 3638-3641.

34.   Killoran, J.; McDonnell, S. O.; Gallagher, J. F.; O'Shea, D. F., A substituted BF2-chelated tetraarylazadipyrromethene as an intrinsic dual chemosensor in the 650–850 nm spectral range. *New J. Chem.* **2008,** *32* (3), 483-489.

35.   Zhang, Y.; Swaminathan, S.; Tang, S.; Garcia-Amorós, J.; Boulina, M.; Captain, B.; Baker, J. D.; Raymo, F. i. M., Photoactivatable BODIPYs designed to monitor the dynamics of supramolecular nanocarriers. *J Am Chem Soc* **2015,** *137* (14), 4709-4719.

36.   Liu, X.; Zhang, Y.; Baker, J. D.; Raymo, F. M., A photoactivatable light tracer. *J Mater Chem C* **2017,** *5* (48), 12714-12719.

37.   Thapaliya, E. R.; Zhang, Y.; Raymo, F. M., Fluorescence patterning with mild illumination in polymer films of photocleavable oxazines. *J Mater Chem C* **2017,** *5* (5), 1179-1183.

38.   Thapaliya, E. R.; Zhang, Y.; Dhakal, P.; Brown, A. S.; Wilson, J. N.; Collins, K. M.; Raymo, F. M., Bioimaging with macromolecular probes incorporating multiple bodipy fluorophores. *Bioconjug Chem* **2017,** *28* (5), 1519-1528.

39.   Zhang, Y.; Tang, S.; Sansalone, L.; Baker, J. D.; Raymo, F. M., A photoswitchable fluorophore for the real‐time monitoring of dynamic events in living organisms. *Chem-Eur J* **2016,** *22* (42), 15027-15034.

40.   Ni, Y.; Wu, J., Far-red and near infrared BODIPY dyes: synthesis and applications for fluorescent pH probes and bio-imaging. *Org Biomol Chem* **2014,** *12* (23), 3774-91.

41.   Sarma, T.; Panda, P. K.; Setsune, J., Bis-naphthobipyrrolylmethene derived BODIPY complex: an intense near-infrared fluorescent dye. *Chem Commun* **2013,** *49* (84), 9806-8.

42.   Zhang, T.; Zhu, X.; Wong, W. K.; Tam, H. L.; Wong, W. Y., Light-harvesting ytterbium(III)-porphyrinate-BODIPY conjugates: synthesis, excitation-energy transfer, and two-photon-induced near-infrared-emission studies. *Chemistry* **2013,** *19* (2), 739-48.

43.   Schellhammer, K. S.; Li, T.-Y.; Zeika, O.; Körner, C.; Leo, K.; Ortmann, F.; Cuniberti, G., Tuning Near-Infrared Absorbing Donor Materials: A study of electronic, optical, and charge-transport properties of aza-BODIPYs. *Chem Mater* **2017,** *29* (13), 5525-5536.

44.   Burghart, A.; Kim, H.; Welch, M. B.; Thoresen, L. H.; Reibenspies, J.; Burgess, K., 3,5-Diaryl-4,4-difluoro-4-bora-3a,4a-diaza-s-indacene (BODIPY) Dyes: synthesis, spectroscopic, electrochemical, and structural properties. *J Org Chem* **1999,** *64*, 7813-7819.

45.   Chen, J.; Burghart, A.; Derecskei-Kovacs, A.; Burgess, K., 4,4-Difluoro-4-bora-3a,4a-diaza-s-indacene (BODIPY) dyes modified for extended conjugation and restricted bond rotations. *J Org Chem* **2000,** *65*, 2900-2906.

46.   Yang, Y.; Guo, Q.; Chen, H.; Zhou, Z.; Guo, Z.; Shen, Z., Thienopyrrole-expanded BODIPY as a potential NIR photosensitizer for photodynamic therapy. *Chem Commun* **2013,** *49* (38), 3940-2.

47.   Wang, J.; Hou, Y.; Lei, W.; Zhou, Q.; Li, C.; Zhang, B.; Wang, X., DNA photocleavage by a cationic BODIPY dye through both singlet oxygen and hydroxyl radical: new insight into the photodynamic mechanism of BODIPYs. *Chemphyschem* **2012,** *13* (11), 2739-47.

48.   McEwen, J. J.; Wallace, K. J., Squaraine dyes in molecular recognition and self-assembly. *Chem Commun* **2009,** (42), 6339-51.

49.   Volkova, K. D.; Kovalska, V. B.; Tatarets, A. L.; Patsenker, L. D.; Kryvorotenko, D. V.; Yarmoluk, S. M., Spectroscopic study of squaraines as protein-sensitive fluorescent dyes. *Dyes and Pigments* **2007,** *72* (3), 285-292.

50.   Dilek, G.; Akkaya, E. U., Novel squaraine signalling Zn(II) ions: three-state fluorescence response to a single input. *Tetrahedron Lett* **2000,** *41* (19), 3721-3724.

51.   Gayathri Devi, D.; Cibin, T. R.; Ramaiah, D.; Abraham, A., Bis(3,5-diiodo-2,4,6-trihydroxyphenyl)squaraine: a novel candidate in photodynamic therapy for skin cancer models in vivo. *J Photochem Photobiol B* **2008,** *92* (3), 153-9.

52.   Umezama, K.; Citterio, D.; Suzuki, K., Water-soluble NIR fluorescent probes based on squaraine and their application for protein labeling. *Anal Sci* **2008,** *24* (2), 213-7.

53.   Gassensmith, J. J.; Baumes, J. M.; Smith, B. D., Discovery and early development of squaraine rotaxanes. *Chem Commun* **2009,** (42), 6329-38.

54.   Jiang, J.; NG, D. K. P., A decade journey in the chemistry of sandwich-type tetrapyrrolato-rare earth complexes. *Acc Chem Res.* **2008,** *42* (1), 79-88.

55.   de la Torre, G.; Claessens, C. G.; Torres, T., Phthalocyanines: old dyes, new materials. Putting color in nanotechnology. *Chem. Commun.* **2007,** (20), 2000-2015.

56.   Luo, S.; Zhang, E.; Su, Y.; Cheng, T.; Shi, C., A review of NIR dyes in cancer targeting and imaging. *Biomaterials* **2011,** *32* (29), 7127-38.

57.   Tanaka, Y.; Shin, J.-Y.; Osuka, A., Facile synthesis of largemeso-pentafluorophenyl-substituted expanded porphyrins. *Eur J Org Chem* **2008,** *2008* (8), 1341-1349.

58.   Xie, Y. S.; Yamaguchi, K.; Toganoh, M.; Uno, H.; Suzuki, M.; Mori, S.; Saito, S.; Osuka, A.; Furuta, H., Triply N-confused hexaphyrins: near-infrared luminescent dyes with a triangular shape. *Angew Chem Int Ed Engl* **2009,** *48* (30), 5496-9.

59.   Kuimova, M. K.; Collins, H. A.; Balaz, M.; Dahlstedt, E.; Levitt, J. A.; Sergent, N.; Suhling, K.; Drobizhev, M.; Makarov, N. S.; Rebane, A.; Anderson, H. L.; Phillips, D., Photophysical properties and intracellular imaging of water-soluble porphyrin dimers for two-photon excited photodynamic therapy. *Org Biomol Chem* **2009,** *7* (5), 889-96.

60.   Celli, J. P.; Spring, B. Q.; Rizvi, I.; Evans, C. L.; Samkoe, K. S.; Verma, S.; Pogue, B. W.; Hasan, T., Imaging and photodynamic therapy: mechanisms, monitoring, and optimization. *Chem Rev* **2010,** *110* (5), 2795-838.

61.   Hu, M.; Brasseur, N.; Yildiz, S. Z.; Lier, J. E. v.; Leznoff, C. C., Hydroxyphthalocyanines as potential photodynamic agents for cancer therapy. *J Med Chem* **1998,** *41* (11), 1789-802.

62.   Karunakaran, S. C.; Babu, P. S.; Madhuri, B.; Marydasan, B.; Paul, A. K.; Nair, A. S.; Rao, K. S.; Srinivasan, A.; Chandrashekar, T. K.; Rao Ch, M.; Pillai, R.; Ramaiah, D., In vitro demonstration of apoptosis mediated photodynamic activity and NIR nucleus imaging through a novel porphyrin. *ACS Chem Biol* **2013,** *8* (1), 127-32.

63.   Sansalone, L.; Tang, S.; Zhang, Y.; Thapaliya, E. R.; Raymo, F. M.; Garcia-Amorós, J., Semiconductor quantum dots with photoresponsive ligands. *Topics in Current Chemistry* **2016,** *374* (5), 73.

64.   Lu, Y.; Su, Y.; Zhou, Y.; Wang, J.; Peng, F.; Zhong, Y.; Huang, Q.; Fan, C.; He, Y., In vivo behavior of near infrared-emitting quantum dots. *Biomaterials* **2013,** *34* (17), 4302-8.

65.   Medintz, I. L.; Uyeda, H. T.; Goldman, E. R.; Mattoussi, H., Quantum dot bioconjugates for imaging, labelling and sensing. *Nat Mater* **2005,** *42*, 435-46.

66.   Gu, Y. P.; Cui, R.; Zhang, Z. L.; Xie, Z. X.; Pang, D. W., Ultrasmall near-infrared Ag$_2$Se quantum dots with tunable fluorescence for in vivo imaging. *J Am Chem Soc* **2012,** *134* (1), 79-82.

67.   Helle, M.; Cassette, E.; Bezdetnaya, L.; Pons, T.; Leroux, A.; Plenat, F.; Guillemin, F.; Dubertret, B.; Marchal, F., Visualisation of sentinel lymph node with indium-based near infrared emitting Quantum Dots in a murine metastatic breast cancer model. *PLoS One* **2012,** *7* (8), e44433.

68.   Xue, B.; Cao, J.; Deng, D.; Xia, J.; Jin, J.; Qian, Z.; Gu, Y., Four strategies for water transfer of oil-soluble near-infrared-emitting PbS quantum dots. *J Mater Sci Mater Med* **2012,** *23* (3), 723-32.

69.   Cao, J.; Zhu, H.; Deng, D.; Xue, B.; Tang, L.; Mahounga, D.; Qian, Z.; Gu, Y., In vivo NIR imaging with PbS quantum dots entrapped in biodegradable micelles. *J Biomed Mater Res A* **2012,** *100* (4), 958-68.

70.   Tuncel, D.; Demir, H. V., Conjugated polymer nanoparticles. *Nanoscale* **2010,** *2* (4), 484-94.

71.   Ma, X.; Tao, F.; Zhang, Y.; Li, T.; Raymo, F. M.; Cui, Y., Detection of nitroaromatic explosives by a 3D hyperbranched σ–π conjugated polymer based on a POSS scaffold. *J Mater Chem A* **2017,** *5* (27), 14343-14354.

72.   Boudreault, P.-L. T.; Najari, A.; Leclerc, M., Processable low-bandgap polymers for photovoltaic applications. *Chem Mater* **2011,** *23* (3), 456-469.

73.   Yen, H.-J.; Shan, C.; Wang, L.; Xu, P.; Zhou, M.; Wang, H.-L., Development of conjugated polymers for memory device applications. *Polymers* **2017,** *9* (1), 25.

74.   Braeken, Y.; Cheruku, S.; Ethirajan, A.; Maes, W., Conjugated polymer nanoparticles for bioimaging. *Materials (Basel)* **2017,** *10* (12).

75.   Kahveci, Z.; Vazquez-Guillo, R.; Martinez-Tome, M. J.; Mallavia, R.; Mateo, C. R., New red-emitting conjugated polyelectrolyte: stabilization by interaction with biomolecules and potential use as drug carriers and bioimaging probes. *ACS Appl Mater Interfaces* **2016,** *8* (3), 1958-69.

76.   Ma, M.; Lei, M.; Tan, X.; Tan, F.; Li, N., Theranostic liposomes containing conjugated polymer dots and doxorubicin for bio-imaging and targeted therapeutic delivery. *RSC Advances* **2016,** *6* (3), 1945-1957.

77.   Yu, J.; Rong, Y.; Kuo, C. T.; Zhou, X. H.; Chiu, D. T., Recent advances in the development of highly luminescent semiconducting polymer dots and nanoparticles for biological imaging and medicine. *Anal Chem* **2017,** *89* (1), 42-56.

78.   Liu, H. Y.; Wu, P. J.; Kuo, S. Y.; Chen, C. P.; Chang, E. H.; Wu, C. Y.; Chan, Y. H., Quinoxaline-based polymer dots with ultrabright red to near-infrared fluorescence for in vivo biological imaging. *J Am Chem Soc* **2015,** *137* (32), 10420-9.

79.   Weber, S. E., Polymer micelles: an example of self-assembling polymers. *J Phys Chem B.* **1998,** *102*, 2618-26.

80.   Lodge, T. P., Block copolymers: past successes and future challenges. *Macromol Chem Phys.* **2003,** *204*, 265-73.

81.   Riess, G., Micellization of block copolymers. *Progress in Polymer Science* **2003,** *28* (7), 1107-1170.

82.   Moffitt, M.; Khougaz, K.; Eisenberg, A., Micellization of ionic block copolymers. *Acc chem Res.* **1996,** *29*, 95-102.

83.   Moughton, A. O.; Hillmyer, M. A.; Lodge, T. P., Multicompartment block polymer micelles. *Macromolecules* **2011,** *45* (1), 2-19.

84.   Owen, S. C.; Chan, D. P. Y.; Shoichet, M. S., Polymeric micelle stability. *Nano Today* **2012,** *7* (1), 53-65.

85.   Kale, T. S.; Klaikherd, A.; Popere, B.; Thayumanavan, S., Supramolecular assemblies of amphiphilic homopolymers. *Langmuir* **2009,** *25* (17), 9660-70.

86.   Cameron, N. S.; Corbierre, M. K.; Eisenberg, A., Asymmetric amphiphilic block copolymers in solution: a morphological wonderland1. *Can J Chem* **1999,** *77*, 1311-26.

87.   Thapaliya, E. R.; Fowley, C.; Callan, B.; Tang, S.; Zhang, Y.; Callan, J. F.; Raymo, F. i. M., Energy-transfer schemes to probe fluorescent nanocarriers and their emissive cargo. *Langmuir* **2015,** *31* (35), 9557-9565.

88.   Pietropaolo, A.; Tang, S.; Raymo, F. M., Free-energy predictions and absorption spectra calculations for supramolecular nanocarriers and their photoactive cargo. *Nanoscale* **2017,** *9* (15), 4989-4994.

89.   Garcia-Amorós, J.; Tang, S.; Zhang, Y.; Thapaliya, E. R.; Raymo, F. M., Self-Assembling nanoparticles of amphiphilic polymers for in vitro and in vivo fret imaging. In *Light-responsive nanostructured systems for applications in nanomedicine*, Springer, Cham: 2016; pp 29-59.

90.   Zhang, Y.; Thapaliya, E. R.; Tang, S.; Baker, J. D.; Raymo, F. M., Supramolecular delivery of fluorescent probes in developing embryos. *RSC Advances* **2016,** *6* (76), 72756-72760.

91.   Zhang, Y.; Tang, S.; Sansalone, L.; Thapaliya, E. R.; Baker, J. D.; Raymo, F. M. Supramolecular delivery of photoactivatable fluorophores in developing embryos, *Proc. SPIE*, **2017**; 100781A.

92.   Zhang, Y.; Tang, S.; Thapaliya, E. R.; Raymo, F. M. Supramolecular nanocarriers with photoresponsive cargo, *Proc. SPIE*, **2016**; 97220C.

93.   Swaminathan, S.; Fowley, C.; Thapaliya, E. R.; McCaughan, B.; Tang, S.; Fraix, A.; Captain, B.; Sortino, S.; Callan, J. F.; Raymo, F. M., Supramolecular nanoreactors for intracellular singlet-oxygen sensitization. *Nanoscale* **2015,** *7* (33), 14071-14079.

94.   Ragab, S. S.; Thapaliya, E. R.; Zhang, Y.; Tang, S.; McMahan, J. B.; Syed, S.; Captain, B.; Raymo, F. M., Synthesis in living cells with the assistance of supramolecular nanocarriers. *RSC Advances* **2016,** *6* (39), 32441-32445.

95.   Kataoka, K.; Kwon, G. S.; Yokoyama, M.; Okano, T.; Sakurai, Y., Block copolymer micelles as vehicles for drug delivery. *J Control Release* **1993,** 119-132.

96.   Torchilin, V. P., Structure and design of polymeric surfactant-based drug delivery systems. *J Control Release* **2001,** *73*, 131-72.

97.   Jones, M.-C.; Leroux, J.-C., Polymeric micelles - a new generation of colloidal drug carriers. *Eur J Pharm Biopharm* **1999,** *48*, 101-11.

98.   Adams, M. L.; Lavasanifar, A.; Kwon, G. S., Amphiphilic block copolymers for drug delivery. *J Pharm Sci.* **2002,** *92* (7), 1343-55.

99.   Wang, D.; Wang, X., Amphiphilic azo polymers: molecular engineering, self-assembly and photoresponsive properties. *Progress in Polymer Science* **2013,** *38* (2), 271-301.

100.   Lalatsa, A.; Schatzlein, A. G.; Mazza, M.; Le, T. B.; Uchegbu, I. F., Amphiphilic poly(L-amino acids) - new materials for drug delivery. *J Control Release* **2012,** *161* (2), 523-36.

101.   Wang, Y.; Grayson, S. M., Approaches for the preparation of non-linear amphiphilic polymers and their applications to drug delivery. *Adv Drug Deliv Rev* **2012,** *64* (9), 852-65.

102.   Mondon, K.; Gurny, R.; Möller, M., Colloidal drug delivery systems – recent advances with polymeric micelles. *CHIMIA International Journal for Chemistry* **2008,** *62* (10), 832-840.

103.   Nicolas, J.; Mura, S.; Brambilla, D.; Mackiewicz, N.; Couvreur, P., Design, functionalization strategies and biomedical applications of targeted biodegradable/ biocompatible polymer-based nanocarriers for drug delivery. *Chem Soc Rev* **2013,** *42* (3), 1147-235.

104.   Husseini, G. A.; Pitt, W. G., Micelles and nanoparticles for ultrasonic drug and gene delivery. *Adv Drug Deliv Rev* **2008,** *60* (10), 1137-52.

105.   Kim, Y. C.; Park, J. H.; Prausnitz, M. R., Microneedles for drug and vaccine delivery. *Adv Drug Deliv Rev* **2012,** *64* (14), 1547-68.

106.   Zhuang, J.; Gordon, M. R.; Ventura, J.; Li, L.; Thayumanavan, S., Multi-stimuli responsive macromolecules and their assemblies. *Chem Soc Rev* **2013,** *42* (17), 7421-35.

107.   Tyler, J. Y.; Xu, X. M.; Cheng, J. X., Nanomedicine for treating spinal cord injury. *Nanoscale* **2013,** *5* (19), 8821-36.

108.   Alakhova, D. Y.; Kabanov, A. V., Pluronics and MDR reversal: an update. *Mol Pharm* **2014,** *11* (8), 2566-78.

109.   Lu, Y.; Park, K., Polymeric micelles and alternative nanonized delivery vehicles for poorly soluble drugs. *Int J Pharm* **2013,** *453* (1), 198-214.

110.   Park, J. H.; Lee, S.; Kim, J.-H.; Park, K.; Kim, K.; Kwon, I. C., Polymeric nanomedicine for cancer therapy. *Progress in Polymer Science* **2008,** *33* (1), 113-137.

111.   Mura, S.; Nicolas, J.; Couvreur, P., Stimuli-responsive nanocarriers for drug delivery. *Nat Mater* **2013,** *12* (11), 991-1003.

112.   Gu, L.; Faig, A.; Abdelhamid, D.; Uhrich, K., Sugar-based amphiphilic polymers for biomedical applications: from nanocarriers to therapeutics. *Acc Chem Res* **2014,** *47* (10), 2867-77.

113.   Swann, J. M. G.; Topham, P. D., Design and application of nanoscale actuators using block-copolymers. *Polymers* **2010,** *2* (4), 454-469.

114.   Förster, S.; Konrad, M., From self-organizing polymers to nano- and biomaterials. *J. Mater. Chem.* **2003,** *13* (11), 2671-2688.

115.   Bälter, M.; Li, S.; Morimoto, M.; Tang, S.; Hernando, J.; Guirado, G.; Irie, M.; Raymo, F. M.; Andréasson, J., Emission color tuning and white-light generation based on photochromic control of energy transfer reactions in polymer micelles. *Chem Sci* **2016,** *7* (9), 5867-5871.

116.   Zhao, J.; Fung, B. M., NMR Study of the transformation of sodium dodecyl sulfate micelles. *Langmuir* **1993,** *9*, 1228-1231.

117.   Chakraborty, T.; Chakraborty, I.; Ghosh, S., The methods of determination of critical micellar concentrations of the amphiphilic systems in aqueous medium. *Arabian Journal of Chemistry* **2011,** *4* (3), 265-270.

118.   Topel, Ö.; Çakır, B. A.; Budama, L.; Hoda, N., Determination of critical micelle concentration of polybutadiene-block-poly(ethyleneoxide) diblock copolymer by fluorescence spectroscopy and dynamic light scattering. *J Mol Liq* **2013,** *177*, 40-43.

119.   Prazeres, T. J. V.; Beija, M.; Fernandes, F. V.; Marcelino, P. G. A.; Farinha, J. P. S.; Martinho, J. M. G., Determination of the critical micelle concentration of surfactants and amphiphilic block copolymers using coumarin 153. *Inorganica Chimica Acta* **2012,** *381*, 181-187.

120.   Lavkush Bhaisare, M.; Pandey, S.; Shahnawaz Khan, M.; Talib, A.; Wu, H. F., Fluorophotometric determination of critical micelle concentration (CMC) of ionic and non-ionic surfactants with carbon dots via Stokes shift. *Talanta* **2015,** *132*, 572-8.

121.   Rothschild, K. J.; Asher, I. M.; Stanley, H. E.; Anastassakislc, E., Raman Spectroscopy of uncomplexed valinomycin. 2. nonpolar and polar solution. *J Am Chem Soc* **1976,** *99* (7), 2032-39.

122.   Ananthapadmanabhan, K. P.; Goddard, E. D.; Turro, N. J.; Kuot, P. L., Fluorescence probes for critical micelle concentration. *Langmuir* **1985,** *1*, 352-5.

123.   Aguiar, J.; Carpena, P.; Molina-Bolívar, J. A.; Carnero Ruiz, C., On the determination of the critical micelle concentration by the pyrene 1:3 ratio method. *J Colloid Interf Sci* **2003,** *258* (1), 116-122.

124.   Swaminathan, S.; Fowley, C.; McCaughan, B.; Cusido, J.; Callan, J. F.; Raymo, F. M., Intracellular guest exchange between dynamic supramolecular hosts. *J Am Chem Soc* **2014,** *136* (22), 7907-13.

125.	Mukherjee, I.; Moulik, S. P.; Rakshit, A. K., Tensiometric determination of Gibbs surface excess and micelle point: a critical revisit. *J Colloid Interface Sci* **2013,** *394*, 329-36.

126.	Castro, M. J. L.; Ritacco, H.; Fernández-Cirelli, J. K. a. A., A simplified method for the determination of critical micelle concentration. *J Chem Ed* **2001,** *78*, 347-8.

127.	Achilefu, S., Lighting up tumors with receptor-specific optical molecular probes. *Technol Cancer Res T* **2004,** *3* (4), 393-409.

128.	Waggoner, B. B. G. W. F. A. S.; Jaffe, D. L. F. J. M. R. R.; Mujumdar, R. B. M. S. R.; Hakala, T. R., Tumor labeling in vivo using cyanine-conjugated monoclonal antibodies. *Cancer Immunol Immun* **1995,** *41*, 257-63.

129.	Ballou, B.; Fisher, G. W.; Hakala, T. R.; Farkas, D. L., Tumor detection and visualization using cyanine fluorochrome-labeled antibodies. *Biotechnol Prog.* **1997,** *13*, 649-58.

130.	Lv, Y.; Liu, P.; Ding, H.; Wu, Y.; Yan, Y.; Liu, H.; Wang, X.; Huang, F.; Zhao, Y.; Tian, Z., Conjugated polymer-based hybrid nanoparticles with two-photon excitation and near-infrared emission features for fluorescence bioimaging within the biological window. *ACS Appl Mater Interfaces* **2015,** *7* (37), 20640-8.

131.	Li, K.; Jiang, Y.; Ding, D.; Zhang, X.; Liu, Y.; Hua, J.; Feng, S. S.; Liu, B., Folic acid-functionalized two-photon absorbing nanoparticles for targeted MCF-7 cancer cell imaging. *Chem Commun* **2011,** *47* (26), 7323-5.

132.	Zhu, S.; Li, M.; Tang, S.; Zhang, Y. M.; Yang, B.; Zhang, S. X. A., Electrochromic switching and microkinetic behaviour of oxazine derivatives and their applications. *Eur J Org Chem* **2014,** *2014* (6), 1227-1235.

133.	Zhang, Y.; Garcia-Amorós, J.; Captain, B.; Raymo, F. M., A fluorescent and halochromic indolizine switch. *J Mater Chem C* **2016,** *4* (14), 2744-2747.

134.	Zhu, S.; Li, M.; Zhang, Y.; Tang, S.; Yang, J.; Wang, Y.; Sun, L.; Sheng, L.; Yang, B.; Zhang, S. X.-A., Hyperconjugation effect on fluorescence enhancement of biomimic disulfide substituted spirooxazine. *RSC Advances* **2013,** *3* (43), 19752-19755.

135.	Zhang, Y.; Captain, B.; Raymo, F. M., A pH-gated photocage. *Adv Opt Mater* **2016,** *4* (9), 1363-1366.

136.	Thapaliya, E. R.; Fowley, C.; Callan, B.; Tang, S.; Zhang, Y.; Callan, J. F.; Raymo, F. M. Probing the intracellular fate of supramolecular nanocarriers and their cargo with FRET schemes, *Proc SPIE,* **2017**, 100781B.

137.	Li, K.; Zhang, Y.; Qiao, B.; Tao, F.; Li, T.; Ding, Y.; Raymo, F. M.; Cui, Y., Facile fabrication of AIE/AIEE-active fluorescent nanoparticles based on barbituric for cell imaging applications. *RSC Advances* **2017,** *7* (48), 30229-30241.

138.   Messerli, S. M.; Prabhakar, S.; Tang, Y.; Shah, K.; Cortes, M. L.; Murthy, V.; Weissleder, R.; Breakefield, X. O.; Tung, C. H., A novel method for imaging apoptosis using a caspase-1 near-infrared fluorescent probe. *Neoplasia* **2004,** *6* (2), 95-105.

139.   Kim, Y.-M.; Chungi, H.-T.; Simmons, R. L.; Billiar, T. R., Cellular non-heme iron content is a determinant of nitric oxide-mediated apoptosis, necrosis, and caspase inhibition. *J Biol Chem* **2000,** *275*, 10954-61.

140.   Patterson, G. H.; Lippincott-Schwartz, J., A photoactivatable gfp for selective photolabeling of proteins and cells. *Science* **2002,** *297* (1873-7).

141.   Tang, S.; Donaphon, B.; Levitus, M.; Raymo, F. M., Structural implications on the properties of self-assembling supramolecular hosts for fluorescent guests. *Langmuir* **2016,** *32* (34), 8676-87.

142.   Tang, S.; Zhang, Y.; Thapaliya, E. R.; Brown, A. S.; Wilson, J. N.; Raymo, F. M., Highlighting cancer cells with halochromic switches. *ACS Sens* **2017,** *2* (1), 92-101.

143.   Tang, S.; Zhang, Y.; Thapaliya, E. R.; Brown, A. S.; Wilson, J. N.; Raymo, F. M. Highlighting cancer cells with macromolecular probes, *Proc. SPIE*, **2017**; 1007814.

144.   Okhapkin, I. M.; Makhaeva, E. E.; Khokhlov, A. R., Water Solutions of Amphiphilic polymers: nanostructure formation and possibilities for catalysis. **2006,** *195*, 177-210.

145.   Makino, A., Morphology control of molecular assemblies prepared from bio-based amphiphilic polymers with a helical hydrophobic unit and application as nanocarriers for contrast agents and/or drug delivery. *Polymer Journal* **2014,** *46* (11), 783-791.

146.   Swaminathan, S.; Garcia-Amoros, J.; Fraix, A.; Kandoth, N.; Sortino, S.; Raymo, F. M., Photoresponsive polymer nanocarriers with multifunctional cargo. *Chem Soc Rev* **2014,** *43* (12), 4167-78.

147.   Yoo, S. I.; An, S. J.; Choi, G. H.; Kim, K. S.; Yi, G. C.; Zin, W. C.; Jung, J. C.; Sohn, B. H., Controlled light emission by nanoencapsulation of fluorophores in thin films of diblock copolymer micelles. *Adv Mater* **2007,** *19* (12), 1594-1596.

148.   Wagh, A.; Qian, S. Y.; Law, B., Development of biocompatible polymeric nanoparticles for in vivo NIR and FRET imaging. *Bioconjug Chem* **2012,** *23* (5), 981-92.

149.   Wang, R.; Peng, J.; Qiu, F.; Yang, Y., Enhanced white-light emission from multiple fluorophores encapsulated in a single layer of diblock copolymer micelles. *Chem Commun* **2011,** *47* (10), 2787-9.

150.   Yoo, S. I.; Lee, J.-H.; Sohn, B.-H.; Eom, I.; Joo, T.; An, S. J.; Yi, G.-C., Enhancement and concurrence of emissions from multiple fluorophores in a single emitting layer of micellar nanostructures. *Adv Funct Mater* **2008,** *18* (19), 2984-2989.

151.   Wu, W.-C.; Chen, C.-Y.; Tian, Y.; Jang, S.-H.; Hong, Y.; Liu, Y.; Hu, R.; Tang, B. Z.; Lee, Y.-T.; Chen, C.-T.; Chen, W.-C.; Jen, A. K. Y., Enhancement of aggregation-induced emission in dye-encapsulating polymeric micelles for bioimaging. *Adv Funct Mater* **2010,** *20* (9), 1413-1423.

152.   Chen, H.; Kim, S.; He, W.; Wang, H.; Low, P. S.; Park, K.; Cheng, J.-X., Fast release of lipophilic agents from circulating peg-pdlla micelles revealed by in viwo fo¨rster resonance energy transfer imaging. *Langmuir* **2008,** *24*, 5213-7.

153.   Javali, N. M.; Raj, A.; Saraf, P.; Li, X.; Jasti, B., Fatty acid–rgd peptide amphiphile micelles as potential paclitaxel delivery carriers to αvβ3integrin overexpressing tumors. *Pharm Res* **2012,** *29*, 3347-61.

154.   Lee, S. Y.; Tyler, J. Y.; Kim, S.; Park, K.; Cheng, J. X., FRET imaging reveals different cellular entry routes of self-assembled and disulfide bonded polymeric micelles. *Mol Pharm* **2013,** *10* (9), 3497-506.

155.   Klymchenko, A. S.; Roger, E.; Anton, N.; Anton, H.; Shulov, I.; Vermot, J.; Mely, Y.; Vandamme, T. F., Highly lipophilic fluorescent dyes in nano-emulsions: towards bright non-leaking nano-droplets. *RSC Adv* **2012,** *2* (31), 11876-11886.

156.   Bickerton, S.; Jiwpanich, S.; Thayumanavan, S., Interconnected roles of scaffold hydrophobicity, drug loading, and encapsulation stability in polymeric nanocarriers. *Mol Pharm* **2012,** *9* (12), 3569-78.

157.   Hu, P.; Tirelli, N., Inter-micellar dynamics in block copolymer micelles: FRET experiments of macroamphiphile and payload exchange. *React Funct Polym* **2011,** *71* (3), 303-314.

158.   Chen, K. J.; Chiu, Y. L.; Chen, Y. M.; Ho, Y. C.; Sung, H. W., Intracellularly monitoring/imaging the release of doxorubicin from pH-responsive nanoparticles using Forster resonance energy transfer. *Biomaterials* **2011,** *32* (10), 2586-92.

159.   McDonald, T. O.; Martin, P.; Patterson, J. P.; Smith, D.; Giardiello, M.; Marcello, M.; See, V.; O'Reilly, R. K.; Owen, A.; Rannard, S., Multicomponent organic nanoparticles for fluorescence studies in biological systems. *Adv Funct Mater* **2012,** *22* (12), 2469-2478.

160.   Jiwpanich, S.; Ryu, J.-H.; Bickerton, S.; Thayumanavan, S., Noncovalent encapsulation stabilities in supramolecular nanoassemblies. *J Am Chem Soc* **2010,** *132* (10683-5).

161.   Li, Y.; Budamagunta, M. S.; Luo, J.; Xiao, W.; Voss, J. C.; Lam, K. S., Probing of the assembly structure and dynamics within nanoparticles during interaction with blood proteins. *ACS Nano* **2012,** *6* (11), 9485-95.

162.   Chen, H.; Kim, S.; Li, L.; Wang, S.; Park, K.; Cheng, J.-X., Release of hydrophobic molecules from polymer micelles into cell membranes revealed by Forster resonance energy transfer imaging. *PNAS* **2008,** *105* (18), 6596-601.

163.   Ryu, J.-H.; Chacko, R. T.; Jiwpanich, S.; Bickerton, S.; Babu, R. P.; Thayumanavan, S., Self-cross-linked polymer nanogels: a versatile nanoscopic drug delivery platform. *J Am Chem Soc* **2010,** *132*, 17227-35.

164.   Lu, J.; Owen, S. C.; Shoichet, M. S., Stability of self-assembled polymeric micelles in serum. *Macromolecules* **2011,** *44* (15), 6002-6008.

165.   Njikang, G. N.; Gauthier, M.; Li, J., Sustained release properties of arborescent polystyrene-graft-poly(2-vinylpyridine) copolymers. *Polymer* **2008,** *49* (25), 5474-5481.

166.   Hu, Y.; Kramer, M. C.; Boudreaux, C. J.; McCormick, C. L., Nonradiative energy transfer studies of ph- and salt-responsive associations in hydrophobically modified, hydrolyzed maleic anhydride-ethyl vinyl ether copolymers. *Macromolecules* **1995,** *28*, 7100-6.

167.   Li, Y.; Xiao, W.; Xiao, K.; Berti, L.; Luo, J.; Tseng, H. P.; Fung, G.; Lam, K. S., Well-defined, reversible boronate crosslinked nanocarriers for targeted drug delivery in response to acidic pH values and cis-diols. *Angew Chem Int Ed Engl* **2012,** *51* (12), 2864-9.

168.   Thapaliya, E. R.; Fowley, C.; Callan, B.; Tang, S.; Zhang, Y.; Callan, J. F.; Raymo, F. M., Energy-transfer schemes to probe fluorescent nanocarriers and their emissive cargo. *Langmuir* **2015,** *31* (35), 9557-65.

169.   Cusido, J.; Battal, M.; Deniz, E.; Yildiz, I.; Sortino, S.; Raymo, F. M., Fast fluorescence switching within hydrophilic supramolecular assemblies. *Chemistry* **2012,** *18* (33), 10399-407.

170.   Swaminathan, S.; Petriella, M.; Deniz, E.; Cusido, J.; Baker, J. D.; Bossi, M. L.; Raymo, F. M., Fluorescence photoactivation by intermolecular proton transfer. *J Phys Chem A* **2012,** *116* (40), 9928-33.

171.   Zhang, Y.; Swaminathan, S.; Tang, S.; Garcia-Amoros, J.; Boulina, M.; Captain, B.; Baker, J. D.; Raymo, F. M., Photoactivatable BODIPYs designed to monitor the dynamics of supramolecular nanocarriers. *J Am Chem Soc* **2015,** *137* (14), 4709-19.

172.   Deniz, E.; Tomasulo, M.; Cusido, J.; Yildiz, I.; Petriella, M.; Bossi, M. L.; Sortino, S.; Raymo, F. M., Photoactivatable fluorophores for super-resolution imaging based on oxazine auxochromes. *J Phys Chem C* **2012,** *116* (10), 6058-6068.

173.   Petriella, M.; Deniz, E.; Swaminathan, S.; Roberti, M. J.; Raymo, F. M.; Bossi, M. L., Superresolution imaging with switchable fluorophores based on oxazine auxochromes. *Photochem Photobiol* **2013,** *89* (6), 1391-8.

174.   Swaminathan, S.; Fowley, C.; Thapaliya, E. R.; McCaughan, B.; Tang, S.; Fraix, A.; Captain, B.; Sortino, S.; Callan, J. F.; Raymo, F. M., Supramolecular nanoreactors for intracellular singlet-oxygen sensitization. *Nanoscale* **2015,** *7* (33), 14071-9.

175.	Yildiz, I.; Impellizzeri, S.; Deniz, E.; McCaughan, B.; Callan, J. F.; Raymo, F. M., Supramolecular strategies to construct biocompatible and photoswitchable fluorescent assemblies. *J Am Chem Soc* **2011,** *133* (4), 871-9.

176.	Stepto, R. F. T., Dispersity in polymer science. *Pure Appl Chem* **2009,** *81* (2).

177.	KOPPEL, D. E., Analysis of macromolecular polydispersity in intensity correlation spectroscopy: the method of cumulants. *J Chem Phys* **1972,** *57*, 4815-20.

178.	Mikhalyov, I.; Gretskaya, N.; Bergström, F.; Johansson, L. B. Å., Electronic ground and excited state properties of dipyrrometheneboron difluoride (BODIPY): Dimers with application to biosciences. *Phys. Chem. Chem. Phys.* **2002,** *4* (22), 5663-5670.

179.	Marushchak, D.; Kalinin, S.; Mikhalyov, I.; Gretskaya, N.; LB, A. J., Pyrromethene dyes (BODIPY) can form ground state homo and hetero dimers: photophysics and spectral properties. *Spectrochim Acta A Mol Biomol Spectrosc* **2006,** *65* (1), 113-22.

180.	Molter, J. D.; Chen, Y.; Gratton, E., Fluorescence correlation spectroscopy. *Methods Enzymol.* **2003,** *361*, 69-92.

181.	Thompson, N. L., *Topics in fluorescence spectriscopy*. New York, 1991; Vol. 1.

182.	Piñeiro, L.; Freire, S.; Bordello, J.; Novo, M.; Al-Soufi, W., Dye exchange in micellar solutions. quantitative analysis of bulk and single molecule fluorescence titrations. *Soft Matter* **2013,** *9* (45), 10779.

183.	Tomasulo, M.; Deniz, E.; Alvarado, R. J.; Raymo, F. M., Photoswitchable fluorescent assemblies based on hydrophilic bodipy-spiropyran conjugates. *J Phys Chem C* **2008,** *112*, 8038-8045.

184.	Gabe, Y.; Urano, Y.; Kikuchi, K.; Kojima, H.; Nagano, T., Highly sensitive fluorescence probes for nitric oxide based on boron dipyrromethene chromophoresrational design of potentially useful bioimaging fluorescence probe. *J Am Chem Soc* **2003,** *126*, 3357-3367.

185.	Sandler, S.; Karo, W.; Bonesteel, J.; Pearce, E., *Polymer synthesis and characterization: a laboratory manual*. Academic Press: San Diego, 1998.

186.	Chakraborty, M.; Kuriata, A. M.; Nathan Henderson, J.; Salvucci, M. E.; Wachter, R. M.; Levitus, M., Protein oligomerization monitored by fluorescence fluctuation spectroscopy: self-assembly of rubisco activase. *Biophys J* **2012,** *103* (5), 949-58.

187.	Ciuba, M. A.; Levitus, M., Manganese-induced triplet blinking and photobleaching of single molecule cyanine dyes. *Chemphyschem* **2013,** *14* (15), 3495-502.

188.	Müller, C. B.; Loman, A.; Pacheco, V.; Koberling, F.; Willbold, D.; Richtering, W.; Enderlein, J., Precise measurement of diffusion by multi-color dual-focus fluorescence correlation spectroscopy. *EPL (Europhysics Letters)* **2008,** *83* (4), 46001.

189.   Gendron, P. O.; Avaltroni, F.; Wilkinson, K. J., Diffusion coefficients of several rhodamine derivatives as determined by pulsed field gradient-nuclear magnetic resonance and fluorescence correlation spectroscopy. *J Fluoresc* **2008,** *18* (6), 1093-101.

190.   Srinivasarao, M.; Galliford, C. V.; Low, P. S., Principles in the design of ligand-targeted cancer therapeutics and imaging agents. *Nat Rev Drug Discov* **2015,** *14* (3), 203-19.

191.   Kobayashi, H.; Ogawa, M.; Alford, R.; Choyke, P. L.; Urano, Y., New strategies for fluorescent probe design in medical diagnostic imaging. *Chem Rev* **2010,** *110*, 2620-2640.

192.   Füzéry, A. K.; Levin, J.; Chan, M. M.; Chan, D. W., Translation of proteomic biomarkers into FDA approved cancer diagnostics: issues and challenges. *Clinical Proteomics* **2013,** *10* (13), 1-14.

193.   Low, P. S.; Antony, A. C., Folate receptor-targeted drugs for cancer and inflammatory diseases. *Adv Drug Deliv Rev* **2004,** *56* (8), 1055-8.

194.   Krebs, M. G.; Metcalf, R. L.; Carter, L.; Brady, G.; Blackhall, F. H.; Dive, C., Molecular analysis of circulating tumour cells-biology and biomarkers. *Nat Rev Clin Oncol* **2014,** *11* (3), 129-44.

195.   Nguyen, Q. T.; Tsien, R. Y., Fluorescence-guided surgery with live molecular navigation--a new cutting edge. *Nat Rev Cancer* **2013,** *13* (9), 653-62.

196.   Tung, C.-H.; Lin, Y.; Moon, W. K.; Weissleder, R., A receptor-targeted near-infrared fluorescence probe for in vivo tumor imaging. *ChemBioChem* **2002,** *8*, 784-786.

197.   Fei, X.; Gu, Y.; Wang, Y.; Meng, Q.; Zhang, B., Targeted thiazole orange derivative with folate: synthesis, fluorescence and in vivo fluorescence imaging. *Molecules* **2010,** *15* (10), 6983-92.

198.   Kennedy, M. D.; Jallad, K. N.; Thompson, D. H.; Ben-Amotz, D.; Low, P. S., Optical imaging of metastatic tumors using a folate-targeted fluorescent probe. *J Biomed Opt* **2003,** *8* (4), 636-41.

199.   van Dam, G. M.; Themelis, G.; Crane, L. M.; Harlaar, N. J.; Pleijhuis, R. G.; Kelder, W.; Sarantopoulos, A.; de Jong, J. S.; Arts, H. J.; van der Zee, A. G.; Bart, J.; Low, P. S.; Ntziachristos, V., Intraoperative tumor-specific fluorescence imaging in ovarian cancer by folate receptor-alpha targeting: first in-human results. *Nat Med* **2011,** *17* (10), 1315-9.

200.   Liu, F.; Deng, D.; Chen, X.; Qian, Z.; Achilefu, S.; Gu, Y., Folate-polyethylene glycol conjugated near-infrared fluorescence probe with high targeting affinity and sensitivity for in vivo early tumor diagnosis. *Mol Imaging Biol* **2010,** *12* (6), 595-607.

201.   Kelderhouse, L. E.; Chelvam, V.; Wayua, C.; Mahalingam, S.; Poh, S.; Kularatne, S. A.; Low, P. S., Development of tumor-targeted near infrared probes for fluorescence guided surgery. *Bioconjug Chem* **2013,** *24* (6), 1075-80.

202.   Moon, W. K.; Lin, Y.; O'Loughlin, T.; Tang, Y.; Kim, D.-E.; Weissleder, R.; Tung, C.-H., Enhanced tumor detection using a folate receptor-targeted near-infrared fluorochrome conjugate. **2003,** *14* (539-545).

203.   He, W.; Wang, H.; Hartmann, L. C.; Cheng, J.-X.; Low, P. S., In vivo quantitation of rare circulating tumor cells by multiphoton intravital flow cytometry. *PNAS* **2007,** *104* (28), 11760-11765.

204.   Bonacchi, S.; Genovese, D.; Juris, R.; Montalti, M.; Prodi, L.; Rampazzo, E.; Zaccheroni, N., Luminescent silica nanoparticles: extending the frontiers of brightness. *Angew Chem Int Ed Engl* **2011,** *50* (18), 4056-66.

205.   Yan, J.; Estévez, M. C.; Smith, J. E.; Wang, K.; He, X.; Wang, L.; Tan, W., Dye-doped nanoparticles for bioanalysis. *Nano Today* **2007,** *2* (3), 44-50.

206.   Lee, R. J.; Wang, S.; Low, P. S., Measurement of endosome pH following folate receptor-mediated endocytosis *Biochim Biophys Acta* **1996,** *1312*, 237-242.

207.   Das, M.; Datir, S. R.; Singh, R. P.; Jain, S., Augmented anticancer activity of a targeted, intracellularly activatable, theranostic nanomedicine based on fluorescent and radiolabeled, methotrexate-folic Acid-multiwalled carbon nanotube conjugate. *Mol Pharm* **2013,** *10* (7), 2543-57.

208.   Xiong, J.; Meng, F.; Wang, C.; Cheng, R.; Liu, Z.; Zhong, Z., Folate-conjugated crosslinked biodegradable micelles for receptor-mediated delivery of paclitaxel. *J Mater Chem* **2011,** *21* (15), 5786.

209.   Shanmugam, V.; Chien, Y. H.; Cheng, Y. S.; Liu, T. Y.; Huang, C. C.; Su, C. H.; Chen, Y. S.; Kumar, U.; Hsu, H. F.; Yeh, C. S., Oligonucleotides--assembled Au nanorod-assisted cancer photothermal ablation and combination chemotherapy with targeted dual-drug delivery of Doxorubicin and Cisplatin prodrug. *ACS Appl Mater Interfaces* **2014,** *6* (6), 4382-93.

210.   Tian, J.; Ding, L.; Xu, H. J.; Shen, Z.; Ju, H.; Jia, L.; Bao, L.; Yu, J. S., Cell-specific and pH-activatable rubyrin-loaded nanoparticles for highly selective near-infrared photodynamic therapy against cancer. *J Am Chem Soc* **2013,** *135* (50), 18850-8.

211.   Santra, S.; Jativa, S. D.; Kaittanis, C.; Normand, G.; Grimm, J.; Perez, J. M., Gadolinium-encapsulating iron oxide nanoprobe as activatable NMR/MRI contrast agent. *ACS Nano* **2012,** *6* (8), 7281-7294.

212. Urano, Y.; Asanuma, D.; Hama, Y.; Koyama, Y.; Barrett, T.; Kamiya, M.; Nagano, T.; Watanabe, T.; Hasegawa, A.; Choyke, P. L.; Kobayashi, H., Selective molecular imaging of viable cancer cells with pH-activatable fluorescence probes. *Nat Med* **2009,** *15* (1), 104-9.

213. Daly, B.; Ling, J.; de Silva, A. P., Current developments in fluorescent PET (photoinduced electron transfer) sensors and switches. *Chem Soc Rev* **2015,** *44* (13), 4203-11.

214. Raymo, F. M., Photoactivatable synthetic fluorophores. *Phys Chem Chem Phys* **2013,** *15* (36), 14840-50.

215. MULLER, P., Glossary of terms used in physical organic chemistry. *Pure Appl Chem* **1994,** *66*, 1077-1184.

216. Speight, J. G., *Lange's handbook of chemistry*. 2005.

217. Sheng, L.; Li, M.; Zhu, S.; Li, H.; Xi, G.; Li, Y. G.; Wang, Y.; Li, Q.; Liang, S.; Zhong, K.; Zhang, S. X. A., Hydrochromic molecular switches for water-jet rewritable paper. *Nat. Commun.* **2014,** *5*, 3044.

218. Horiguchi, T.; Koshiba, Y.; Ueda, Y.; Origuchi, C.; Tsutsui, K., Reversible coloring/decoloring reaction of leuco dye controlled by long-chain molecule. *Thin Solid Films* **2008,** *516*, 2591.

219. Garcia-Amorós, J.; Swaminathan, S.; Raymo, F. M., Saving paper with switchable ink. *Dyes Pigm.* **2014,** *106*, 71.

220. Han, J.; Burgess, K., Fluorescent indicators for intracellular pH. *Chem. Rev.* **2010,** *110*, 2709.

221. Feringa, B. L.; Brown, W. L., *Molecular switches*. Wiley-VCH: Weinheim, 2011.

222. Deniz, E.; Tomasulo, M.; Cusido, J.; Yildiz, I.; Petriella, M.; Bossi, M. L.; Sortino, S.; Raymo, F. M., Photoactivatable fluorophores for super-resolution imaging based on oxazine auxochromes. *J. Phys. Chem. C* **2012,** *116*, 6058.

223. Garcia-Amorós, J.; Swaminathan, S.; Sortino, S.; Raymo, F. M., Plasmonic activation of a fluorescent carbazole–oxazine switch. *Chem. - Eur. J.* **2014,** *20*, 10276.

224. Swaminathan, S.; Petriella, M.; Deniz, E.; Cusido, J.; Baker, J. D.; Bossi, M. L.; Raymo, F. M., Fluorescence photoactivation by intermolecular proton transfer. *J. Phys. Chem. A* **2012,** *116*, 9928.

225. Petriella, M.; Deniz, E.; Swaminathan, S.; Roberti, M. J.; Raymo, F. M.; Bossi, M. L., Superresolution imaging with switchable fluorophores based on oxazine auxochromes. *Photochem. Photobiol.* **2013,** *89*, 1391.

226.   Deniz, E.; Kandoth, N.; Fraix, A.; Cardile, V.; Graziano, A. C. E.; Lo Furno, D.; Gref, R.; Raymo, F. M.; Sortino, S., Photoinduced fluorescence activation and nitric oxide release with biocompatible polymer nanoparticles. *Chem. - Eur. J.* **2012,** *18*, 15782.

227.   Ogawa, M.; Kosaka, N.; Regino, C. A. S.; Mitsunaga, M.; Choyke, P. L.; Kobayashi, H., High sensitivity detection of cancer in vivo using a dual-controlled activation fluorescent imaging probe based on H-dimer formation and pH activation. *Mol. BioSyst.* **2010,** *6*, 888.

228.   Tian, J.; Ding, L.; Ju, H.; Yang, Y.; Li, X.; Shen, Z.; Zhu, Z.; Yu, J. S.; Yang, C. J., A multifunctional nanomicelle for real-time targeted imaging and precise near-infrared cancer therapy. *Angew. Chem., Int. Ed.* **2014,** *53*, 9544.

229.   Urano, Y.; Asanuma, D.; Hama, Y.; Koyama, Y.; Barrett, T.; Kamiya, M.; Nagano, T.; Watanabe, T.; Hasegawa, A.; Choyke, P. L.; Kobayashi, H., Selective molecular imaging of viable cancer cells with pH-activatable fluorescence probes. *Nat. Med.* **2009,** *15*, 104.

230.   Deniz, E.; Sortino, S.; Raymo, F. M., Fluorescence switching with a photochromic auxochrome. *J. Phys. Chem. Lett.* **2010,** *1*, 3506.

231.   Cusido, J.; Battal, M.; Deniz, E.; Yildiz, I.; Sortino, S.; Raymo, F. M., Fast fluorescence switching within hydrophilic supramolecular assemblies. *Chem. - Eur. J.* **2012,** *18*, 10399.

232.   Liu, Q.; Xu, S.; Niu, C.; Li, M.; He, D.; Lu, Z.; Ma, L.; Na, N.; Huang, F.; Jiang, H.; Ouyang, J., Distinguish cancer cells based on targeting turn-on fluorescence imaging by folate functionalized green emitting carbon dots. *Biosens. Bioelectron.* **2015,** *64*, 119.

233.   Li, K.; Jiang, Y.; Ding, D.; Zhang, X.; Liu, Y.; Hua, J.; Feng, S.; Liu, B., Folic acid-functionalized two-photon absorbing nanoparticles for targeted MCF-7 cancer cell imaging. *Chem. Commun.* **2011,** *47*, 7323.

234.   Zhang, Y.; Thapaliya, E. R.; Tang, S.; Baker, J. D.; Raymo, F. M., Supramolecular delivery of fluorescent probes in developing embryos. *RSC Adv.* **2016,** *6*, 72756.

235.   Wu, J.-S.; Liu, W.-M.; Zhuang, X.-Q.; Wang, F.; Wang, P.-F.; Tao, S.-L.; Zhang, X.-H.; Wu, S.-K.; Lee, S.-T., Fluorescence turn on of coumarin derivatives by metal cations: a new signaling mechanism based on C=N isomerization. *Org Lett* **2007,** *9* (1), 33-36.

236.   Deniz, E.; Sortino, S.; Raymo, F. i. M., Fluorescence switching with a photochromic auxochrome. *J Phys Chem Lett* **2010,** *1* (24), 3506-3509.

237.   Yildiz, I.; Deniz, E.; McCaughan, B.; Cruickshank, S. F.; Callan, J. F.; Raymo, F. M., Hydrophilic CdSe-ZnS core-shell quantum dots with reactive functional groups on their surface. *Langmuir* **2010,** *26* (13), 11503-11.

238.   Wurth, C.; Grabolle, M.; Pauli, J.; Spieles, M.; Resch-Genger, U., Relative and absolute determination of fluorescence quantum yields of transparent samples. *Nat Protoc* **2013,** *8* (8), 1535-50.

239.   Corey, E. J.; Cheng, X.-M., *The logic of chemical synthesis*. Wiley: New York, 1995.

240.   Wolpert, L.; Tickle, C.; Arias, A. M., *Principles of development*. Oxford University Press: Oxford, 2015.

241.   Dugatkin, L. A., *Principles of animal behavior*. Norton & Company, 2014.

242.   Gorris, H. H.; Wolfbeis, O. S., Photon-upconverting nanoparticles for optical encoding and multiplexing of cells, biomolecules, and microspheres. *Angew Chem Int Ed Engl* **2013,** *52* (13), 3584-600.

243.   Leng, Y.; Sun, K.; Chen, X.; Li, W., Suspension arrays based on nanoparticle-encoded microspheres for high-throughput multiplexed detection. *Chem Soc Rev* **2015,** *44* (15), 5552-95.

244.   Shikha, S.; Salafi, T.; Cheng, J.; Zhang, Y., Versatile design and synthesis of nano-barcodes. *Chem Soc Rev* **2017,** *46* (22), 7054-7093.

245.   Jun, B. H.; Kang, H.; Lee, Y. S.; Jeong, D. H., Fluorescence-based multiplex protein detection using optically encoded microbeads. *Molecules* **2012,** *17* (3), 2474-90.

246.   Puliti, D.; Warther, D.; Orange, C.; Specht, A.; Goeldner, M., Small photoactivatable molecules for controlled fluorescence activation in living cells. *Bioorg Med Chem* **2011,** *19* (3), 1023-9.

247.   Klan, P.; Solomek, T.; Bochet, C. G.; Blanc, A.; Givens, R.; Rubina, M.; Popik, V.; Kostikov, A.; Wirz, J., Photoremovable protecting groups in chemistry and biology: reaction mechanisms and efficacy. *Chem Rev* **2013,** *113* (1), 119-91.

248.   Wysocki, L. M.; Lavis, L. D., Advances in the chemistry of small molecule fluorescent probes. *Curr Opin Chem Biol* **2011,** *15* (6), 752-9.

249.   Raymo, F. M., Photoactivatable synthetic dyes for fluorescence imaging at the nanoscale. *J Phys Chem Lett* **2012,** *3* (17), 2379-85.

250.   Li, W. H.; Zheng, G., Photoactivatable fluorophores and techniques for biological imaging applications. *Photochem Photobiol Sci* **2012,** *11* (3), 460-71.

251.   Deniz, E.; Tomasulo, M.; Cusido, J.; Sortino, S.; Raymo, F. M., Fast and stable photochromic oxazines for fluorescence switching. *Langmuir* **2011,** *27* (19), 11773-83.

252.   Kamkaew, A.; Lim, S. H.; Lee, H. B.; Kiew, L. V.; Chung, L. Y.; Burgess, K., BODIPY dyes in photodynamic therapy. *Chem Soc Rev* **2013,** *42* (1), 77-88.

253.   Lu, H.; Mack, J.; Yang, Y.; Shen, Z., Structural modification strategies for the rational design of red/NIR region BODIPYs. *Chem Soc Rev* **2014,** *43* (13), 4778-823.

254.   Benstead, M.; Mehl, G. H.; Boyle, R. W., 4,4'-Difluoro-4-bora-3a,4a-diaza-s-indacenes (BODIPYs) as components of novel light active materials. *Tetrahedron* **2011,** *67* (20), 3573-3601.

255.   Zhang, Y.; Tang, S.; Sansalone, L.; Baker, J. D.; Raymo, F. M., A photoswitchable fluorophore for the real-time monitoring of dynamic events in living organisms. *Chemistry* **2016,** *22* (42), 15027-15034.

256.   Garcia-Amoros, J.; Swaminathan, S.; Zhang, Y.; Nonell, S.; Raymo, F. M., Optical writing and reading with a photoactivatable carbazole. *Phys Chem Chem Phys* **2015,** *17* (17), 11140-3.

257.   Goswami, P. P.; Syed, A.; Beck, C. L.; Albright, T. R.; Mahoney, K. M.; Unash, R.; Smith, E. A.; Winter, A. H., BODIPY-derived photoremovable protecting groups unmasked with green light. *J Am Chem Soc* **2015,** *137* (11), 3783-6.

258.   Kobayashi, T.; Komatsu, T.; Kamiya, M.; Campos, C.; Gonzalez-Gaitan, M.; Terai, T.; Hanaoka, K.; Nagano, T.; Urano, Y., Highly activatable and environment-insensitive optical highlighters for selective spatiotemporal imaging of target proteins. *J Am Chem Soc* **2012,** *134* (27), 11153-60.

259.   Amamoto, T.; Hirata, T.; Takahashi, H.; Kamiya, M.; Urano, Y.; Santa, T.; Kato, M., Spatiotemporal activation of molecules within cells using silica nanoparticles responsive to blue-green light. *Journal of Materials Chemistry B* **2015,** *3* (37), 7427-7433.

260.   Ragab, S. S.; Swaminathan, S.; Baker, J. D.; Raymo, F. M., Activation of BODIPY fluorescence by the photoinduced dealkylation of a pyridinium quencher. *Phys Chem Chem Phys* **2013,** *15* (36), 14851-5.

261.   Frolund, B.; Ebert, B.; Kristiansen, U.; Liljefors, T.; Krogsgaard-Larsen, P., GABA-A receptor ligands and their therapeutic potentials. *Curr Top Med Chem* **2002,** *2* (8), 817-832.

262.   Fang-Yena, C.; Averyb, L.; Samuela, A. D. T., Two size-selective mechanisms specifically trap bacteria-sized food particles in Caenorhabditis elegans. *PNAS* **2009,** *106* (47), 20093-20096.

263.   Collins, K. M.; Koelle, M. R., Postsynaptic ERG potassium channels limit muscle excitability to allow distinct egg-laying behavior states in Caenorhabditis elegans. *J Neurosci* **2013,** *33* (2), 761-75.

264.   Madhu, S.; Rao, M. R.; Shaikh, M. S.; Ravikanth, M., 3,5-Diformylboron dipyrromethenes as fluorescent pH sensors. *Inorg Chem* **2011,** *50* (10), 4392-400.

265.   Scaiano, J. C., *CRC handbook of organic photochemistry*. CRC Press: Boca Raton, 1989.

266.   Edwards, S. L.; Charlie, N. K.; Milfort, M. C.; Brown, B. S.; Gravlin, C. N.; Knecht, J. E.; Miller, K. G., A novel molecular solution for ultraviolet light detection in Caenorhabditis elegans. *PLoS Biol* **2008,** *6* (8), 198.